3D MESO-SCALE MODELLING OF SOLIDIFICATION: APPLICATION TO ADVANCED HIGH STRENGTH STEELS

3D MESO-SCALE MODELLING OF SOLIDIFICATION: APPLICATION TO ADVANCED HIGH STRENGTH STEELS

BY
YI FENG, M.Sc.

A THESIS
SUBMITTED TO THE DEPARTMENT OF MATERIALS SCIENCE AND ENGINEERING
AND THE SCHOOL OF GRADUATE STUDIES
OF MCMASTER UNIVERSITY
IN PARTIAL FULFILMENT OF THE REQUIREMENTS
FOR THE DEGREE OF
DOCTOR OF PHILOSOPHY

Doctor of Philosophy (2020) McMaster University
(Materials Science and Engineering) Hamilton, Ontario, Canada

TITLE:	3D Meso-scale Modelling of Solidification: Application to Advanced High Strength Steels
AUTHOR:	Yi Feng B.Eng. (Metallurgy Engineering), Northeastern University, Shenyang, China M.Sc. (Ferrous Metallurgy), Northeastern University, Shenyang, China
SUPERVISOR:	Prof. André B. Phillion
NUMBER OF PAGES:	xxi, 136

Preface

The current mesoscale model is built on previous granular models developed at École Polytechnique Fédérale de Lausanne and The University of British Columbia by PhD students M. Sistaninia and H.R. Zareie Rajani, and supervised by Professors M. Rappaz, and A.B. Phillion. With the exception of Dr. M. Založnik and Dr. B.G. Thomas, who provided valuable suggestions for this research, I am the key contributor to this work. I successfully extended the previous models and applied them to the continuous casting process of steel. I managed to bridge some of the existing gaps inherent to the previous models, and overcome significant limitations to apply this technique to alloys having dendritic microstructure. Specifically, I developed three brand new numerical modules (Dendritic solidification, Dendritic fluid flow, and Alloy segregation) using C++, and incorporated them into this mesoscale model. I also managed to predict centreline segregation with high computational efficiency, and validated the predicted solute distribution against microscale X-Ray fluorescence spectroscopy measurement made with the help from Dr. J. Sengupta at ArcelorMittal's Global R&D Centre in Hamilton, Canada.

Part of the results of this research have been presented in two international conferences: 1) Feng, Y., Phillion, A.B. A 3D Meso-Scale Solidification Model for Steels, AISTech Conference Proceedings 2018 May. 2) Feng, Y., Založnik M., Thomas, B.G., Phillion, A.B. A 3D discrete-element model for simulating liquid feeding during dendritic solidification of steel. In IOP Conference Series: Materials Science and Engineering 2019 May (Vol. 529, No. 1, p. 012031). The research results have also been published in refereed journals: 1) Feng, Y., and Phillion, A.B. "A 3D mesoscale solidification model for metallic alloy using a volume average approach." Materialia 6 (2019): 100329; 2) Feng, Y., Založnik, M., Thomas, B.G. and Phillion, A.B." Mesoscale simulation of liquid feeding in an equiaxed dendritic mushy zone." Materialia 9 (2020): 100612; 3) Feng, Y., Založnik, M., Thomas, B.G. and Phillion, A.B. "Mesoscale simulation of central segregation in an equiaxed dendritic mushy zone during continuous casting of steel." ready to submit to Acta Materialia in Dec. , 2020; and 4) Feng, Y., Phillion, A.B. "A 3-D coupled hydromechanical model for predicting hot tearing within semisolid consisting of dendritic equiaxed grains." (Manuscript currently in preparation).

Abstract

Advanced high strength steels (AHSSs) are considered to have a promising future due to the outstanding properties compared with the conventional steel and have been widely adopted as the base materials for the automotive components. Some of the challenges preventing the extensive applications of AHSSs are due the solidification defects, i.e. hot tearing and segregation. In this thesis, a 3D mesoscale and multi-physics model is developed and validated to directly investigate solidification defects for semi-solid steel with dendritic morphology associated with the peritectic transformation. Similar to the prior models [1, 2], the current model explicitly considers the solidification behavior of each grain prior to assembling, which allows for the mesoscale simulation within a semisolid containing thousands of grains. Six sub-models are incorporated: (i) microstructure generation model is used to create the fully solidified microstructure of equiaxed grains based on a Voronoi tessellation; (ii) a dendritic solidification module based on an average volume approach is developed for predicting the solidification behavior of a random set of grains, considering the diffusion in different phases along with peritectic transformation. The progressive coalescence to form a solid cluster is predicted by incorporating an interfacial energy determination model; (iii) a fluid flow module is developed for the prediction of both intra-dendritic flow and extra-dendritic flow within the dendritic network induced by solidification shrinkage and deformation; (iv) a semisolid deformation model is used and extended to simulate the semi-solid mechanical behavior of steel using a discrete element method. The solid grains are modeled using a constitutive law and implemented via Abaqus commercial software; (v) a coupled cracking model incorporated with a failure criterion is used and extended to predict the crack formation and propagation in semi-solid steel. This comprehensive model consists of models (i-iv) and considers the interaction between the deformation within the solid phase and pressure drop in the liquid phase; (vi) a one-way coupled solute transportation module is also developed and used to simulate the solute redistribution due to fluid flow and diffusion within the liquid channels assuming the solid grains are fixed. The movement of the solute-enriched liquid in the solute transport model is induced by solidification shrinkage and deformation.

The new 3D mesoscale model is then applied to correlate the semisolid behavior during solidification to different physical and process parameters. The results from the dendritic solidification model show the evolution in semi-solid microstructure and consequently liquid film migration. The model is able to predict the solidification of equiaxed grains with either globular and dendritic structure having experiencing primary solidification and the peritectic transformation. The coalescence phenomenon between grains is considered at the end of solidification using Bulatov's approach [24] for estimating interfacial energy. It is seen that only 0.9% of the grains are attractive based on their orientations within a specific domain, significantly depressing final-stage solidification. The dendritic fluid flow model quantitatively captures both semi-solid morphology and the fluid flow behavior, and provides an alternative to the convectional experiment for the prediction of permeability by using the given surface area concentration. Comparison of the numerical and experimental permeabilities shows a good agreement (within $\pm$ 5%) for either extra-dendrite or intra-dendritic flow, and deviation from the conventional Carman-Kozeny equations using simplified Dendritic S_v or Globular S_v are explained in detail. The results quantitatively demonstrate the effect of grain size and microstructure morphology during solidification on the permeability prediction. The localization of liquid feeding under the pressure gradient is also reproduced. Additionally, the fluid flow due to shrinkage and deformation for non-peritectic and peritectic steel grades with dendritic morphology during solidification was captured for the first time. The cracking model allows for the prediction of hot tearing initiation and the progressive propagation during a tensile test deformation and the results are compared with the experimental results conducted by Seol et al. [3] at different solid fractions. Parametric studies of coalescence criteria and surface tension on the constitutive behavior of the semisolid are discussed and the deformation behavior of alloys with different carbon contents under a feedable mushy zone is investigated. Finally, the solute transport model has been applied to the continuous casting process of steel for the investigation of centreline segregation, and results indicate that the grain size has a great impact on the solute distribution and solute partitioning combined with intra-dendritic fluid flow leads eventually to liquid channels enriched with solute. The predicted composition in these discrete liquid channels shows a great match with the experimental measured profile obtained via the microscopic X-Ray fluorescence (MXRF).

Keywords : Hot cracking, Permeability, Solidification, Segregation, Peritectic transformation, Finite element analysis

The thesis is dedicated to my beloved parents for all their love and support

Acknowledgements

I would like to express my sincere gratitude to my supervisor Dr. André Phillion for his guidance, encouragement and great support. His wide knowledge in solidification and process metallurgy and sharp vision of future trends formed the basis of this thesis.

I would like to thank Dr. Brian Thomas and Dr. Miha Založnik for their insightful and constructive comments on this thesis. I would also like to thank Dr. Hatem Zurob, Dr. Michael Greenwood, Dr. Ken Coley and Dr. Neslihan Dogan for being my annual committee meeting members and providing me with great suggestions during my PhD journey. I would also like to thank my industrial sponsor Dr. Joydeep Sengupta for many useful interactions and discussions.

My gratitude also goes to my best friends Baoqin Deng, Weiwei Zhang, Dr. Hanshuo Liu, Taoran Wang, Dr. Yutong Ge, Yujiao Hao, Yuanzhe Chen, Dr. Kezhuan Gu for their company; Special thanks to my group mates Mohammad H. Ghoncheh, Zhen Li, Niloufar Khodaei, Pardis Mohammadpour, Coleton Parks, Farheen Ahmed, Angshuman Podder, Prabhakar Pal, Kaamil Ur Rahman Mohamed Shibly, Dr. Khaled Abu Samk, Dr. Stefan Heugenhauser for generously sharing their thoughts and knowledge. Their help and friendship have made my PhD journey an unforgettable experience.

Last but by no means least, I would like to thank my parents for their unconditional love and support.

Contents

Preface **iii**

Abstract **iv**

Acknowledgements **vii**

Notation, Definitions, and Abbreviations **xvi**

1 Introduction **1**
1.1 Overview 1
1.2 Solidification during the AHSSs continuous casting process . . 4
1.3 Solidification defects of AHSSs during casting 6
1.4 Outline 9

2 Literature Review **10**
2.1 Solidification 10
2.2 Segregation 13
2.3 Hot tearing 21

3 Scope and Objectives **36**

4 Methods **38**
4.1 Fundamental models 39
4.2 Defect prediction 56
4.3 Validation of mesoscale models 65

5 Results and Discussions **69**
5.1 Dendritic solidification model 69
5.2 Dendritic fluid flow model 78
5.3 Semisolid cracking model 92
5.4 Mesoscale solute transportation model 101

6 Conclusions **117**

List of Figures

1.1 Targets for passenger vehicle fuel efficiency in nine countries [4]. 3
1.2 Elongation-tensile strength diagram for various steels [5]. . . . 4
1.3 Schematic diagram of the continuous casting apparatus along with a flow pattern inside the mold [6]. 5
1.4 Typical hot tears observed within steel slabs [7]. 7
1.5 Schematic diagram of mechanisms of hot tearing in steels [8]. . 7
2.1 (a) A Fe-C binary phase diagram and (b) mechanism of peritectic reaction and transformation during solidification [9]. . . 11
2.2 Solute mapping obtained from EPMA within a steel sample cut from continuously casting slab with different P contents: (a) 0.01 wt.%P, (b) 0.10 wt.%P and (c)0.20 wt.%P. [10]. 14
2.3 Solute mapping measured from XRF within a cross-section of a ingot sample for Cr and Mo [11]. 15
2.4 Columnar dendrites growing during solidification process of succinonitrile-acetone alloy (left) and a simplified schematic diagram of dendrite secondary arms used for microsegregation analysis [12]. . 15
2.5 (a) Schematics illustrating the partitioning of solute from interface to liquid phase in (a) Lever Rule model and (b) Gulliver-Scheil model of microsegregation. 16
2.6 (a) A schematic of an equiaxed dendrite enclosed by an envelope and a solute profile in different phases [12]. 19
2.7 Schematic diagram of Crickacier hot tearing test [8]. 21
2.8 Schematic diagram of a Gleeble thermo-mechanical simulator [13]. 22
2.9 Schematic diagram of a submerged spill chill tensile test apparatus [14]. 24
2.10 Schematic diagram of a compression test apparatus [15]. . . . 25
2.11 Fractographs of steel samples produced with final electromagnetic stirring: (a) cracked region, (b) dendritic region and (c) breaking point of the dendrite [16]. 25
2.12 Fractograph of a steel sample with a partially melt region [17]. 26
2.13 A healed hot tear [18]. 27

2.14 (a) Specimen geometry designed for the experiment; (b) a schematic diagram of the furnace and tensile grips; and (c) experimental setup on beamline I12 at Diamond Light Source [19]. 28
2.15 A schematic of liquid feeding to compensate shrinkage and uniaxial deformation within a small volume element [20]. 29
2.16 Comparison between tensile experimental results of an Al-1wt.% Cu alloy and simulation results at different experimental temperatures. The nominal stress shown on the right is calculated at the neck zone [21]. 32
2.17 Defect evolution of the semi-solid Al-2wt.%Cu specimen under tensile deformation rate at 10^{-4} s^{-1} at (a) 405 s, (b) 729 s and (c) 1215 s [22]. 33
2.18 Comparison between simulation results (dashed lines) with experimental measurement (solid lines) on a semi-solid Al-2wt.% Cu at a solid fraction of $g_s = 0.98$ at two strain rates [22]. . . 34
2.19 Modelling of crack during fusion welding based on Kou's cracking criterion at three different solid fractions of 0.7, 0.8 and 0.96, respectively [23]. 34
4.1 Various geometries of the 3D meso-scale model: (a) 3D Voronoi tessellation consisting of 27 grains each colored by a different grayscale value; (b) a single Voronoi grain; (c) polyhedral element, (d) tetrahedral element, (e) semi-solid domain with 1000 grains at the solid fraction 0.81. In (e) the liquid is colored black, while the delta ferrite grains are colored in gray. Note that the amount of remaining liquid within each grain is represented by the channel thickness. 41
4.2 Schematic diagram showing (a) primary solidification and (b) primary solidification plus peritectic transformation. The images (1), (2), and (3) show the actual dendritic structure, equivalent structure for the volume average model, and the geometric structure for the meso-scale model. The grey, red, and white regions indicate the δ, γ and l regions. The dotted red line denotes the dendrite envelope. 42
4.3 Evolution of liquid, solid-δ and dendrite envelope fraction of a single grain for a Fe-0.07 wt.% C alloy cooling at (a) 0.1°C/s and (b) 50°C/s. A grain radius of 100 µm and a secondary arm spacing of 20 µm are assumed in both cases. 45
4.4 (a) Meso-scale simulation domain containing 125 equiaxed grains with different orientations; (b) grain boundary energy and coalescence undercooling distributions used in the multi-physics model for a Fe-0.16wt.% C alloy as proposed by Bulatov et al. [24]. 46

4.5 Schematic of the smoothing process of grain corner in a 3-D element following Sistaninia [1]. Note that the amount of remaining liquid between grains is highlighted in yellow. 47
4.6 Schematic diagram of two facing tetrahedrons, the velocity profile of fluid passing through the inter- and extra- dendritic regions, and the corresponding 3-node 2D triangular element. The velocity profiles for the cases with only intra-dendritic and only extra-dendritic flow are also shown. 49
4.7 Schematic of equiaxed grains and three different types of finite element used in the simulation: (a) Voronoi grain, (b) 3D solid element consists of multiple tetrahedral elements, (c) multi-point constrained element between two nodes belong to one grain and (d) contact element located between two solid elements across the grain boundary. 54
4.8 Comparison of stress and strain curve for δ and γ phase under different strain rates at 1480 °C: 10^{-3} s^{-1}, 5×10^{-3} s^{-1} and 10^{-2} s^{-1}, respectively. 55
4.9 Schematic of coupling between sub-models for the prediction of cracks. 57
4.10 Schematic of two facing grains with a liquid film in between where a meniscus with a hemi-cylindrical shape forms. 59
4.11 Influence of sulfur and oxygen contents on surface tension of liquid iron. 60
4.12 Flow chart of the hydro-mechanical coupling procedures following Sistaninia et al. [1]. 61
4.13 Schematic diagram of sampling within the continuous casting slab. 66
4.14 (a) Photograph of experimental setup of Micro X-Ray Fluorescence device at Arcelor Mittal Dofasco, and (b) MXRF scanning stage [25, 26]. 67
5.1 Simulation domain (5mm×5mm×5mm) containing 125 grains for a Fe-0.16wt.%C alloy: (a) coalescence of grain clusters at different time; (b) evolution of the number of grain clusters as a function of time. 71
5.2 2D Cross-sections from the 3D meso-scale solidification model of steel consisting of 1000 grains and a total domain size of 125 mm^3. (a-d) represent simulations with different carbon compositions, each for three different temperatures. (I-III) presents three different temperatures of 1507.1°C, 1492.2°C and 1491.8°C, respectively. Note that $g_{l\_extra}\sim0$. 73

5.3 The distribution in liquid channel widths for cases (b3), (c3), and (d3) from Fig. 5.2 corresponding to compositions of 0.12wt.%, 0.16wt.%, and 0.18wt.% 74
5.4 The evolution of semi-solid microstructure and the liquid channel thickness within the domain size of 125 mm^3 consisting of 1000 grains for a Fe-0.07 wt.%C alloy at T=1507°C under different cooling rates: (a) 25 °C/s; (b) 50 °C/s and (c) 75 °C/s. Note that $g_{l\_extra} \sim 0$. 75
5.5 The evolution of liquid channel width at different temperatures within the domain size of 125 mm^3 for a Fe-0.16 wt.%C alloy consisting grains with average grain size of: (a) 500 µm; (b) 1000 µm. Note that $g_{l\_extra} \sim 0$. 76
5.6 Internal solid fraction evolution within a single grain with a final diameter of 300 µm under three cooling rates along with the schematic diagrams of intra-dendritic, extra-dendritic and both fluid flow types. 78
5.7 Pressure distribution within a domain containing 8000 grains at g_s=0.60 solidified under three cooling rates: (a) CR=1K/s, (b) CR=5K/s and (c) CR=55K/s. Note that Fig. 5.7(a) and (b) share the same color bar. 80
5.8 Validation of permeability predicted by present model with the Carman-Kozeny equation for a uniform network of grains with microstructure solidified under the cooling rate of 1K/s, 5K/s and 55K/s. 82
5.9 (a) Equivalent grain size d distribution within the semisolid domain and (b) the variation in g_s' for five grains containing different sizes. 83
5.10 Variations of permeability as a function of solid fraction for a semisolid domain containing both intra-dendritic and extra-dendritic flow. 84
5.11 Permeability map as a function of solid fractions and (a) cooling rate as well as (b) dimensionless grain size, $d/(2 \cdot \lambda_2)$. 85
5.12 Influence of S_v calculated based on different internal solid fractions on the prediction of the permeability within mushy zone via Carman-Kozeny equation. 87
5.13 Variations in permeability (-1) and local velocity (-2) within a semisolid domain at (a)g_s=0.70 and (b) g_s=0.84. The grain size was 500 µm, and the cooling rate was 5 K/s 88

5.14 A comparison of Q/V predicted by the 3D dendritic fluid flow model and Eq. 5.2.3 as a function of solid fraction for various Fe-C alloys along with the pressure contours at three solid fractions for Fe-0.12wt.% alloy. The required flux to compensate for the peritectic transformation in peritectic grades is also included in the flow predictions of the 3D dendritic fluid flow model.Note that Fig. 5.14(b1) and (b2) share the same color bar. 89
5.15 A comparison of the Q/V predicted by the 3D dendritic fluid flow model taking into account both solidification shrinkage and deformation. Strain rates of 0.1 s^{-1} (upper) and 0.001 s^{-1} (lower) are examined. 91
5.16 Schematic diagram of boundary conditions imposed in the semi-solid domain for stress calculation. 93
5.17 Predicted semisolid behavior with a solid fraction of 0.90 under a constant tensile deformation for non-peritectic and hyper-peritectic alloys: (a) liquid pressure and (b) average stress as a function of strain. 94
5.18 Simulated (a) liquid pressure and (b) stress as a function of strain for a semisolid at g_s=0.90 under the tensile strain rate of 0.01 s^{-1}. 96
5.19 Comparison between the tensile strength measured in the steel samples by Seol et al. [27] and the results of the semisolid cracking model. 98
5.20 Comparison between average stress as a function of strain for various coalescence criteria. 99
5.21 Contours plots of the Von Mises stress at a given strain of 0.003 predicted by using different coalescence criteria with attractive proportion of (a) 15.4% and (b) 0.8%, respectively. 99
5.22 Influence of surface tension on stress strain curve of a semisolid at g_s=0.90 due to the presence of sulfur and oxygen. 100
5.23 (a) Temperature evolution along the centreline predicted by CON1D along with a schematic diagram of simulation domain location; (b) corresponding lines of $g_s = 0$ and $g_s = 1$ to denote the extent of the mushy zone; (c) solid fraction variations at positions P_i and P_{ii} within the mesoscale simulation domain, along with a schematic of the applied subdivision used to reduce computation time. Note that the solid fraction is a sum of both delta phase and austenite phase. 103
5.24 Boundary conditions applied for the simulation domain with a size of 2700 mm × 20 mm × 20 mm identified by the liquidus and solidus lines (above) and (b) the mass and solute flux at the subdomain interface within the simulation domain. 104

5.25 Flow chart outlining the sequential one-way coupling process for the solute prediction and validation within the continuous casting process at a steady state. 105
5.26 Linear approximation of the binary Fe-C equilibrium phase diagram, along with the corresponding Fe-C-Mn pseudo-binary phase diagram at 1.55 and 2.14 wt.%Mn. 105
5.27 (a) Influence of grain size on the flow rate and pressure drop assuming g_s=0.92; (b) corresponding solute maps for each of the six cases. 107
5.28 Predicted flux, pressure, and Mn concentration evolution within the entire mushy zone as a function of the subdomain number. The results presented represent the average value obtained at the subdomain interface. 109
5.29 Influence of solid fraction gradient on the solute distribution. The subdomains correspond to subdomain number in Fig. 5.28: (a) subdomain 1,(b) subdomain 20, (c) subdomain 26 and (d) subdomain 27. 110
5.30 Solute mapping images of micro-segregation of Mn examined by MXRF in the section near centre of the continuously cast slab. 111
5.31 Comparison of solute distribution via experimental measurement and 3D mesoscale solute transport model. 113
5.32 Influence of strain rate on the solute distribution. The influence of strain rate on the incoming flux and pressure drop are also shown below. 114
5.33 Influence of carbon contents on the solute distribution of Mn. 115

List of Tables

4.1 List of parameters used for δ and γ phase in the simulation [3]. 55
4.2 Chemical compositions of the sample test in Gleeble machine [27] (wt.%) 66
5.1 List of parameters used in the simulation for Fe–C alloy [28, 29, 30, 31, 32] 70

Notation, Definitions, and Abbreviations

Notation

$A^{\alpha/\beta}$	Interfacial area between the α and β phases
A_c	Characteristic value
b^e	Load vector
c_s^*, c_l^*	Solute concentration in the solid and liquid phases of a binary alloy at the solid/liquid interface
$c^{\alpha/\beta}$	Solute concentration of the phase interface on the α side
D_k	Diffusion coefficient in the phase k
$\dot{E}$	Cumulative average deformation over the depth of the mushy zone
F_{oT}	Fourier number related to temperature
F_{os}	Fourier number in solid phase related to diffusion
G	Thermal gradient
G_l	Free energy of liquid phase per unit volume
G_s	Free energy of solid phase per unit volume
g_s	Volume fraction of solid
g_l	Volume fraction of liquid
g_δ	Volume fraction of δ phase

g_γ	Volume fraction of γ phase
g_g	Volume fraction of dendrite envelope
g_{id}, g_{l_intra}	Volume fraction of intra-dendritic liquid
g_{ed}, g_{l_extra}	Volume fraction of extra-dendritic liquid
g_l'	Internal liquid fraction inside the dendrite envelope
g^α	Volume fraction of of an individual phase within each zone
$\vec{g}$	Acceleration due to gravity, 9.82m s^{-2}
h	(Half) channel width
$\widehat{h}$	Critical half liquid channel width for coalescence when corner rounding is considered
I	Unit tensor
k	Partition coefficient
K_l	Bulk modulus of liquid
K_s, K_o	Absorption coefficients for oxygen and sulfur on liquid iron
K_e	Strength coefficient
$[K]^e$	Element stiffness matrix
l^{id}, l^{ed}	Intra-dendritic and extra-dendritic liquid
L	Length of the element
L_e	Edge length
m_l	Liquidus slope
m	Strain rate sensitivity
N	Element shape functions in finite element method
n^*	Brittle temperature range exponent in Won's criterion
n	Strain hardening exponent
p_l	Liquid pressure
p_a	Atmosphere pressure

Q	Solute transfer rate at the solid/liquid interface due to solute partitioning
Q_a	Activation energy for deformation
R	Gas constant
r	Radius
S_s	Interfacial area concentration of solid/liquid interface
S_e	Interfacial area concentration of dendrite envelope
$S^{\alpha/\beta}$	Interfacial area concentration between α and β phase
S_l^e	Total lateral area of the two tetrahedral elements
S_{sl}^e	Solid/liquid interfacial area within an element
T_{liq}	Liquidus temperature
T_f	Equilibrium melting temperature
T	Temperature
$\dot{T}$	Cooling rate
$T_{k,start}$	Transformation temperature of the k phase
t_v	Time spend in the vulnerable region
t_r	Time spend with the solid fraction ranges from the 0.4 to 0.9.
t_{99}, t_{cr}, t_{40}	Time at solid fractions equal to 0.90, 0.40 and critical value determined by Feurer's criterion
V	Total volume of the domain
V_{liq}	Volume of liquid present in an element
V_l^e	Total volume of the two facing tetrahedrons
V^e	Total volume of dendrite envelope within an element
$v_n^{(1)}$	Boundary velocity of zone (1)
v_T	Velocity of the solidification front
$\vec{v}_s$, $\vec{v}_l$	Velocity of the solid and liquid phase

$\vec{v}^{ed}$	Fluid velocity in the extra-dendritic region
$\vec{v}^{id}$	Fluid velocity in the intra-dendritic region
$v^{\alpha/\beta}$	Normal velocity of the phase interface on the α side
x, y, z	Global Cartesian coordinates
x', y', z'	Local Cartesian coordinates
α	Half of the supplementary angle of the grain corner angle
λ	Surface tension at the atmosphere-liquid interface
λ_2	Secondary dendrite arm spacing
$\ell_{ed/\mathrm{i}d}$, $\ell_{s/\mathrm{i}d}$	Characteristic diffusion length in the extra-dendritic and solid phase
$\ell^{\alpha/\beta}$	Diffusion length in the α phase
φ	Constant in Won's criterion
σ	Stress
σ_e	Effective stress
ε_c	Critical strain
$\dot{\varepsilon}$	Strain rate
$\dot{\varepsilon}_e$	Effective plastic strain rate
$\dot{\varepsilon}_{sv}$	Volumetric part of the strain rate imposed on a mushy zone ($\dot{\varepsilon}_{sv} = \dot{\varepsilon}_{xx} + \dot{\varepsilon}_{yy} + \dot{\varepsilon}_{zz}$)
ε_e	Effective plastic strain
η	Thickness of diffuse solid/liquid interface
γ_{ex}	Excess energy
γ_{sl}	Interfacial energies of the solid-liquid interface
γ_{gb}	Interfacial energies of the (dry) gain boundary
Γ	Gibbs-Thomson coefficient
μ_l	Dynamic viscosity of the liquid phase

ρ_k	Density of the phase k
$\Delta p_{l,\max}$	Pressure drop over a small volume element
$\Delta p_{l,\max}^{\varepsilon x}$	Pressure drop due to deformation
$\Delta p_{l,\max}^{\beta_s}$	Pressure drop due to shrinkage
Δs_f	Volumetric entropy of fusion
ΔT	Undercooling
ΔT_b	Coalescence undercooling
ΔT_B	Brittle temperature range
Δv_{liq}	Volumetric flow rate required to compensate for deformation
β_s	Solidification shrinkage coefficient
κ	Permeability of mushy zone
$\kappa(g_l{}')$	Local permeability within the dendrite envelope
$\langle c_k \rangle^k$	Intrinsic solute concentration in the phase k
Ω	Supersaturation
Iv^{-1}	Inverse of Ivantsov equation
$\vee$	Additional liquid volume due to the rounding edge
$\{\phi\}^e$	External boundary conditions
δ	Delta-Ferrite
γ	Gamma-Austenite

Abbreviations

AHSSs	Advanced High Strength Steels
BCC	Body-Centered Cubic
CAFE	Corporate Average Fuel Economy
CP	Complex Phase
CA	Cellular Automaton

DP	Dual Phase
DSM	Dendritic Solidification Module (Model)
DFFM	Dendritic Fluid Flow Module (Model)
EPMA	Electron Probe Micro Analyzer
FSV	Future Steel Vehicle
FP	Fundamental Parameter
GHG	Greenhouse Gas
HCS	Hot Cracking Susceptibility
L-IP	Lightweight Steels with Induced Plasticity
LS	Least Squares
LIT	Liquid Impenetrable Temperature
MPC	Multi-Point Constraint
MART	Martensitic
RVE	Representative Volume Element
SCN	Succinonitrile-acetone
SSCT	Submerged Spill Chill Tensile Test
SDM	Semisolid Deformation Module (Model)
SCM	Semisolid Cracking Module (Model)
SDD	Silicon Drifted Detector
SBIP	Shear-Band-Induced Plasticity
TRIP	Transformation-Induced Plasticity
TWIP	Twinning-Induced Plasticity
ULSAB	Ultralight Steel Auto Body
XRF	X-Ray Fluorescence
ZST	Zero Strength Temperature
ZDT	Zero Ductility Temperature

Chapter 1

Introduction

This chapter provides an overview of Advanced High Strength Steels (AHSSs) including their background, categories, advantages over conventional grades as well as the challenges associated with the production process due to casting defects. This is followed by an introduction of the continuous casting process for AHSSs, and typical solidification defects: segregation and hot tearing. The chapter ends by outlining the main goals of this work and the chapters of this thesis.

1.1 Overview

In 1960, continuous casting of steel was introduced commercially after overcoming great technical difficulties. This process is favored worldwide owing to its inherent advantages of high production yield, low cost and great operational flexibility [33]. Yet, during the casting process, defects such as hot tearing and macrosegregation will occur; these can be observed throughout the cast slab section [34]. For steel grades having high alloy contents such as AHSSs, transverse cracks and centreline cracks induced by hot tearing and macrosegregation occur relatively commonly. Continuously-cast steel products with severe defects usually contain reduced mechanical properties and must be down-graded. The occurrence of these cracks and centreline segregation is also very detrimental in terms of damage to downstream equipment. Although numerous efforts have been made to avoid hot tearing [34, 35], the availability and accuracy of models to predict their occurrence remains inadequate.

Due to the high temperature at which hot tearing and segregation problem occur in steels, the semi-solid state, and metal opacity, experimental investigations are limited. Instead, simulation methods for predicting hot tearing susceptibility and segregation have been developed. However, modeling the formation of these defects during the continuous casting process still remains a big challenge for metallurgists, since these casting defects result from the

combination of a series of physical phenomena: liquid feeding, deformation, and segregation [12]. Accurate prediction of hot tearing and segregation requires the complex coupling of these various interacting phenomena. In order to shed light on the formation of defects, numerous criteria have been proposed to predict the susceptibility of an alloy/process combination to the formation of hot tearing (e.g. [36]); however these criteria are not able to quantify the location and severity of hot tears. The models used to predict macrosegregation are also known to have shortcomings such as heavy computational cost and strong dependence on the input parameters [37]. In this thesis, a 3D meso-scale and multi-physics model is proposed to predict hot tearing formation and centreline segregation during the continuous casting of AHSSs by coupling relevant physics together in a comprehensive modeling framework.

1.1.1 Background of AHSSs

The world's most popular material, steel, has extensive applications in automotive vehicles, skyscrapers, rails constructions and planes simply due to its functionality, high strength, great adaptability and good machine-ability [38]. Today's industries, particularly automotive manufacturers, will continue using steel as a key material but call for the development of new grades of steel with lighter weight to reduce fuel consumption and environmental damage while maintaining a sound ecosystem. This is due to the fact that automotive manufacturers need to meet the Corporate Average Fuel Economy (CAFE) standards which was proposed to improve transportation efficiency and reduce environmental emissions [4]. The CAFE standards were expanded in 2009 to include greenhouse gas (GHG) emissions limits for year 2012-2016. Fig. 1.1 shows the historical performance of passenger car fuel efficiency, as well as future targets. For Canada, the enacted target will reach to 55 miles per gallon in the year 2025. Although other materials such as Al and Mg can alternatively be used for weight reduction, the lower cost of steel products is more attractive to automotive manufacturers.

1.1.2 Advantages of AHSSs

AHSSs grades significantly outperform conventional steels for the automotive applications due to several advantages. First, AHSSs are known for having high yield strengths and high work hardening rates [39]. The strength properties of AHSS grades have been roughly defined as a yield strength $\geq$300 MPa, a tensile strength $\geq$600 MPa [39], and an elongation between 20-30% [40]. Because of these properties, AHSSs grades offer a reduction in weight without compromising safety and load bearing performance [38]. Second, AHSSs have excellent fatigue behavior and outstanding energy absorbing

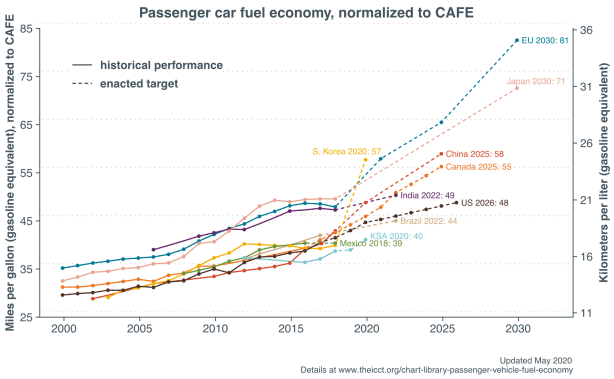

Figure 1.1: Targets for passenger vehicle fuel efficiency in nine countries [4].

properties [41, 42]. This makes these grades highly competitive as compared to other options for automotive materials. Other advantages include flexible performance, low cost, and superior recyclability [38]. According to the previous research [43], the use of AHSSs in North American vehicles has risen significantly over the past ten years and is expected to double from 254 pounds per vehicle weight in 2014 to 483 pounds by the year of 2025.

1.1.3 Classification and challenges for application of AHSSs

The outstanding mechanical properties of AHSSs grades lie on the multi-phase complex microstructures, based on which the AHSSs can be classified in three different categories. Fig. 1.2 shows the mechanical properties of various categories. The 1st gen. of AHSSs consist of primary ferrite-based microstructure including dual phase (DP), transformation-induced plasticity (TRIP), complex-phase (CP) and martensitic (MART) steels. However, due to the lean compositions and ferritic-related dominated phases in first generation AHSSs, second gen. AHSSs were developed consisting of high alloy austenitic steels such as the twinning induced plasticity (TWIP) steels, lightweight steels with induced plasticity (L-IP) and shear-band-induced plasticity (SBIP) [39, 44]. The 2nd gen. AHSSs exhibit superior mechanical properties, however, their high cost due to Mn and Al additions and complex manufacturing process have prevented them from achieving wide usage [5]. For example, TWIP steel, with high Mn, is likely prone to delayed cracking and suffers from embrittlement susceptibility [45]. Other challenging issues include poor castability, difficult hot working conditions, and poor corrosion resistance [46, 5].

The 3rd gen. AHSSs, currently being developed, aim to obtain mechanical properties in between the 1st and 2nd gen. They will be steel alloys with a good combination of strength and ductility, greater than those exhibited by the first gen. AHSSs but at a lower cost compared with the second gen. AHSSs,

and with strength ≈1000-1500 MPa along with an elongation of 20-30% [5]. The timely development of 3rd gen. AHSS grades are considered to be of vital importance to sustainability within the automotive industry [44, 39].

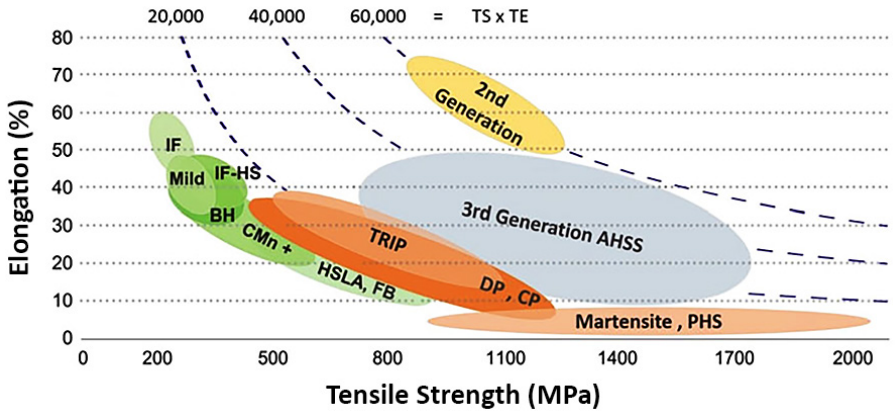

Figure 1.2: Elongation-tensile strength diagram for various steels [5].

1.2 Solidification during the AHSSs continuous casting process

Continuous casting is a mature technology undergoing improvements over decades [47]. A typical schematic of the process is shown in Fig 1.3. The needed equipment consists of a copper mold providing primary cooling, spray nozzles providing secondary cooling, and rollers upon which the casting travels through the system.

In the continuous casting process, molten steel fed from the tundish is introduced to an oscillating, water cooled mold with an open exit. The mold oscillates to help avoid the sticking between the solidified shell and the copper mold. The process starts with a mold blocker located at the mold bottom. Once the liquid is poured into the mold through a nozzle, the metal starts to solidify against the copper mold and the starter block due to the heat extraction. When the solid shell grows with a certain thickness, the block will be gradually withdrawn while the molten metal is continuously fed into the mold to maintain a relative even meniscus level. A layer of slag is often used to cover the molten meniscus to provide the metal with thermal and chemical insulation from the atmosphere and to absorb alumina inclusions.

The solid shell, having a known thickness, is vertically oriented as it exists the mold. A series of motor-driven rolls below the mold gradually withdraw the product from the vertical direction to the horizontal direction over a length of

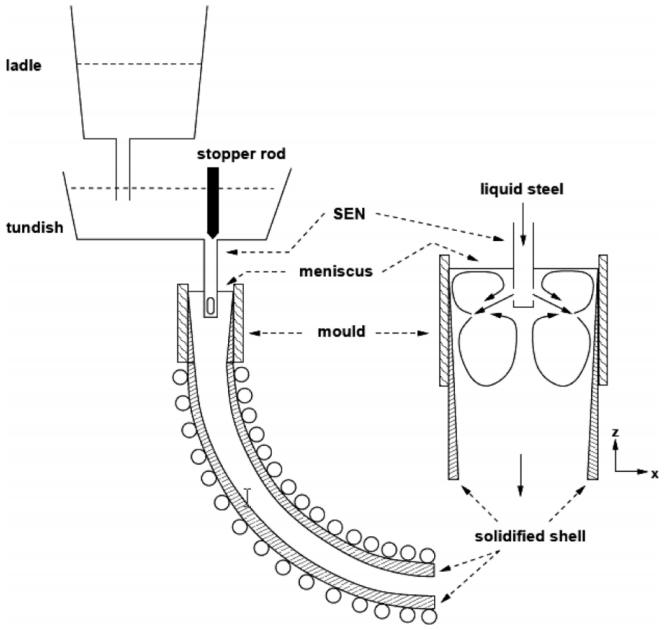

Figure 1.3: Schematic diagram of the continuous casting apparatus along with a flow pattern inside the mold [6].

∼10 m. Additionally, these support rolls also help to prevent bulging caused by the ferrostatic pressure. Between these support rolls, high-pressure nozzles are used to spray water on the product surface to extract the latent heat of fusion at the solidification front as well as the heat of phase transformation from the solidified steel as well as heat related to the high temperature. Once the casting steel reaches a length convenient for further processing, it is subjected to torch cutoff into individual products. As-cast steel product shapes include billets (square cross section with thickness less than 150 to 175 mm), thick slabs (wide rectangular cross section with thickness between 50 and 300 mm), thin slabs (thickness between 50 and 75 mm), strips (thickness between 1 and 12 mm), and rounds/extrusion billets (100 to 500 mm in diameter) [48].

Solidification during continuous casting involves a complex interplay of heat transfer processes. The molten metal, entering the mold through a ceramic nozzle, brings the heat. Then, heat transport inside the mold and the mold/metal interface influences the initial solidification behavior as well as the growth of a solidified shell [48]. The heat transfer rate varies with time and location. Near the meniscus, the molten metal is in contact with the water-cooled mold, which makes heat transfer very efficient. Steel tends to shrink upon cooling, ultimately resulting in the cast surface being rough, and the formation of an air gap which impacts the heat extracted through the mold. The shrinkage gap forming near the corner and spreading across the lateral faces

is compensated by utilizing a tapered mold to facilitate the cooling [49, 50]. It was reported that 40% of the total superheat and about 30% of the total sensible heat can be removed by primary cooling [51].

1.3 Solidification defects of AHSSs during casting

Solidification defects are occurring both in the mold as well as below the mold observed in different microstructures. Dendrite growth is the most common crystallization mechanism observed during continuous casting of steel. The morphology characterized by the dendrite arms is associated with the formation of secondary phases and casting defects, most notably hot tearing, porosity and segregation [52, 53]. Advanced continuously-cast high strength steel slabs with high levels of alloying elements as well as complex shape castings are quite prone to these defects which have plagued the continuous casting process for decades [54].

1.3.1 Hot tearing

The occurrence of hot tearing, is a multi-scale problem, and has been known to be related directly to the flow of liquid through the dendritic network at the microscale [20], due to the concomitant phenomena of solidification induced shrinkage and mushy zone deformation. A typical crack, from a thin slab caster, is shown in Fig. 1.4. This figure shows the internal half-way crack observed in the longitudinal cross section of as-cast slabs, along with the surrounding microstructure.

This defect occurs in metallic alloys during the semi-solid state and is caused by a lack of liquid feeding to compensate solid network openings induced by tensile and shear strains [12]. The rapid cooling during the initial solidification of continuously-cast steel leads to steep temperature gradients, resulting in large thermal strains as the slab contracts or expands within the mold [34]. The hot tears formed within the mold will be subjected to thermal strain along with mechanically induced strains caused by the roll pressure, ferrostatic pressure, machine misalignment, bending and straightening operations, any of these strains and stresses will accelerate the formation and propagation of the crack [34].

Reports have shown that the mechanical properties of semi-solid steel display a ductility trough over a critical solid fraction range known as the brittle temperature range where the liquid behaves as an extremely brittle phase [8]. A typical schematic of the ductility trough at high solid fractions near the solidus temperature of columnar grains is shown in Fig. 1.5. In this schematic,

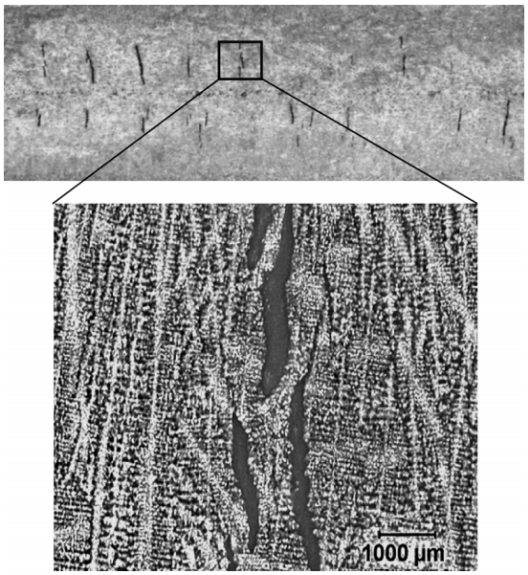

Figure 1.4: Typical hot tears observed within steel slabs [7].

several critical points can be identified in terms of solid fraction and temperature [8] that characterize the brittle temperature range and thus the range in which hot tears are prone to forming:

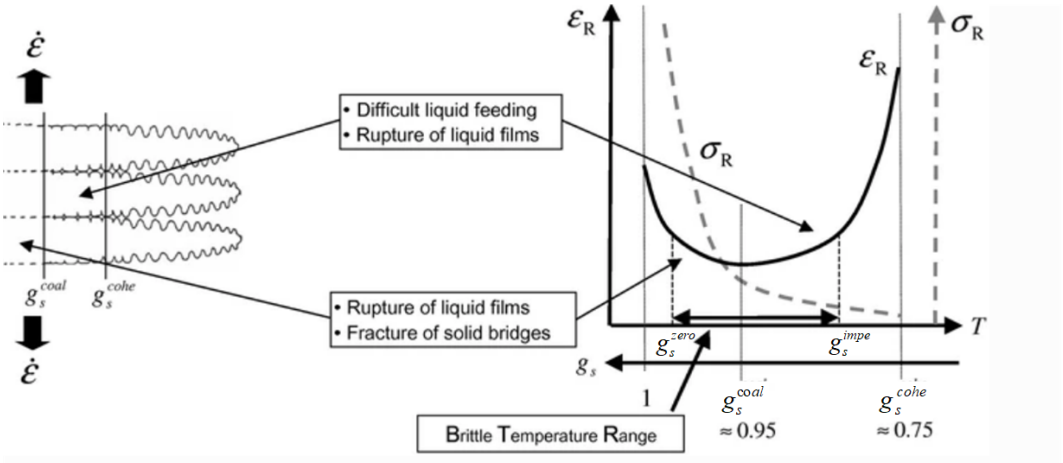

Figure 1.5: Schematic diagram of mechanisms of hot tearing in steels [8].

Coherency point, g_s^{cohe}

g_s^{cohe} represents the point at which secondary arms are beginning to touch the neighbouring ones, while still allowing liquid to pass through them. When a semisolid reaches the coherency point, the solid skeleton is continuous and can

withstand slight deformation.

Liquid impenetrable point, g_s^{impe}

Liquid impenetrable point is defined as a semi-solid solid fraction where the dendrites are compact and impede the liquid feeding. Inadequate liquid feeding results in the formation of porosity or a rupture of a liquid film if the semisolid is subjected to deformation. The ductility of a semisolid will decrease with the increase of solid fraction until it reaches to the coalescence point.

Coalescence point, g_s^{coal}

g_s^{coal} is defined as the solid fraction when the disappearance of a liquid film between two distinct grains occurs, forming a solid grain boundary as well as isolating liquid pockets. The semisolid at the coalescence point is strong enough to withstand large deformation and is ductile. Hot tearing is not likely to occur once the solid fraction is greater than the coalescence point.

Zero ductility temperature, g_s^{zero}

g_s^{zero} corresponds to the point when a solid fraction is very high and little porosity remains. The ductility and strength both increase began at this point until complete disappearance of the liquid phase.

Hot tears are prone to occurring between the zone identified by g_s^{cohe} and g_s^{impe} where the material is known to be extremely brittle [8]. The problems become more severe for steel grades having carbon contents between 0.09 and 0.17 wt.% which covers the peritectic range [55]. Once a hot tear forms within a casting, it represents an irreversible failure that needs to be repaired or cut off.

1.3.2 Macrosegregation

In addition to hot tearing, inhomogeneity in solute distribution within a metal alloy can also occur during casting. This defect, known as segregation, occurs at different length scales; macrosegregation refers to composition differences over a large spatial scale whereas microsegregation refers to composition differences on the scale of the inter-dendritic spacing. Macrosegregation is a result of two fundamental mechanisms: flow of solute-enriched liquid through the mushy zone containing solidifying dendrites and transport of solid grains or grain fragments throughout the liquid pool [29]. Gradual solute enrichment of the liquid occurs as a result of solute partitioning during solidification, due to the low solubility of most alloying elements in the solid as compared to the

liquid. The fundamental mechanism to cause macrosegregation is the movement of the enriched or depleted liquid and the transport of solid grains in the mushy zone [29].

Macrosegregation is one of the most unavoidable problems in continuous-cast steel due to the inter-dendritic flow caused by shrinkage, changes in liquid density [56] induced by temperature variations, mechanical deformation [57] and electromagnetic forces [58]. Segregation along the centreline, known as centreline macrosegregation, is often considered as the initiation site for cracking and porosity [59]. Although microsegregation can be eliminated during heat treatment, it is not possible to achieve long-range chemical homogeneity thus eliminating macrosegregation once casting is complete due to the large length scales. Final products with severe macrosegregation usually end up with reduced mechanical properties and are sold at reduced cost. Although strategies such as electromagnetic stirring, soft reduction and intense cooling have been used to minimize this effect [60], great interest remains in determining strategies that eliminate this defect during continuous casting [37].

1.4 Outline

This thesis proposes the use of a multi-scale and multi-physics model to investigate hot tearing and centreline segregation during the continuous casting process of steel. The model is also used to predict the microstructure morphology transitions from individual dendritic grains to a percolated solid network, the effects of the peritectic transformation, and permeability variations within a semisolid. The model is validated experimentally using X-ray fluorescence data and the measurements from the semisolid tensile test experiment.

This thesis is organized in a following order:

Chapter 2 describes the principles of hot tearing and macrosegregation during solidification, including a review on the basic knowledge, pertinent experimental investigations, and key numerical simulations.

Chapter 3 presents the scope and objectives of this thesis. This includes a short review of the gaps in the previous models and key improvements.

Chapter 4 presents the methodologies used in this thesis, including the model development and the experimental set up used for validation.

Chapter 5 reports the application of the model to various conditions and the corresponding results. Validations of the model results with experimental measurements are also presented.

Chapter 6 summarizes all contributions of this thesis and concludes with model limitations and suggestions for future work. The industrial applications of the current model are also discussed.

Chapter 2

Literature Review

Solidification defects including hot tearing and macrosegregation are examples of multi-scale and multi-physics problems. The microstructure and fluid flow occur at the microscale while stress develops at the macroscale. The key phenomena include alloy segregation during solidification, fluid flow within the intra-dendritic and extra-dendritic regions, and deformation of the mushy zone. Experimental investigation of the mechanisms behind these phenomena has provided much knowledge for developing numerical models that have greatly reduced the occurrence of these detrimental defects. Nevertheless, prediction of hot tearing and macrosegregation is extremely difficult, especially during the continuous casting process [47].

This chapter consists of three parts: solidification, segregation, and hot tearing. First, the fundamentals of solidification path for steel alloys and coalescence at the end of solidification are reviewed. Second, experimental characterizations of macrosegregation are presented followed by a review of numerical investigations including both existing microsegregation models and macrosegregation models. Thirdly, both experimental and numerical investigations of hot tearing are presented: experimental works including hot tearing sensitivity test, mechanical test and observation of hot tearing; macroscopic hot tearing criteria and continuum model of hot tearing; and prior researches on multi-physics modelling of hot tearing as well as the applicability of these models to steel alloy systems and the continuous casting process.

2.1 Solidification

2.1.1 Solidification path in AHSSs

Phase diagrams are useful tools to provide insights on the solidification path of advanced high strength steels. A phase diagram provides the existing phases at specific temperature and composition at equilibrium state, usually assuming

a fixed pressure.

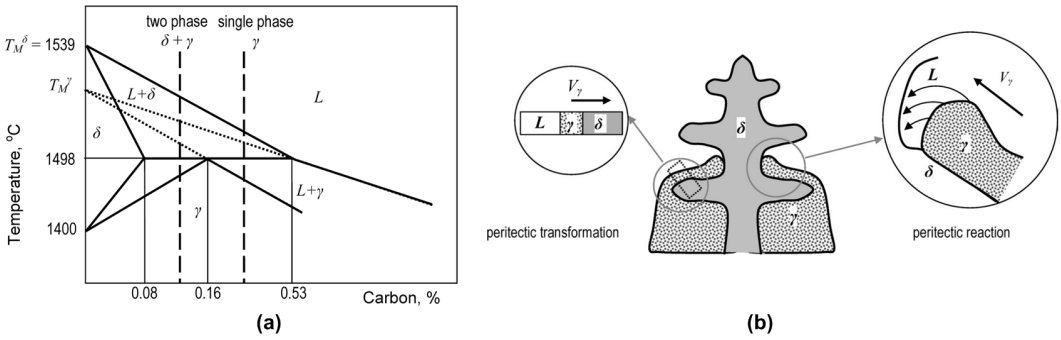

Figure 2.1: (a) A Fe-C binary phase diagram and (b) mechanism of peritectic reaction and transformation during solidification [9].

Fig. 2.1(a) shows a typical example of Fe-C diagram at high temperatures. The phase diagram clearly indicates the boundaries between different phases. For alloys with carbon contents between 0.16 wt.% and 0.53 wt.%, the solidification sequence can be easily identified: primary solidification $L \rightarrow \delta$, peritectic reaction $L + \delta \rightarrow \gamma$, followed by the sequential peritectic transformation. A schematic diagram illustrating the mechanism of the peritectic reaction and transformation is shown in Fig. 2.1(b). Initially, the primary δ phase forms followed by the peripheral growth of γ phase during peritectic reaction. Once the peritectic reaction is over, the γ grows and consumes both liquid phase and δ phase. For multi-component alloys, a pseudo-binary phase diagram of alloys containing different compositions can also be calculated with the help of modern thermodynamic software such as ThermoCalc [61] and FactSage [62], and is useful to identify the existing phases.

In reality, an equilibrium state is hard to achieve during solidification due to inadequate time for complete diffusion of solute and heat [12]. This implies that there is always a concentration gradient in each phase, i.e. segregation. However, it often assumes that a local equilibrium at the phase interface is satisfied. The solute partitioning between the solid and liquid is controlled by the partition coefficient, also known as segregation coefficient, $k = c_s^*/c_l^*$, where c_s^* and c_l^* represent the equilibrium concentrations in the solid and liquid phase at the temperature of interest.

The evolution of solid fraction can be predicted using various modelling approaches, each containing different assumptions, and thus obtaining segregation profiles as a result of solute partitioning and diffusion in each phase. Often, the liquidus and solidus lines of the phase diagram are linearized in order to obtain a constant partition coefficient thus simplifying the simulation. Casting defects such as hot tearing and segregation are likely to form during solidification. Note that hot tearing is likely to occur at high solid fraction

due to the inadequate liquid feeding [12] prior to coalescence, while segregation occurs throughout the whole process and at different length scales. The definition of coalescence will be reviewed hereafter followed by microsegregation models and macrosegregation models.

2.1.2 Coalescence during solidification

At the end of solidification, when two grains with different orientations are about to touch each other, a driving force is needed to determine the non-equilibrium temperature when they will coalesce and form a solid bridge [63]. Solidification of the last liquid film depends on the interfacial energies of the (dry) gain boundary, γ_{gb} and of the solid-liquid interface, γ_{sl} [63]. For a pure metal, the excess free energy of two interfaces approaching each other at the melting temperature deviates from γ_{sl} until it equals γ_{gb} when the liquid channel has completely disappeared. The expression of the excess energy γ(h) as a function of channel width (h) at the melting temperature is given by

$$\gamma\left(h\right) = 2\gamma_{sl} + \left(\gamma_{gb} - 2\gamma_{sl}\right) \exp\left(\frac{-h}{\eta}\right), \tag{2.1.1}$$

where η represents the thickness of diffuse solid/liquid interface ($\eta \sim$1-3 nm) [64] (note – coalescence phenomena can only be felt at this length scale). The forces between two grains can be categorized into three cases: attractive ($\gamma_{gb} < 2\gamma_{sl}$), neutral ($\gamma_{gb} = 2\gamma_{sl}$), and repulsive ($\gamma_{gb} > 2\gamma_{sl}$). At other temperatures, the excess free energy $G\left(h\right)$ (per unit area) resulting from supercooled liquid is given by

$$G\left(h\right) = \left(G_l - G_s\right) h + \gamma\left(h\right) = \Delta s_f h \Delta T + \gamma\left(h\right), \tag{2.1.2}$$

where G_l and G_s are the free energy of liquid and solid phase per unit volume, Δs_f represents the volumetric entropy of fusion, and ΔT is the undercooling relative to the melting temperature. Rappaz et al. [63] combined Equations 2.1.1 and 2.1.2 to show that stable liquid films will remain between two grains below the equilibrium solidification temperature until a coalescence undercooling (ΔT_b) is reached,

$$\Delta T_b = \frac{\gamma_{gb} - 2\gamma_{sl}}{\Delta s_f \cdot \eta}. \tag{2.1.3}$$

As can be seen in Eq. 2.1.3, the sign of the coalescence undercooling depends on the difference between γ_{gb} and γ_{sl}. In alloys, ΔT_b, is also influenced by solute enrichment in the liquid film due to microsegregation. Thus, the coalescence results in a shift downwards of the liquidus line by a certain solute undercooling.

2.2 Segregation

2.2.1 Experimental characterizations of macrosegregation

Numerous methods have been suggested in the literature to study macrosegregation experimentally, and in this section only a few methods commonly used in industries are covered.

Casting structure is considered to influence the severity of macrosegregation [65]. Eskin et al. [66] conducted some microstructure analysis on the casting samples through the optical microscope. The samples were well polished, cleaned and etched using different agents for revealing grain size and secondary arm spacings based on the composition inhomogeneity. They observed the coarse microstructure which was located near the center and varied under different casting conditions. Solidification structure and macrosegregation along centreline of a continuously cast slab was also investigated by Choudhary et al. [67] through sulfur printing. The presence of centreline segregation with a band width of around 10∼12 mm was clearly observed. The structure analysis provides useful insights into the macrosegregation features and can be used as a validation for the model's prediction in terms of microstructure and alloy distribution. However, the low sulfur contents within a steel sample often fail to indicate the severity of segregation and the solidification morphology. Quantitative analysis of the chemistry of a solidified sample is necessary as the solute inhomogeneity directly determines the mechanical properties of the material.

For quantitative analysis of the solute concentration distribution, Electron Probe Micro Analyzer (EPMA) measurements were performed on the steel sample from the ingot casting [68]. Yoshida et al. [10] used the same technique to investigate the influence of P on the microstructure of steel, and the solute distributions of species P and Mn within a small area of 2.56 mm×2.56mm is shown in Fig 2.2. The primary dendritic structure is visualized by the Mn-poor or P-poor area as solute is rejected from the solid phase during solidification. This method is capable to quantitatively indicate that the addition of P has a significant influence on the segregation. Other alternative approaches such as X-Ray analysis in the electron microscope, optical emission methods are rarely applied to macrosegregation analysis due to the fact they are very destructive and time consuming, and often restricted to small samples.

The experiments, especially large-scale experiments on industrial alloys upon real casting processes, are seldom done in the past mainly due to the challenges associated with shortage of equipment and expertise. X-Ray fluorescence (XRF) spectroscopy shows advantages over conventional methods

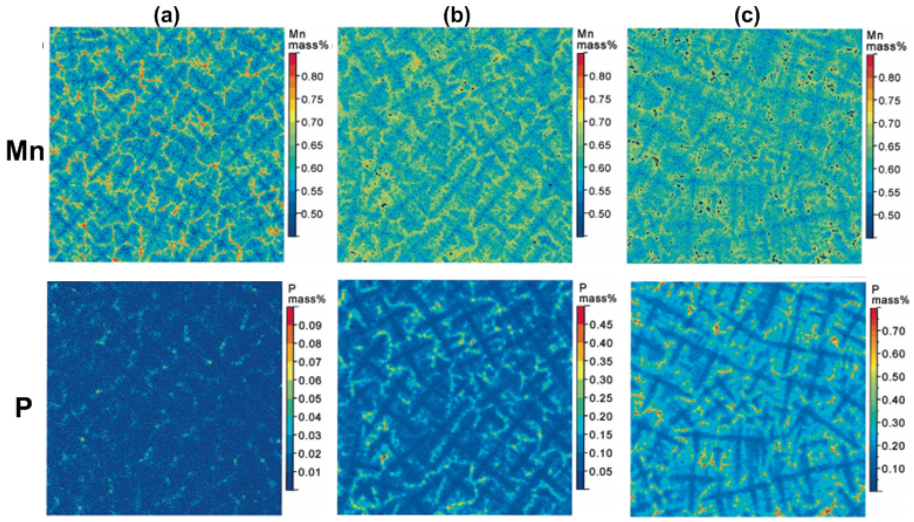

Figure 2.2: Solute mapping obtained from EPMA within a steel sample cut from continuously casting slab with different P contents: (a) 0.01 wt.%P, (b) 0.10 wt.%P and (c)0.20 wt.%P. [10].

mentioned above, and offers new possibilities to exam the chemical distribution at both microscale and macroscale. X-Ray fluorescence analysis is a well-established method for elemental analysis of a great variety of specimens. The advantages of the non-destructive or poorly destructive character and the ability to conduct simultaneous multi-element determinations with high sensitivity have made it applicable for the investigation of different materials. Additionally, the quantitative analysis via X-Ray fluorescence is known as a rapid and inexpensive technique with a simple sample preparation without acid digestion processes. It has been applied to investigate macrosegregation by Flemings for the first time in 1960s [69]. Fig. 2.3 shows a solute map for the steel ingot on a large scale obtained through XRF [11] for Cr and Mo. This large scale cross-section of the ingot was mapped for the first time with great details. The enriched solute of either Cr or Mo is located within channels along a direction antiparallel to the vertical direction, characterized as A segregation, can be clearly visualized; besides, the positive segregation at the top of the ingot is also observed. One of the limitations of XRF is that the carbon distribution within the sample can not be measured.

2.2.2 Numerical methods

Microsegregation Model

In addition to experimental investigation, numerical methods also help to provide insight into the segregation behavior. These models are often derived

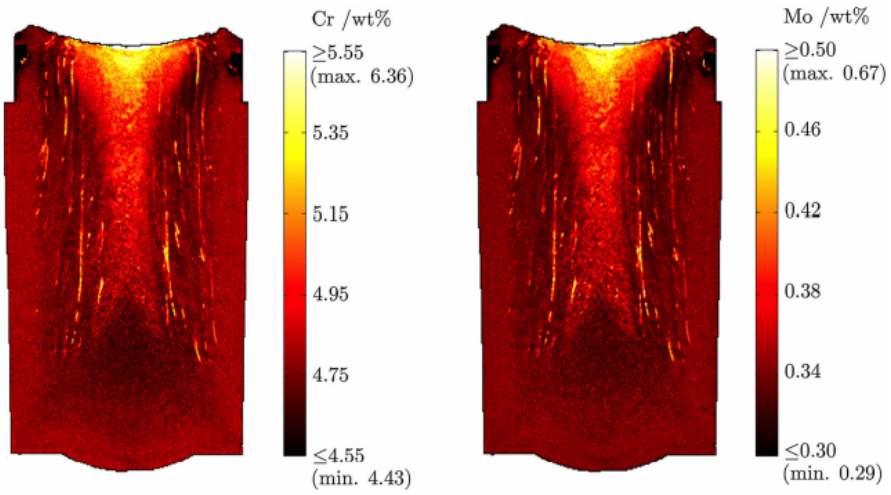

Figure 2.3: Solute mapping measured from XRF within a cross-section of a ingot sample for Cr and Mo [11].

based on the microstructure. The morphology of columnar dendrites of a solidified succinonitrile-acetone (SCN) alloy is shown in Fig. 2.4, where the primary dendrites and the secondary arms could be observed. An ideal schematic is shown on the right where an array of secondary dendrite arms growing parallel to one direction are assumed. This schematic is used to perform a 1D microsegregation analysis. Then the 1D microsegregation models are derived based on solute conservation over the black box shown in Fig. 2.4 at the scale of secondary dendrite arm spacing λ_2 under the assumption that the density of solid and liquid phase are equal and constant. The temperature within the black box is considered to be uniform due to a larger Fourier number Fo_T.

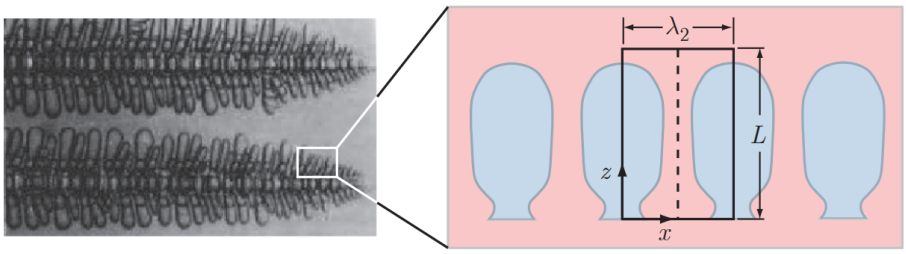

Figure 2.4: Columnar dendrites growing during solidification process of succinonitrile-acetone alloy (left) and a simplified schematic diagram of dendrite secondary arms used for microsegregation analysis [12].

The two simplest relations between the solid fraction and the alloy composition are Lever Rule and Gulliver-Scheil Equation. The Lever Rule presents the equilibrium solidification process by assuming complete mixing both in

solid and liquid phases at a temperature T, and solute rejected at the s/l interface contributes to the increment of solute concentration in both liquid and solid phases shown in Fig. 2.5(a). The equation is expressed as follows,

$$g_s = \frac{1}{1-k}\frac{T-T_{liq}}{T-T_f}, \tag{2.2.1}$$

where g_s is the solid fraction, T_{liq} is the liquidus temperature, and T_f is the melting point. The other extreme rule is the Gulliver-Scheil equation, which assumes no diffusion in the solid and complete mixing in the liquid along with a local equilibrium at the interface. The solute profile within the two phases can be found in Fig. 2.5(b). Note that the horizontal dashed line in Fig. 2.5(b) represents the average solute concentration in the solid phase $\langle c_s \rangle^s$. The solute rejected at the s/l interface is balanced by the increase in solute concentration in liquid phase only. Then Gulliver-Scheil equation derived based on the mass balance of the mushy zone is given,

$$g_s = 1 - (\frac{T-T_f}{T_{liq}-T_f})^{1/(k-1)}. \tag{2.2.2}$$

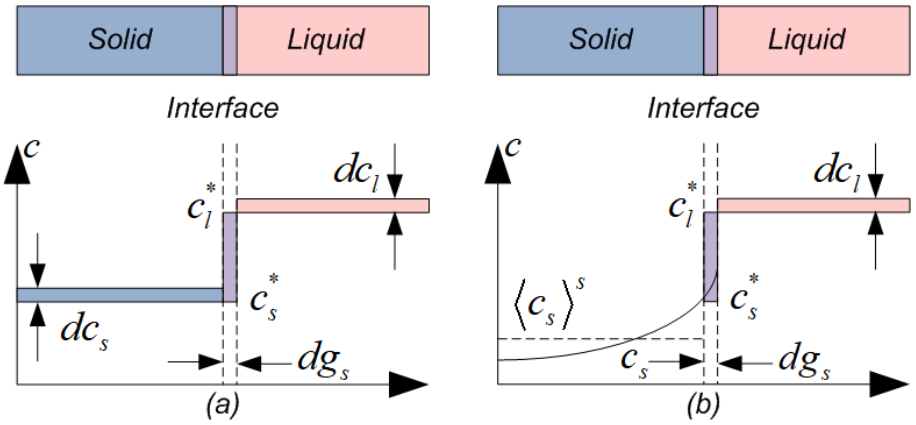

Figure 2.5: (a) Schematics illustrating the partitioning of solute from interface to liquid phase in (a) Lever Rule model and (b) Gulliver-Scheil model of microsegregation.

Lever Rule and Gulliver-Scheil equation represent two extreme cases: complete mixing or no mixing of the solid phase. Both Eq. 2.2.2 and Eq. 2.2.1 are independent of length and time scale. However, Gulliver-Scheil approximation is valid during rapid solidification such as laser welding [70]; Also, in reality, finite diffusion within the solid which referred as back-diffusion, does take place. The relative importance of back diffusion is determined by the Fourier number within the solid phase. Brody and Flemings [71] were the first to propose a microsegregation model that includes back diffusion, assuming

a uniform temperature and liquid is well mixed. The relation between solid fraction and temperature is given as,

$$g_s = \frac{1}{1-2kFo_s}\left[1-\left(\frac{T-T_f}{T_{liq}-T_f}\right)^{-(1-2kFo_s)/(1-k)}\right], \tag{2.2.3}$$

where Fo_s is the Fourier number in solid phase defined as $Fo_s = 4{\lambda_2}^2/D_s$ with D_s corresponds to the diffusion coefficient in the solid phase. However, the current Brody-Fleming model is only safe to use when Fo_s is less than 0.1, and it fails to guarantee solute conservation [12].

Clyne and Kurz [72] introduced a similar empirical expression based on the Fourier number to ensure that Eq. 2.2.1 can be reproduced when $Fo_s \to \infty$,

$$g_s = \frac{1}{1-2f\left(Fo_s\right)k}\left[1-\left(\frac{T-T_f}{T_{liq}-T_f}\right)^{(1-2f(Fo_s)k)/(k-1)}\right], \tag{2.2.4}$$

where the expression $f\left(Fo_s\right)$ is given by,

$$f\left(Fo_s\right) = Fo_s\left[1-\exp\left(-\frac{1}{Fo_s}\right)\right] - 0.5\exp\left(-\frac{1}{2Fo_s}\right). \tag{2.2.5}$$

Eq. 2.2.4 still fails to handle the solute conservation due to the fact that the solute diffusion in solid phase is not properly dealt with [12]. Other researchers, including Ohnaka [73] and Kobayashi [74] introduced alternative expressions of the Brody-Flemings equation to take into account of partial diffusion in the solid during solidification. Both models achieve a solute conservation, Ohnaka's model is an approximated solution under the assumption of parabolic distribution while the Kobayashi's model provides an exact solution to the back diffusion problem.

In the models mentioned above, Clyne-Kurz model is widely used due to its simplicity. Won et al. [56] extended the Clyne-Kurz model to multi-component systems with dendritic morphology characterized by λ_2, and considered phenomena such as coarsening and peritectic transformation. Won's model was applied to investigate the effect of cooling rate on the characteristic temperatures such as the zero strength temperature (ZST), zero ductility temperature (ZDT) and liquid impenetrable temperature (LIT) of a steel sample during solidification. The results indicate that cooling rate has a significant influence on ZST, LIT and ZDT due to the segregation behavior of the elements near the final stage of solidification.

However, the models mentioned above are all limited to 1D, and solute concentration inside a unit cell such as the black box shown Fig. 2.4 remains

constant without any solute exchange with the neighboring grains. It will cause a problem if non-constant density is included as it requires liquid feeding from neighboring grains to compensate solidification shrinkage; also coarsening introduced in these 1D model is not physically correct as coarsening results from the disappearance of dendrite arm due to incoming enriched solute flux [12].

A more elegant model based on an averaging approach over the microstructure was proposed by Wang and Beckermann [75]. The solidification model derived via this approach defines at least three phases intra-dendritic liquid l^{id}, extra-dendritic liquid l^{ed} and solid s phase. A dendrite envelope is introduced to distinguish the l^{id} and l^{ed} shown in Fig. 2.6(a). Wang and Beckermann assumed finite diffusion in solid and extra-dendritic liquid phase while the intra-dendritic liquid was well mixed, and the schematic profile of solute concentration can be seen in Fig. 2.6(b). Wang's model was also derived under following assumptions: uniform temperature over a representative volume element (RVE), densities of all phases are equal and constant, fluid flow is negligible. The controlling equations are derived based on three solute conservation equations of three phases(l^{id}, l^{ed} and s), and the LGK model [76] is used for predicting the dendrite tip velocity,

$$\frac{d\left(g_s + g_{id}\right)}{dt} = \frac{S_e D_l m_l \left(k-1\right) c_l^*}{\pi^2 \Gamma_{sl}} \left[Iv^{-1}\left(\Omega\right)\right]^2, \tag{2.2.6}$$

$$\frac{d\left(g_s \langle c_s \rangle^s\right)}{dt} = c_l^* k \frac{dg_s}{dt} + \frac{S_s D_s}{\ell_{s/\mathrm{id}}} \left(c_l^* k - \langle c_s \rangle^s\right), \tag{2.2.7}$$

$$\frac{d\left(g_{id}\langle c_{id}\rangle^{id}\right)}{dt} = c_l^* \frac{dg_{id}}{dt} + c_l^*(1-k)\frac{dg_s}{dt} - \frac{S_s D_s}{\ell_{s/\mathrm{id}}}\left(c_l^* k - \langle c_s\rangle^s\right) - \frac{S_e D_l}{\ell_{ed/\mathrm{id}}}\left(c_l^* - \langle c_{ed}\rangle^{ed}\right), \tag{2.2.8}$$

$$\frac{d\left(g_{ed}\langle c_{ed}\rangle^{ed}\right)}{dt} = c_l^* \frac{dg_{ed}}{dt} + \frac{S_e D_l}{\ell_{ed/\mathrm{id}}}\left(c_l^* - \langle c_{ed}\rangle^{ed}\right), \tag{2.2.9}$$

where g_s, g_{id} and g_{ed} represent the volume fraction of each phase, S is the interfacial area to the volume of the element, and subscripts s and e indicate the solid/liquid interface area and envelope area. m_l is the liquidus slope obtained from phase diagram. c_l^* is the equilibrium solute concentration in the liquid phase at a temperature of interest. D_l and D_s are the diffusion coefficient in liquid and solid phase, respectively. Γ_{sl} is the Gibbs-Thomson coefficient. $\langle c_k \rangle^k$ denotes the volume averaged intrinsic concentration of a phase k, and $\ell_{ed/\mathrm{id}}$ and $\ell_{s/\mathrm{id}}$ are the characteristic diffusion length in the extra-dendritic liquid and solid phase, respectively. The inverse of Ivantsov equation $Iv^{-1}\left(\Omega\right)$ can be approximated with the following equation with Ω denoting

solutal undercooling,

$$Iv^{-1}(\Omega) = \Omega = \frac{c_l^* - \langle c_{ed} \rangle^{ed}}{(1-k)\, c_l^*}. \tag{2.2.10}$$

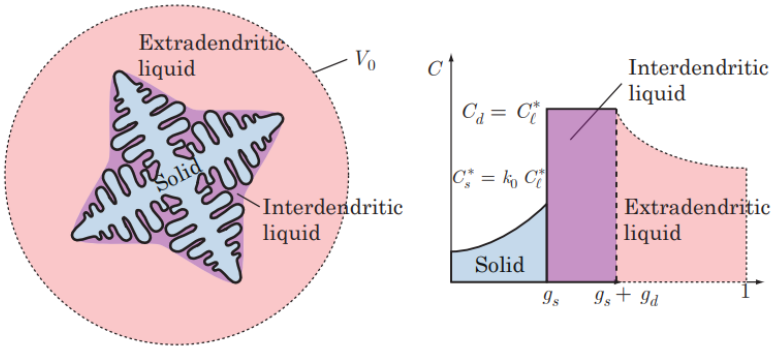

Figure 2.6: (a) A schematic of an equiaxed dendrite enclosed by an envelope and a solute profile in different phases [12].

The main advantage of this averaging approach is its ability to consider complex dendritic geometry and incorporate a dendrite growth model, which is able to simulate the evolution of phase fraction upon cooling without explicitly tracking the interfaces between the phases. This model was further extended to consider the diffusion in intra-dendritic region [77], and to investigate the relative movement between the solid and liquid phase and the permeability within a mushy zone [78].

Microsegregation predicted by the above models occurs at a scale of microstructure and will cause macrosegregation if liquid flow between grains is present.

Macrosegregation Models

Macrosegregation, as explained in Section 1.3.2, is a critical defect in casting products, and is commonly observed at the center of continuously cast semi-products, such as slabs and billets. Modeling macrosegregation is challenging due to the complex interplay between heat transfer, solute transport, fluid flow, solid deformation and the movement of the solid grains. Combined these require heavy computational cost at the scale of the casting [79].

Flemings and Nereo [80] were among the first to model the fluid flow induced by only shrinkage under the assumption of stationary solid phase and constant densities ($\rho_l \neq \rho_s$) for both liquid and solid phases. The microsegregation prediction was simplified using the Gulliver-Scheil model. Building

on this framework, Mehrabian et al. [81] introduced the intra-dendritic fluid flow during solidification by using the Darcy's law according to pressure drop model and gravity, and with a known temperature gradient as an input parameter. The bulk liquid flow was not considered in their works. The limitation was gradually removed with the development of multi-domain model where the moving boundaries of mushy zone and liquid zone were tracked and solved with corresponding different equations, and the prior decoupled model was extended by taking mass, momentum, solute and energy conservation equations into account [82]. In the late 1980s, macrosegregation was first predicted through a continuum model based on the mixture theory [83, 84]. A more robust and rigorous model developed by Ni and Beckermann [85] through volume average approach accounts for multiple phenomena during solidification, where the concentration is a treated as a mixture of both solid and liquid phases. This averaging volume approach is now commonly used to predict macrosegregation as intra-dendritic flow induced by solidification shrinkage, bulging, thermo-solutal buoyancy and the motion of equiaxed grain can be simulated at the macroscale. Založnik and Combeau [86] proposed a splitting scheme for the average volume solidification model to reduce the complexities associated with the coupling procedures while considering the movement of grains, which has been applied to predict the macrosegregation in DC casting [87].

2.2.3 Gaps in prior macrosegregation models

Macrosegregation prediction requires heavy computational cost; the coarse mesh size and simplifications introduced in order to make the computation time manageable sometimes fail to capture phenomena at the scale of the microstructure. Further, these models are strongly dependent on the input parameters and auxiliary models [37]. The selection of simplified Level-Rule, Gulliver-Scheil or Brody-Flemings microsegregation equations [88] have a significant effect on the solid evolution and thus solute concentration [37]. The mushy zone permeability will spatially vary due to the different local liquid fraction, flow tortuosity and semisolid microstructure, and requires a solution of the feeding at a microscale [81] and not simply the use of an analytical expression like Carman-Kozeny [89]. Evidence has also shown that macrosegregation cannot be accurately predicted without considering the morphology of the microstructure [79].

Based on these challenges, modeling macrosegregation during continuous casting is extremely difficult because, as identified by Thomas [47], it requires a comprehensive thermal/solutal model, a microsegregation model, a model for solute transport induced by shrinkage and mechanical deformation of the solid steel due to mechanical forces such as bulging, roll misalignment, unbending, and failure of the microstructure.

2.3 Hot tearing

2.3.1 Experiments investigation on hot tearing

As explained in Section 1.3.1, hot tearing is a casting defect within a semi-solid state formed due to a lack of liquid feeding while under tension or shear stresses. Many hot tearing tests have been developed to characterize this defect. In this section, different experimental tests used to investigate the hot tearing sensitivities, the mechanical properties of the alloys and the metallographic analysis of hot tearing are reviewed. These experiments help to investigate the influence of temperature, composition, applied deformation and other factors on the formation and propagation of hot tearing.

Hot tearing sensitivity tests

Many experimental apparatus have been developed over decades to assess the hot tearing susceptibility of alloys, the basic idea of these tests is to constrain the thermal contraction and shrinkage of a solidifying semisolid, thus inducing tensile stresses and consequently hot tearing [12]. The severity of hot tearing sensitivity of an alloy is often characterized by the length of a crack which is determined either through visual inspection of a solidified sample, or measuring the electrical resistivity during sensitivity tests [12]. The most common ways to test hot tearing sensitivity for steel include ingot punching test, bending test [90], constraint shrinkage test, while ring mold test [91], dog bone test [92] and cold finger test [93] are often used for aluminum alloys. Recently, Bellet et al. [8] developed a method, called the Crickacier hot tearing test, to investigate the hot tearing sensitivity of semi-solid steels. It basically belongs to the constrained shrinkage test.

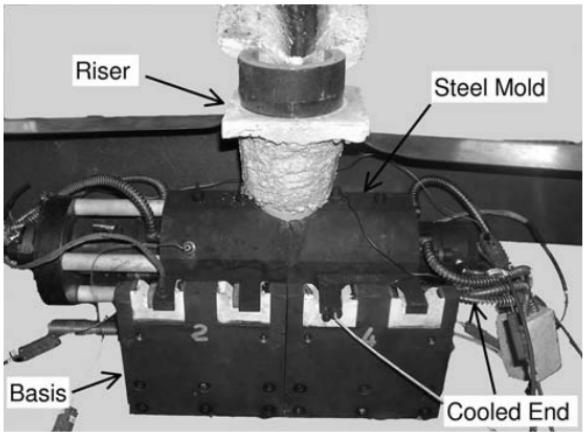

Figure 2.7: Schematic diagram of Crickacier hot tearing test [8].

The Crickacier test involves a feeder, two water-cooled chills, a mold insert and a mold as shown in Fig. 2.7. The casting specimen with a cone trunk shape is cooled at two ends, creating a central hot spot that acts to resist the thermal contraction as the specimen solidifies. Both ends of the specimen are constrained by the mold, thus causing tensile stresses perpendicular to the growth direction of columnar grains near the central hot spot. In this test, the thermal evolution along with the mechanical load are well controlled.

Mechanical tests

The empirical function to characterize the constitutive behavior of a semisolid is often derived based on accurate experimental measurements. Mechanical tests are able to show the loss of ductility and predict strain and stress evolution after a deformation is applied.

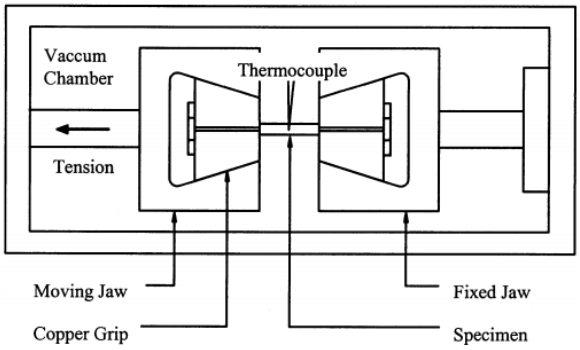

Figure 2.8: Schematic diagram of a Gleeble thermo-mechanical simulator [13].

Tensile tests: tensile testing semi-solid material has been found to be an effective method to predict the crack susceptibility of steel made by continuous casting process [94]. In the early 1960s, a group of researchers at Rensselaer Polytechnic Institute developed an apparatus called "Gleeble" to study the effect of temperature and high strain rates on the mechanical behavior of materials [95]. This apparatus consists of a high tensile testing apparatus and a high speed time-temperature control device, and is able to conduct various deformation tests under well-programmed temperature ranges and mechanical loading. It has been used to characterize the critical fracture stress for semi-solid steel [13]. The typical schematic diagram of the Gleeble system is shown in Fig. 2.8, where the control and heating systems are joined with a low force mechanical rig. The specimen is clamped between the two water-cooled jaws while heated by conductive resistance, and the horizontal tensile loads are applied through the mounted cylinder. The main advantages of the Gleeble test are the rapid heating system and well-designed temperature and deformation control systems, thus providing relatively accurate experimental

data [96]. However, it still remains uncertain if the experiment reproduces the actual continuous casting condition in terms of microstructure evolution and thermal history, also the nonuniformities of temperature distribution within such a small sample infer greatly on the mechanical properties [97]. Additionally, conducting a tensile test on a semisolid encounters numerous challenges due to the presence of intra-granular liquid within a semisolid when a tensile load is applied. The liquid film acts as an extremely brittle phase.

Another approach permitting the in-situ measurement of the mechanical behavior during solidification is called submerged spill chill tensile test (SSCT) [98, 99]. This test was initially proposed for the aluminum and aluminum alloys, and gradually applied to steel. Fig. 2.9 shows the two-piece chill body consists of water-cooled copper cylinder. The upper part of the chill cap is fixed to the support while the lower part is attached to the hydraulic cylinder, which allows for a constant separation rate between the two parts under an applied load through the rod. When the chill body is immersed into the molten steel, a solid shell forms over the surface. After a preset time, the solidified shell will be deformed in a direction parallel to the axis of the cylinder, and the columnar dendrites that have formed near the separation line between the two parts are pulled apart and the load is recorded simultaneously. The SSCT provides a similar condition for the hot tearing formation, and the result of the strength-elongation curve shows the real mechanical behaviors of the semi-solid state of steel during the initial solidification process [12]. The advantage of SSCT over the conventional test through the Gleeble-type machine is its contribution to obtain the mechanical strength of a solidifying shell; besides, the microstructure orientation is well controlled in respect to the tensile axis during the experiment [98].

Compression tests: the rheological behavior of a semisolid can also be predicted with a compression test by squeezing a sample either under a fixed load or a constant displacement rate between two parallel plates [100]. This experiment is often conducted on the semisolid with a solid fraction greater than 0.5 [101]. In a semi-solid sample, when compression is applied, the liquid will be squeezed out from liquid channels and pressure within the intra-dendritic liquid will increase [1]. This process can be related to solidification, where a solid/liquid interface moves towards a neighboring one with an increasing of solid fraction. When the compressibility of a semisolid drops to zero, it indicates that the liquid disappears and only fully solidified grains remain. The measurement of the amount of liquid squeezed out from a semisolid allows for the prediction of volumetric strain evolution and strain rates [96]. One example of the devices used to conduct the compression test is shown in Fig. 2.10. The specimen is placed in the cylindrical furnace equipped with quartz heat-resistant windows, and heated to a specific temperature prior to the compression. The applied force and displacement during compression are

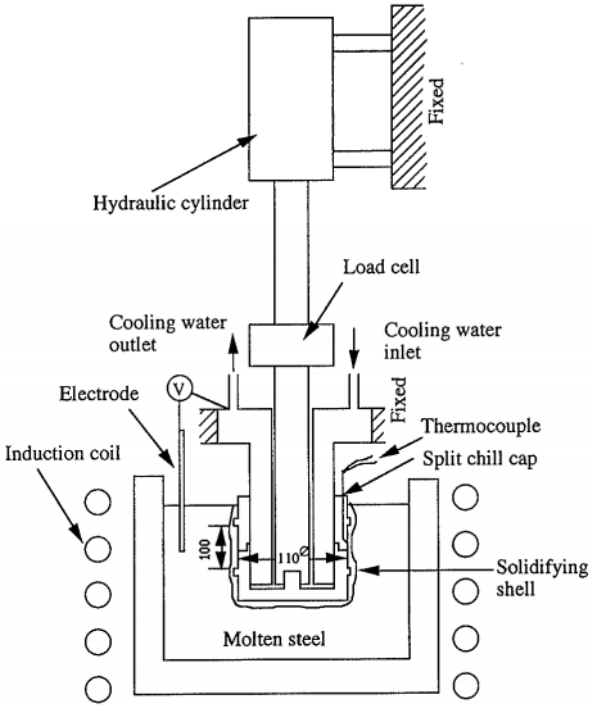

Figure 2.9: Schematic diagram of a submerged spill chill tensile test apparatus [14].

properly measured and the microstructure analysis can be done based on the quenched sample [15].

Observation of hot tearing

Fracture profile observation: experimental investigations of hot tearing also include fractography analysis of the samples, which help to better interpret the fracture mode at high temperatures and hot tearing mechanism. Xu et al. [16] performed a series of observations on the fracture surface of the Cr13 stainless steel produced by continuous casting at Baosteel. The bumpy surface of hot tearing was visualized as shown in Fig. 2.11(a). Fig. 2.11(b) indicates that the well developed dendritic structures coalesce and form dendritic bridges surrounded by a smooth inter-dendritic region which solidifies at lower temperatures due to the enriched solute. Inadequate liquid feeding at the last stage of solidification results the formation of cavities can be also found in Fig. 2.11(b). The breaking point located between the primary dendrites at the fracture surface was also observed as shown in Fig 2.11(c), those tiny spikes indicate that when the dendritic bridges are subject to a tensile deformation, they will be elongated prior to the failure.

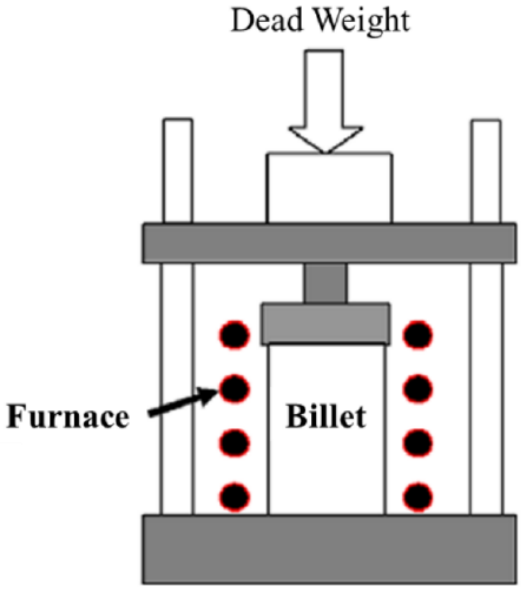

Figure 2.10: Schematic diagram of a compression test apparatus [15].

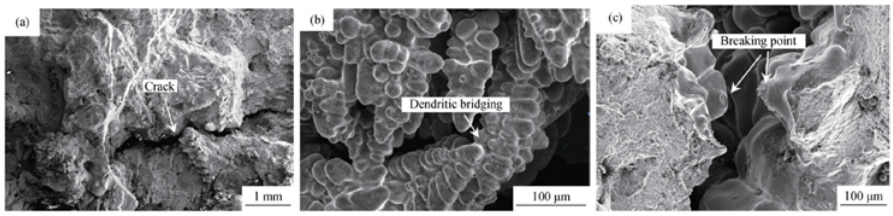

Figure 2.11: Fractographs of steel samples produced with final electromagnetic stirring: (a) cracked region, (b) dendritic region and (c) breaking point of the dendrite [16].

The fractography is also able to capture phenomena such as liquid film, precipitates and inclusions [17]. Fig. 2.12 shows the dendritic structure at 1300 °C of a dual-phase advanced high strength steel. The presence of liquid, shown in Fig. 2.12, leads to an onset of failure that intensifies the tendency to crack due to embrittlement during the tensile test [17]. The author also observed that S-rich precipitates embedded in the fracture surface weaken the shear strength of the material and the round-shape inclusions located at the triple junctions acted as initiation sites for the crack formation.

In-situ observation: in-situ observation of hot tearing performed on transparent organic systems allows researchers to observe the hot tearing formation with the help of optical microscope. Farup et al. [18] conducted an in-situ

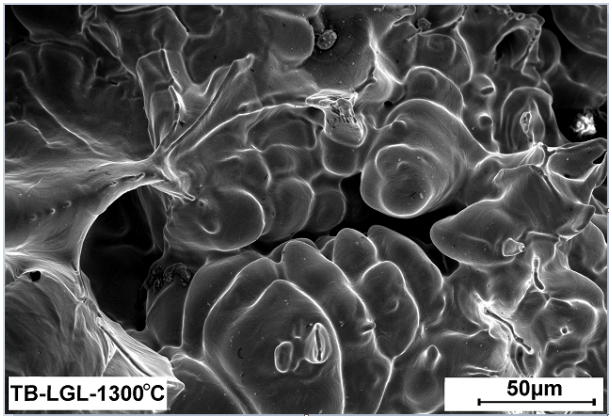

Figure 2.12: Fractograph of a steel sample with a partially melt region [17].

observation on SCN and acetone system during its solidification. This material shares similar characteristics compared with metallic alloys such as body-centered cubic (BCC) lattice and low entropy of fusion as well as its steady state creep behavior near the solidus temperature [102, 103]. The columnar dendrites growing parallel to the thermal gradient at a low solid fraction are shown in Fig. 2.13 on the left. A schematic of the microstructure along with the process is shown on the right. The number of the grains is clearly identified by the labels. After the thermal equilibrium was well established, a pull stick was used to deform the semisolid perpendicularly to the columnar growth direction and thus cause the opening of the liquid channel. The fluid flow direction is illustrated by the arrow, and the formation of equiaxed grains and bubbles during the experimental process could also be observed. The results indicate that if the pulling is performed at a low solid fraction, liquid is able to fill the openings between the dendrites and heal the hot tearing that forms under deformation. Despite the fact that in-situ observation on SCN can provide some fundamental knowledge related to the hot tearing formation, the difference between SCN and metallic alloys in terms of mechanical behaviors are significant, and the deformation rate was not accurately controlled while performing these experiments [104].

2.3.2 Modeling of hot tearing in steel

In addition to experimental investigation, commercial and in-house software can also help to provide new perspectives to shed insights on the mechanism of hot tearing and thus improve the quality of casting products. Modeling of hot tearing formation often remains a big challenge for metallurgists due to the staggering complexities associated with physical phenomena which involve stress and embitterment [105]. For the prediction of hot tearing, the

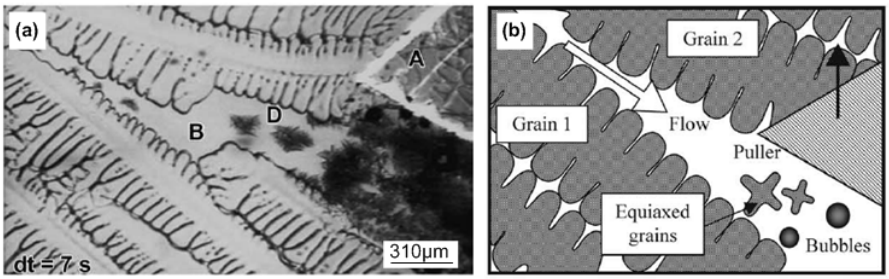

Figure 2.13: A healed hot tear [18].

conventional way is to incorporate a hot tearing criterion into a macroscale thermo-mechanical model. In this section, the key hot tearing criteria for a semisolid varying from microscale to macroscale are reviewed. Additionally, a more sophisticated continuum model and quantitative two-phase mesoscale model used for prediction of hot tearing are also presented.

Macroscopic based criteria

Criteria Based on Thermal Considerations: the thermally-based criteria mainly focus on the freezing range; the larger freezing interval, and the higher hot tearing sensitivity [12]. The simplest hot tearing criterion only depends on the freezing interval based on the thermal analysis, and indicates alloys with wider solidification range are more prone to hot tearing. The criterion proposed by Clyne and Davis [106], labeled CD in this section, defined the hot cracking susceptibility (HCS) as the ratio of time spend in the vulnerable region t_ν with the solid fraction ranges from 0.9 to 0.99 to the total solidification time t_r with the solid fraction ranges from 0.4 to 0.9.

$$\mathrm{HCS_{CD}} = \frac{t_v}{t_r}. \tag{2.3.1}$$

Katgerman [107] expanded this criterion through a combination of thermal theoretical considerations as well as including the effect of solidification shrinkage (following an idea proposed by Feurer [108]),

$$\mathrm{HCS} = \frac{t_{99} - t_{cr}}{t_{cr} - t_{40}}, \tag{2.3.2}$$

where t_{99}, t_{40}, t_{cr} represent the time at solid fractions equal to 0.90, 0.40 and critical value determined by Feurer's criterion. However, the hot tearing sensitivity calculated by these thermal-based criteria are only composition dependent, which is too simple to give accurate predictions given that hot tearing is also related to mechanical deformation of the semi-solid state.

Criteria Based on Solid Mechanics: Campbell [109] also mentioned that

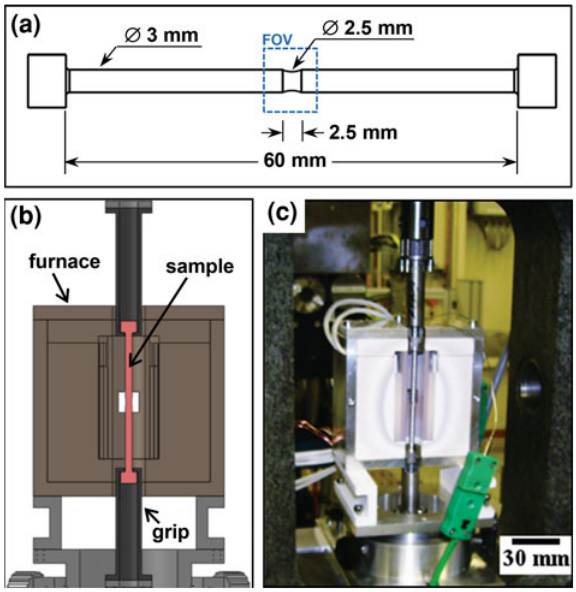

Figure 2.14: (a) Specimen geometry designed for the experiment; (b) a schematic diagram of the furnace and tensile grips; and (c) experimental setup on beamline I12 at Diamond Light Source [19].

the stress development is a major factor for hot tearing since the forces during solidification are much greater as compared to the failure stress of a semi-solid network. However, it is now generally agreed that strain accumulation within the semi-solid material is the major factor contributing to hot tearing. As early as the 1950s, Pellini [110] proposed a critical strain criterion for hot tearing formation in steel alloys. Other well-known strain-based criteria include ones by Prokhorov [111], Novikov [112] and Magnin et al. [113], who all compared the experimentally-obtained fracture strain with thermal contraction or plastic strain, each proposing slightly different equations. Similarly, building on the criterion of Prokhorov, Yamanaka et al. [114] developed a criterion for steels by comparing the obtained accumulated strain over a range of temperatures, termed the brittleness temperature region ΔT_B, against a critical strain limit. Later, Won et al. [13] extended this criterion to a new one named WYSO considering both the strain rate $\dot{\varepsilon}$ and the brittle temperature range. The critical strain ε_c within the brittle temperature range can be expressed as follows,

$$\varepsilon_c = \frac{\varphi}{\dot{\varepsilon}^m \Delta T_B^{n^*}}, \tag{2.3.3}$$

where φ is the constant, m and n^* are the strain rate sensitivity and brittle temperature range exponent. Specifically, the critical strain within the brittle

temperature range was proposed by fitting to Gleeble test results on different steel grades; this indicated that critical strains in the brittle temperature range will decrease with the increasing strain rate and the broadening of the brittle temperature interval. It was suggested that this behavior occurs since larger strain rates cause inadequate time for the liquid to compensate the deformation. However, the critical strain dependents on feeding as well as strain rate, and can't be used alone.

Criteria Based on Solid and Fluid Mechanics: from the mesoscopic viewpoint, liquid flow is another important factor causing hot tearing. The criteria derived by Feurer [108] and Rappaz, Drezet and Gremaud [20] (labeled RDG) are based on a physical description of hot tearing mechanism by considering liquid feeding between the intergranular spaces to counteract mechanical deformations of a semisolid. Feurer's criterion [108] compares the volumetric feeding rate and the solidification shrinkage rate occurring at high solid fractions, and considers that hot tearing will occur once there is inadequate feeding through the intergranular network to counteract shrinkage. However, this criterion does not take into account the mechanical deformations that also occur. Compared with Feurer's model, the RDG model considers a complete physical description of a semisolid, taking into account solidification shrinkage, mechanical deformations, fluid flow, and the permeability of the mushy zone to predict hot tear occurrence.

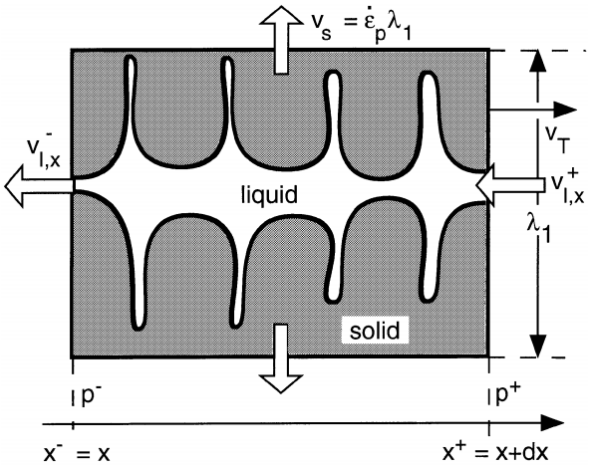

Figure 2.15: A schematic of liquid feeding to compensate shrinkage and uniaxial deformation within a small volume element [20].

In RDG model, the growth direction of columnar grains is assumed to be parallel to the thermal gradient with a tensile deformation perpendicular to the growth direction as shown in Fig. 2.15. Liquid feeding along the direction opposite to the columnar growth is sucked in to compensate for shrinkage

as well as deformation. A mass balance was performed on a small volume element in the mushy zone as shown in Fig. 2.15. The integration over this small volume element finally gives the pressure drop between the tips and roots of the dendrites,

$$\Delta p_{l,\max} = \Delta p_{l,\max}^{\varepsilon_s} + \Delta p_{l,\max}^{\beta}, \tag{2.3.4}$$

where $\Delta p_{l,\max}^{\varepsilon_s}$ and $\Delta p_{l,\max}^{\beta}$ represent the pressure drop associated with deformation and shrinkage, respectively,

$$\Delta p_{l,\max}^{\varepsilon_s} = \frac{5{S_s}^2 (1+\beta)\,\mu_l}{G} \int_{g_l}^{1} \frac{\dot{E}\,(g_l)\,(1-g_l)^2}{{g_l}^3} \frac{dT}{dg_l} dg_l, \tag{2.3.5}$$

$$\Delta p_{l,\max}^{\beta_s} = \frac{5{S_s}^2 v_T \beta_s \mu_l}{G} \int_{g_l}^{1} \frac{(1-g_l)^2}{{g_l}^2} \frac{dT}{dg_l} dg_l, \tag{2.3.6}$$

where the S_s represents the solid/liquid interfacial area concentration, G is the thermal gradient, v_T represents the velocity of the solidification front, μ_l is the dynamic viscosity of the liquid phase, and β_s is the solidification shrinkage, g_l is the liquid fraction and $\dot{E}$ is the cumulative average deformation over the depth of the mushy zone based on the strain rate $\dot{\varepsilon}$, defined as,

$$\dot{E} = \int_{0}^{x} g_s \dot{\varepsilon} dx. \tag{2.3.7}$$

The RDG model assumes that once the liquid pressure falls below the cavitation pressure, a void may form and give rise to the initiation of hot tearing.

All of the above criteria predict the susceptibility of alloys to hot tears. Interestingly, while the RDG criterion is considered best for Al alloys, the Won criterion [13] is considered best for steels [96]. However, neither criteria predict the strain distribution at the semi-solid grain boundaries. The localization of strains is likely to identify where hot tears initiate. Also, the bridging or coalescence phenomena between grains occurring at high solid fraction and delaying final solidification is not considered; including this phenomenon could help to determine if stress transfer occurs between the grains. Based on these ideas, it is clear that hot tearing cannot be simply characterized using an average value across a semi-solid region.

Continuum simulation of hot tears

Average approaches have been proved to be useful methods for the prediction of the hot cracking tendency of alloys in solidification processes such as continuous casting and welding [115, 21]. These methods specifically consider the general formalism of the two-phase nature of a mushy zone, and the microscopic quantities are averaged over a RVE where the mass and momentum equations are solved. The average mass conservation is given by,

$$\frac{\partial}{\partial t}\left(g_s\rho_s + g_l\rho_l\right) + \nabla\cdot\left(g_s\rho_s\vec{v}_s + g_l\rho_l\vec{v}_l\right) = 0, \tag{2.3.8}$$

where g, ρ, $\vec{v}$ represent the volume fraction, density and velocity, and the subscripts s and l indicate the solid and liquid phase, respectively. The superficial velocity of liquid could be approximated by the Darcy's law,

$$g_l\left(\vec{v}_l - \vec{v}_s\right) = -\frac{\kappa}{\mu}\left(\nabla p_l - \rho_l\vec{g}\right), \tag{2.3.9}$$

where κ is the permeability of the mushy zone, and p_l represents the liquid pressure, $\vec{g}$ is the gravity. Substituting Eq. 2.3.9 into Eq. 2.3.8, the average mass conservation equation is expressed as,

$$\frac{\partial\rho}{\partial t} + \nabla\cdot\left(\rho\vec{v}_s\right) + \nabla\cdot\left(\rho_l\frac{-\kappa}{\mu}\left(\nabla p_l - \rho_l\vec{g}\right)\right) = 0, \tag{2.3.10}$$

where $\rho = g_s\rho_s + g_l\rho_l$ is the average density. Assuming quasi-steady state, and the shear stress in the liquid phase is negligible, the momentum equation is reduced to,

$$\nabla\cdot\sigma_e + \rho\vec{g} = \nabla p_l, \tag{2.3.11}$$

where effective stress is defined as $\sigma_e = \sigma + p_l I$, linking the total stress σ with the hydrostatic pressure. I is the unit tensor. Due to the large thermal stress, the contribution of the liquid pressure to the effective stress is further assumed to be negligible, then the two-phase equation ends up,

$$\nabla\cdot\sigma + \rho\vec{g} = 0. \tag{2.3.12}$$

By applying an appropriate constitutive law to link stress and strain (or displacement of solid phase), then Eq. 2.3.12 can be solved for the solid deformation with imposed boundary conditions. The deformation rate of solid grains ($\vec{v}_s$) is used as an input parameter for the pressure calculation given a known permeability at a specific solid fraction. The model's prediction was compared with the experimental results in terms of force and displacement curve as shown in Fig. 2.16. A very good agreement is achieved up to the fracture point for all the four temperatures.

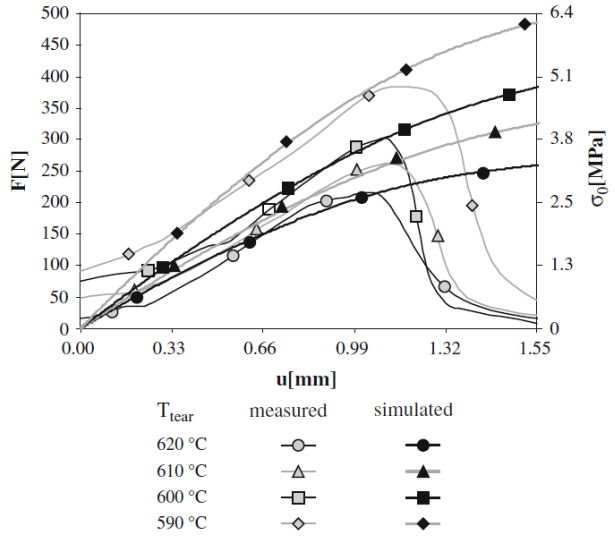

Figure 2.16: Comparison between tensile experimental results of an Al-1wt.% Cu alloy and simulation results at different experimental temperatures. The nominal stress shown on the right is calculated at the neck zone [21].

In this model, despite the fact that the interactions between the solid phase and liquid phase within the mushy zone are considered, it still fails to capture the possible location of hot tearing initiation and its appearance. To predict hot tearing, the microstructure, localization of liquid feeding and strain distribution have to be incorporated within the two-phase model.

Mesoscale simulation of hot tearing

As shown in the hot tearing criteria that have been previously developed, hot tearing is a multi-scale and multi-physics problem requiring an understanding of fluid flow and microstructure at the microscale and stress develop at the scale of the component. In this study, the term mesoscale modelling is defined a simulation technique to predict casting defect. It bridges between the microscale and macroscale. This technique allows for the consideration of interactions between solid and liquid phases and concomitant phenomena simultaneously including microstructure evolution at microscale and transport phenomena at macroscale. Over the past 10 years, the development of a mesoscale and multi-physics model of hot tearing has made it possible to predict the initiation and propagation of hot tearing during solidification in a representative volume element within a mushy zone. In 2004, Mathier et al. [116] first used the 2D Voronoi diagram to approximate the morphology of the semi-solid Al-Cu grains having globular-equiaxed microstructure, and developed a description of grain coalescence at the end of the solidification.

Then, based on this 2D semi-solid microstructural framework, the solidification, liquid feeding and mechanical behavior of Al-Cu alloys in the semi-solid state were investigated by Vernède et al. [64, 117, 118]. Later, this model was extended from 2D to 3D by Phillion et al. [119], and then be improved by Sistaninia et al. [120, 121, 1] by coupling four modules, solidification, flow, deformation and failure, into a complete multi-physics simulation of solidification.

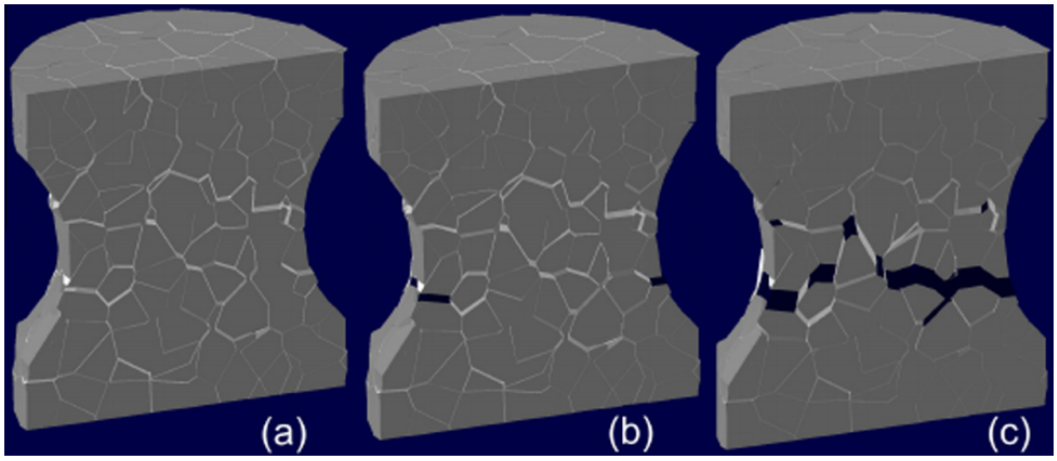

Figure 2.17: Defect evolution of the semi-solid Al-2wt.%Cu specimen under tensile deformation rate at 10^{-4} s^{-1} at (a) 405 s, (b) 729 s and (c) 1215 s [22].

The predictions obtained in Fig. 2.17 consider the deformation of grains, solidification shrinkage, liquid feeding within these liquid channels along with the coalescence between the solid grains. The model is able to reproduce a defect evolution under a tensile deformation at different time qualitatively. The liquid localization was successfully captured under the tensile deformation as shown in Fig. 2.17(a), followed by the void formation as shown in Fig. 2.17(b). The failure of the semi-solid domain was also reproduced and presented in Fig. 2.17(c). This model allows for a direct prediction of hot tearing formation in equiaxed-globular Al alloys for the first time. The results were also validated against X-Ray tomography images [22].

This model also achieves a successful quantitative comparison with experimental measurements. Fig. 2.18 indicates that the stress predicted by the model reproduces the main features of the experimental measurements conducted on a semi-solid Al-Cu alloy under different strain rates. The stress initially increases with the increase of the displacement followed by a decrease due to the presence of the failure. The results also indicate that the stress of the semisolid increases due to the increase of the strain rate.

Recently, Rajani et al. [2, 122, 123, 23] successfully applied this modeling framework to fusion welding process. Their results, shown in Fig. 2.19, enabled

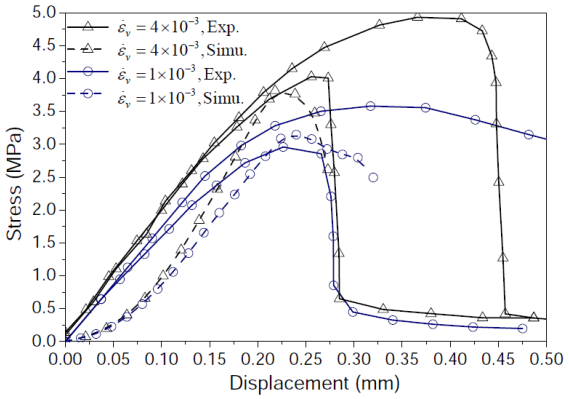

Figure 2.18: Comparison between simulation results (dashed lines) with experimental measurement (solid lines) on a semi-solid Al-2wt.% Cu at a solid fraction of $g_s = 0.98$ at two strain rates [22].

the investigation of external mechanical restraints on deformations within a mushy zone, which was then used to judge the possible locations where the hot tearing might occur.

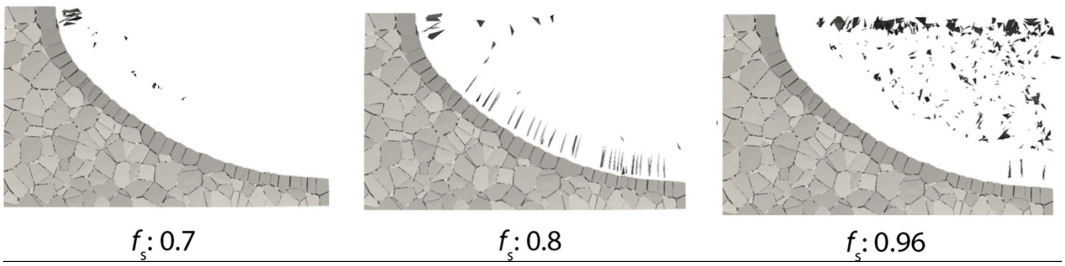

Figure 2.19: Modelling of crack during fusion welding based on Kou's cracking criterion at three different solid fractions of 0.7, 0.8 and 0.96, respectively [23].

The mesoscale and multi-physics model has been proved to be able to reproduce most of the features associated with the hot tearing formation while considering various physical phenomena [12]. In addition to the scientific advantages of this modeling approach for predicting hot tearing, mesoscale models are highly efficient, enabling multi-physics simulation of hot tearing in only a few hours. The drawback of this approach is that the microstructure must be known prior to the simulation, whereas competing methods like phase filed and cellular automaton (CA) can directly predict the solidification structure.

2.3.3 Gaps in previous mesoscale models

The recently-developed multi-scale and multi-physics models of solidification have achieved great success in quantifying hot tearing. However, these models have been developed to calculate the solidification behavior of equiaxed grains with globular structure. They do not allow for reproducing the combined solidification, fluid flow and deformation occurring during continuous casting of steel as significant differences are found between Al alloys and steels. A systematic investigation is needed to shed light on the multi-physics nature of casting defects in steel as the microstructure of continuously-cast steel consists of equiaxed grains with dendritic structure rather than globular structure. For many steel grades, especially advanced high strength steels, the peritectic reaction taking place in the last stage solidification plays a key role in hot tearing susceptibility due the additional density change between δ-Fe and γ-Fe. Additionally, in globular microstructure, liquid feeding to compensate for solidification shrinkage and mechanical deformations occurs around the grains, whereas in dendritic structures the liquid flows both around and through the dendritic network. The temperature profile during continuous casting of steel is complex, because of complex cooling conditions especially in the secondary cooling zones. The semi-solid geometry resulting from the temperature profile is critical for fluid flow behavior which in turn influences the hot tearing sensitivity. Finally, the coalescence undercooling for bridging between the grains is strongly influenced by the grain boundary energy which is a function of grain orientations and the vector perpendicular to the grain boundary plane and was not covered in the prior models.

Chapter 3

Scope and Objectives

The adoption of AHSSs in automotive vehicles keeps increasing due to their outstanding combination of mechanical performance and weight reduction. However, they often exhibit cracking and macrosegregation problems during the continuous casting process, which have plagued the continuous casting process since its inception. Continuously-cast steel products with severe defects usually contain reduced mechanical properties and must be down-graded.

To solve these problems, in this PhD project, it is proposed to develop a mesoscale and multi-physics model of steel solidification, focusing on AHSSs in order to improve the castability of these important steel alloys, and taking into considerations of the modeling gaps identified in Section 2.2.3 and 2.3.3. To provide the relevant evolution in temperature during continuous casting of steel, the model will be coupled with macro-scale process simulations. The combination of these two approaches will enable predictions of centreline segregation within a casting slab as a function of casting parameters including alloy compositions and deformation rates.

The newly-developed multi-physics model is built on the previous models developed over the past 10 years [64, 117, 118, 120, 121, 1, 2, 122, 123, 23], but will include additional physical phenomena necessary to simulate the microstructure evolution, stress/strain and fluid flow along with macrosegregation during continuous casting of the steel. Different from the previous applications that focused on globular microstructure, dendritic microstructure is more sensitive to hot tearing as the liquid will not only remain between the grains but also within the inter-dendritic region; these liquid channels have little capacity to withstand semi-solid deformation. To accurately predict these defects, several models need to be developed and coupled together to simulate the behavior of a large number of grains with different orientations during solidification of steel. Each model has its specific functions during solidification. This research pursues the main following objectives:

(i) A new 3D solidification model will be developed to simulate the solidification of steel at the mesoscale. The primary solidification and peritectic transformation within each grain will be taken into account. Also, phase evolution within a semi-solid domain with either dendritic or globular microstructure can be reproduced. The new solidification model should be able to consider coalescence phenomenon between grains at the end of solidification.

(ii) The development of a 3D mesoscale model for the prediction of fluid flow within liquid channels in a semisolid with varying equiaxed microstructure, from dendritic to globular. The model should be able to quantitatively predict the fluid flow behavior induced by the solidification shrinkage and deformation at a mesoscale.

(iii) The development of a 3D mesoscale solute transport model. This approach should enable new insights into the fundamental mechanisms of centreline segregation within a semisolid containing loosed packed equiaxed grains, whereby the flow of enriched intra-dendritic liquid is induced by the solidification shrinkage and deformation.

(iv) Experimental measurements of large-scale solute maps within steel samples taken from casting slabs will be conducted via X-ray fluorescence for the validation of centreline segregation predicted by the mesoscale solute transport model.

Chapter 4

Methods

In this chapter, a 3D mesoscale solidification model of solidifying steel alloys during continuous casting is proposed to investigate late-stage solidification phenomena that lead to hot tearing and segregation. This mesoscale model consists of 4 sub-models: i) microstructure generation model, ii) dendritic solidification model, iii) dendritic fluid flow model, iv) semisolid deformation model. The prediction of defects requires additional physics, leading to the development of two coupled models: v) semisolid cracking model and vi) mesoscale solute transport model based on the 4 sub-models. A brief introduction of each sub-model and coupled model is presented below.

i) A microstructure generation model predicts the fully solidified microstructure of equiaxed grains using a Voronoi tessellation. In this model, a discretized mesh of equiaxed grain is presented along with a typical example of the microstructure.

ii) A 3D dendritic solidification model is developed for the prediction of the semisolid geometry at the mesoscale. This new model allows for the investigation of microstructure morphology transition from individual dendritic grains to a percolated solid network, while permitting a detailed analysis of the evolution in δ fraction, dendrite envelope fraction (containing both solid and intra-dendritic liquid phase), and γ fraction (in peritectic grades) at the scale of a single grain. A model [24] that takes into account the five physical parameters of misorientation is used to quantify the grain boundary energies that control the disappearance of the thin liquid films between grains.

iii) A dendritic fluid flow model is proposed to simulate fluid flow during the solidification within a mushy zone containing both intra-dendritic and extra-dendritic flow and taking into account shrinkage caused by the peritectic transformation and deformation. The mesoscale semi-solid domain is created using the 3D dendritic solidification model in ii).

iv) A semisolid deformation model initially developed by Sistaninia [120] is extended to predict the mechanical behavior of a semisolid containing both

solid and liquid phases at a given solid fraction. The solid phase is modeled by using a constitutive law and the liquid phase is approximated by a special connector. The semisolid deformation analysis is performed using the commercial code Abaqus and different kinds of elements used in this simulation are also presented.

v) The semisolid cracking model simulates the hot tearing initiation and propagation within a semisolid consists of equiaxed grain structures. The semisolid deformation of solid grains is performed using the semisolid deformation model in iv) while the pressure within the liquid channels is predicted by a modified dendritic fluid flow model in iii). A crack initiation criterion is incorporated within the semisolid cracking model for identifying the initiation location of hot tearing.

vi) The mesoscale solute transport model, building on the dendritic solidification model in ii) and fluid flow model in iii), is developed for the prediction of segregation at a mesoscale. This model directly combines solute transport at the scale of the casting with solute partitioning at the scale of the grains. This approach enables new insight into the fundamental mechanisms resulting in centreline segregation within a semisolid containing loose-packed equiaxed grains. The flow of enriched intra-dendritic liquid is induced by the solidification shrinkage and mechanical deformation.

The detailed descriptions of these subdomains and coupled models are presented in Section 4.1 and 4.2, respectively. All sub-models or the coupled models need to be validated with either empirical equations or experimental data. The coupled semisolid cracking model is validated against the semisolid tensile experimental measurements by Seol et al. [27] while the coupled mesoscale solute transport model is validated against the solute map measured via MXRF quantitatively. In Section 4.3, the semisolid tensile test experiment used to measure the tensile strength of semisolids and MXRF used to measure the solute map within a steel sample cast at a specific condition are presented.

4.1 Fundamental models

4.1.1 Microstructure generation model

The microstructure of semi-solid steel is assumed to consist of a large number of equiaxed dendritic grains having different orientations, and a continuous liquid layer coexisting around the solid structure. To approximate the 3-D microstructure in the semisolid, an unstructured mesh is created based on a Voronoi tessellation [124] of the grain nuclei within a representative volume element, Fig. 4.1(a), whereby each polygon, Fig. 4.1(b) represents one grain. The grains are then subdivided into smaller polyhedral sub-elements, Fig. 4.1(c), which are further divided into many tetrahedral elements with the

nucleation site as the summit and the surface of the polyhedron as the base, shown in Fig. 4.1(d-1). The grain density within the domain is acquired from metallographic analysis and used as a model input parameter. Note that the microstructure of steel containing columnar gains can also be generated using a modified Voronoi tessellation of random points, following [2]. Specifically, an in-house C++ code was developed to create a local Voronoi diagram representing equiaxed grains with different orientations firstly, similar as Fig. 4.1(a). Then a procedure is used to modify the morphology, the seeds are moved to one edge of RVE to create elongated polyhedral elements approximating columnar microstructure. Since this thesis only focuses on a semisolid containing equiaxed grains, and readers could refer to Ref. [125] for a detail explanation of microstructure generation of columnar grains in steel alloys.

With the fully solidified microstructure generated by Voronoi tessellation, solidification is simulated independently for each tetrahedral element using a 1-D volume average method in spherical coordinates as will be described in Section 4.1.2. A uniform temperature assumption is applied throughout the domain, nucleation of all grains is assumed to occur simultaneously, and the boundaries of each fully solidified grain correspond to the shape of a Voronoi polygon. To simulate dendritic solidification, the position of the dendrite envelope is tracked, moving from the initial nucleation site at t=0 to the boundary of the Voronoi tessellation. Then, each tetrahedral element is partitioned into different phases depending on the fraction of each phase. As the dendritic morphology indicated in Fig. 4.1(d-1) cannot be visualized by an unstructured mesh, the model shows the equivalent phase fraction in a geometric sense, Fig. 4.1(d-2). The bulk solid fraction within the domain is then estimated by summing all of the solid within each tetrahedral element. An example simulation domain, 125 mm^3 and created using the developed C++ code, is shown in Fig. 4.1(e). In this domain, the solid fraction is 0.81 and the average size of the equiaxed δ grains is $\sim$ 500 µm. Note that the liquid phase represents the sum of both intra-dendritic and extra-dendritic liquid phase for dendritic structure shown in Fig. 4.1(e); the amount of remaining liquid within each grain is represented by the channel thickness.

4.1.2 Dendritic solidification model

Solidification of the dendritic structure is simulated using a volume average method for multiphase binary systems [126, 127, 128, 129]. In the volume average approach, the evolution of the solid/liquid interface cannot be explicitly tracked; instead the phase fraction could be obtained without requiring high computational cost. Occurrence of the peritectic transformation is also included, for relevant chemistries. Thus, the phase fraction of interest such

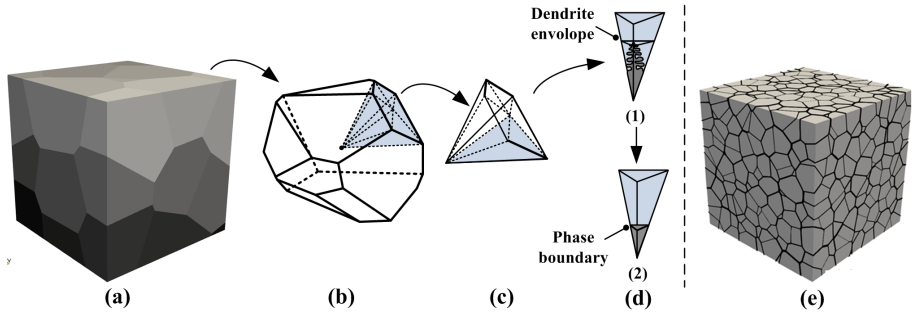

Figure 4.1: Various geometries of the 3D meso-scale model: (a) 3D Voronoi tessellation consisting of 27 grains each colored by a different grayscale value; (b) a single Voronoi grain; (c) polyhedral element, (d) tetrahedral element, (e) semi-solid domain with 1000 grains at the solid fraction 0.81. In (e) the liquid is colored black, while the delta ferrite grains are colored in gray. Note that the amount of remaining liquid within each grain is represented by the channel thickness.

as primary phase g_δ, austenite g_γ and liquid phase g_l can be predicted incrementally. Note that the liquid phase fraction can be further distinguished by total intra-dendritic g_{l_intra} and extra-dendritic liquid g_{l_extra}. The dendrite envelope fraction, g_g, represents the total amount of solid phase as well as the intra-dendritic liquid, i.e. g_g=g_δ+g_γ+g_{l_intra}. The main idea of the volume average approach is that the δ and/or γ phases nucleate from the center of the grain in an undercooled liquid (l) and grow in radial direction until the total element length, R, is reached, as shown in either Fig. 4.2(a) or (b). Different zones are used to track the formation and disappearance of various phases; each phase can coexist in multiple zones. As stated previously, temperature is assumed to be uniform and continuously cooling at a given rate. In primary solidification, the δ dendrite tip position ($R^{(1)}$) separates zones (0) and (1), as shown in Fig. 4.2(a1). Zone (0) contains only extra-dendritic liquid ($g_l^{(0)}$) whereas zone (1) contains intra-dendritic liquid ($g_l^{(1)}$) and δ phase ($g_\delta^{(1)}$). Zone (2), a combination of δ phase ($g_\delta^{(2)}$), γ phase ($g_\gamma^{(2)}$) and intra-dendritic liquid ($g_l^{(2)}$), forms when the γ phase nucleates, eliminating zone (1) as shown in Fig. 4.2(b1). It is assumed that the peritectic reaction occurs instantaneously, and thus the position of the γ phase tip ($R^{(2)}$) is equal to the position of the primary δ dendrite tip ($R^{(1)}$). The dendrite tip position also denotes the edge of the dendrite envelope. The radial growth rate of the dendrite tip is predicted via a kinetic model [130]. The dendrite envelope fraction is calculated as g_g= 1−$g_{\mathrm{l\_extra}}$, where $\mathrm{g}_{l\_\mathrm{extra}} = g_l^{(0)}$. Alternatively, it could be calculated as $\mathrm{g}_g = \sum_{i=1}^{2} g_\delta^{(i)} + \sum_{i=1}^{2} g_\gamma^{(i)} + \sum_{i=1}^{2} g_l^{(i)}$. Note that the superscript indicates the zone that the phase exists. The sum of the volume fractions (g) of each

phase within a grain is equal to unity, such that $g_\delta + g_\gamma + g_l = 1$. Due to the different concentrations of the δ, γ and l phases, a solute mass balance is considered individually for each phase in each zone, and the solute exchange at the zone boundaries is also included. Note that equal and constant densities are assumed for all phases. For more details on the volume average approach to model dendritic growth, please refer to [77].

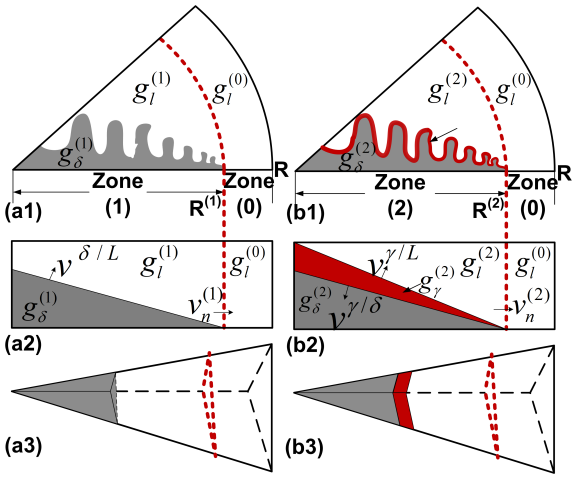

Figure 4.2: Schematic diagram showing (a) primary solidification and (b) primary solidification plus peritectic transformation. The images (1), (2), and (3) show the actual dendritic structure, equivalent structure for the volume average model, and the geometric structure for the meso-scale model. The grey, red, and white regions indicate the δ, γ and l regions. The dotted red line denotes the dendrite envelope.

Inside each zone, α and β represent individual arbitrary phases. The average mass conservation of an individual phase and mass exchange over the phase interface are given by

$$\frac{\partial g^\alpha}{\partial t} = \sum\nolimits_{\alpha/\beta} (S^{\alpha/\beta} v^{\alpha/\beta}), \tag{4.1.1}$$

$$v^{\alpha/\beta} + v^{\beta/\alpha} = 0, \tag{4.1.2}$$

where g^α is the volume fraction of an individual phase within each zone, $v^{\alpha/\beta}$ is the normal velocity of the phase interface on the α side shown in Fig. 4.2(a2) as $v^{\delta/l}$, and $S^{\alpha/\beta}$ is the interfacial area concentration, defined as $A^{\alpha/\beta}/V$, where $A^{\alpha/\beta}$ is the interfacial area between the α and β phases and V represents the total volume of the domain. Note that phases co-existing in multiple zones are considered to be different phases.

For an individual phase, solute conservation is given as

$$g^{\alpha}\frac{\partial\langle c^{\alpha}\rangle^{\alpha}}{\partial t}=\sum\nolimits_{\beta(\beta\neq\alpha)}S^{\alpha/\beta}\left(c^{\alpha/\beta}-\langle c^{\alpha}\rangle^{\alpha}\right)\left(v^{\alpha/\beta}+\frac{D^{\alpha}}{\ell^{\alpha/\beta}}\right), \tag{4.1.3}$$

$$\left(c^{\alpha/\beta}-c^{\beta/\alpha}\right)v^{\alpha/\beta}+\frac{D^{\alpha}}{\ell^{\alpha/\beta}}\left(c^{\alpha/\beta}-\langle c^{\alpha}\rangle^{\alpha}\right)+\frac{D^{\beta}}{\ell^{\beta/\alpha}}\left(c^{\alpha/\beta}-\left\langle c^{\beta}\right\rangle^{\beta}\right)=0, \tag{4.1.4}$$

where $c^{\alpha/\beta}$ represents the solute concentration of the phase interface on the α side. The concentrations at the δ/l or γ/l interface are given by the equilibrium binary phase diagram, the two symbols $\langle c^{\alpha}\rangle^{\alpha}$ and $\left\langle c^{\beta}\right\rangle^{\beta}$ represent the average solute concentration in α and β, $\ell^{\alpha/\beta}$ represents the diffusion length in the α phase, and D^{α} and D^{β} are the solute diffusion coefficient in α and β. The expressions for the interfacial area concentration $S^{\alpha/\beta}$ and diffusion length $\ell^{\alpha/\beta}$ are presented in detail elsewhere [126, 129].

The boundary velocity for zone (1) or zone (2) is equal to the dendrite tip velocity of δ or γ growing into the undercooled liquid. This tip velocity is calculated using the KGT model [130],

$$v_{n}^{(1)}=-\frac{D^{l}m^{\delta/l}\left(c^{l/\delta}-c^{\delta/l}\right)}{\pi^{2}\Gamma^{\delta/l}}\left[Iv^{-1}\left(\Omega^{\delta/l}\right)\right]^{2}, \tag{4.1.5}$$

where $v_{n}^{(1)}$ is the boundary velocity of zone (1), $m^{\delta/l}$ is the liquidus slope of δ phase, $\Gamma^{\delta/l}$ is the Gibbs-Thomson coefficient, and Iv^{-1} and $\Omega^{\delta/l}$ represent the inverse of the Ivantsov function, and solute supersaturation, respectively [77],

$$Iv^{-1}\left(\Omega^{\delta/l}\right)=0.4567\cdot\left(\frac{\Omega^{\delta/l}}{1-\Omega^{\delta/l}}\right)^{1.195}, \tag{4.1.6}$$

$$\Omega^{\delta/l}=\left[c^{l/\delta}-\left\langle c^{l^{(0)}}\right\rangle^{l^{(0)}}\right]/\left[c^{l/\delta}-c^{\delta/l}\right]. \tag{4.1.7}$$

In Eq. 4.1.5, 4.1.6, and 4.1.7, l and δ represent the arbitrary phases α and β.

The 1-D volume average solidification model is applied to each tetrahedral element, assuming the element height to be the total grain radius, R, and solute exchange between two neighboring elements is neglected. In this fashion, the variation in individual phases along with the evolution of semi-solid morphology can be predicted at the meso-scale. This model is implemented using a purpose-written C++ code that solves Equations 4.1.1-4.1.7 simultaneously for each phase, within each zone, for each grain. The differential equations are discretized using an explicit difference method, with the term on the left-hand

side of the equation being calculated from the values taken from the previous time step. The detailed solution procedure is as follows. First, time is incremented to the next time step. This results in an incremental reduction in temperature and causes the equilibrium concentrations at the interface $c^{\alpha/\beta}$ to be updated based on the phase diagram. Second, $v_n^{(i)}$ is calculated based on Eq. 4.1.5, and the volume fraction of each zone (zone 0, zone 1, zone 2, ...) is updated. Third, $S^{\alpha/\beta}$ and $\ell^{\alpha/\beta}$ are determined, and then $v^{\alpha/\beta}$ is obtained by combining Eq. 4.1.2 and Eq. 4.1.4. Subsequently, the concentration at the zone boundary $c^{\alpha/\beta}$ is calculated via Eq. 4.1.4 for phases that co-exist in two zones. Finally, the volume fraction and average concentration of each phase are determined using Eq. 4.1.5 and Eq. 4.1.3. All of the values for these parameters at the present step are then used as initial conditions for the next time step. Once the volume fraction of each phase has been calculated, the equivalent positions of the various interfaces are determined, in a geometric sense, as shown in Fig. 4.2(a2) and Fig. 4.2(b2) to show the structure within the framework of a Voronoi tessellation.

An example of the model results for a single grain is shown in Fig. 4.3, which predicts the solidification behavior (evolution in the dendrite envelope fraction g_g and the delta-ferrite fraction g_δ as a function of time) of a non-peritectic alloy with 0.07wt.% carbon being cooled at 0.1°C/s and 50°C/s. The results indicate that at 0.1°C/s, a low cooling rate, the kinetics of the dendrite envelope evolution is rather slow. This can be seen by the superposition of the solid fraction and grain fraction curves in Fig. 4.3(a). At the initial stage of solidification, g_g increases faster than the solid fraction and a small dendritic structure forms. However, as solidification continues, the solid fraction becomes equal to the dendrite envelope fraction resulting in a final microstructure that is globular. On the other hand, when a cooling rate of 50°C/s is applied to the model, the dendrite envelope grows quite fast until it reaches the maximum grain radius whereas the solid fraction evolves at a much slower rate. The gap between the two curves leads to the formation of a dendritic structure. Thus, during continuous casting, while the dendrite envelopes from neighboring grains may be about to touch, a great amount of liquid remains in the intra-dendritic regions. This is an indication that although the extra-dendritic liquid films may be thin, the remaining intra-dendritic liquid might play an important role in hot tearing susceptibility. Through this small example it is shown that the use of a volume average method as part of the 3-D mesoscale solidification model is able to predict dendritic structure near the meniscus where the cooling rates are high but will still predict globular grains near the centre of the slab where cooling rates are low. The formation of the columnar zone is ignored in this study because of the focus on blown grains; it was covered in one of our prior publications [125].

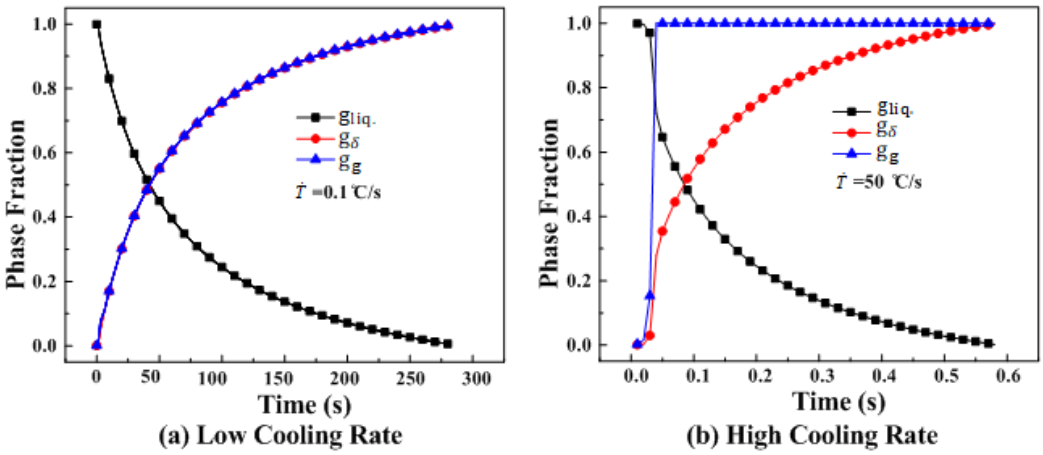

Figure 4.3: Evolution of liquid, solid-δ and dendrite envelope fraction of a single grain for a Fe-0.07 wt.% C alloy cooling at (a) 0.1°C/s and (b) 50°C/s. A grain radius of 100 µm and a secondary arm spacing of 20 µm are assumed in both cases.

Coalescence criterion

As mentioned in Sec. 2.1.2, a coalescence undercooling is needed for the two grains to impinge. This undercooling cooling is calculated based on grain boundary energy γ_{gb} which depends critically on the misorientation between two grains. For dendrite arms belonging to the same grain, no misorientation exists and γ_{gb}=0. In this case, a solid bridge would immediately form between these dendrite arms when they are a few nanometers away as they attract each other. For dendrite arms belonging to different grains, γ_{gb} is influenced by five parameters; three for misorientation between the crystal lattice of the two grains and two for the orientation of the grain boundary plane itself. The mesoscale solidification model of steel includes the requirement to overcome the thermodynamic barrier to coalescence between neighboring grains in order to predict the gradual formation of grain clusters that are able to withstand deformations applied to the mushy zone. Specifically, Eq. 2.1.3 is applied to determine the required undercooling for bridging between two dendritic-equiaxed grains to predict the transient from the isolated solid grains to one coherent solid cluster. The prior work of Sistaninia randomly assigned a single orientation value between 0° and 90° to each grain and then calculated γ_{gb} [120, 131, 118, 64, 1, 117] based on a symmetric tilt boundary along [100]. Bulatov et al. recently proposed a model to calculate the grain boundary energy between any two misoriented grains [24] having FCC crystal structure taking into account the five physical parameters of misorientation. In the

present work this new model is used; the three Euler angles defining the orientation of each grain are assigned randomly. The calculated data provided by Bulatov for the Ni system is used to approximate the grain boundary energy of Fe as their properties are quite similar to each other [132]. Because the approach proposed by Bulatov is limited to FCC systems, the coalescence model is only applicable to peritectic grades of steel.

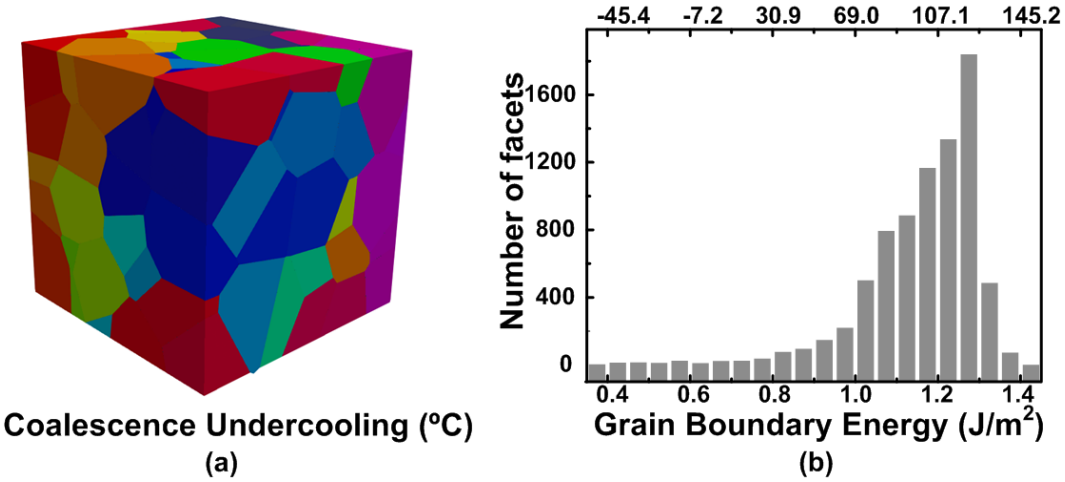

Figure 4.4: (a) Meso-scale simulation domain containing 125 equiaxed grains with different orientations; (b) grain boundary energy and coalescence undercooling distributions used in the multi-physics model for a Fe-0.16wt.% C alloy as proposed by Bulatov et al. [24].

Fig. 4.4(a) shows the output of a simulation, 125 mm^3 in size with an average grain size of 1000 µm for a Fe-0.16wt.%C alloy. The frequency of the calculated γ_{gb} between any two neighboring grains and the corresponding ΔT_b based on the Bulatov's approach is plotted in Fig. 4.4(b). As can be seen, γ_{gb} ranges from 0.37 to 1.40 J/m^2, which results in considerable undercooling required for coalescence, up to 145.2°C. The majority of the grain interfaces require undercooling greater than 100°C below the equilibrium solidus before coalescence occurs. The results also show that the proportion of negative coalescence undercoolings is $\sim 0.9\%$, indicating that only a very small proportion of the grains are attractive to each other and promote the occurrence of solidification-related grain coalescence whereas the remainder are repulsive.

Corner rounding

The semisolid geometry created via the above microstructure generation model and solidification dendritic model is found to have sharp edges. In reality, the sharp edge of a semisolid created by Voronoi tessellation does not exist, and is remelted due to Gibbs-Thomson effect. The morphology predicted by the

Voronoi tessellation with sharp edges overestimates the solid fraction at the coalescence point [133]. The unrealistic shape also fails to predict the liquid pocket formed at the triple junction of the grains. To overcome the drawback of using Voronoi tessellation to generate the microstructure and consider the non-facet and smooth interface, a rounded corner model developed specifically by Vernède et al. [117] and Sistaninia et al. [134] has been implemented in the present model for the readjustment of the liquid film thickness within semi-solid steel.

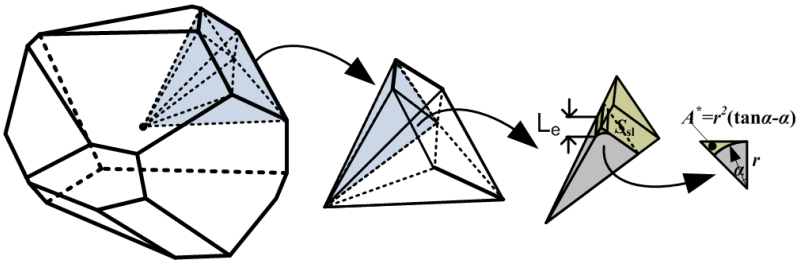

Figure 4.5: Schematic of the smoothing process of grain corner in a 3-D element following Sistaninia [1]. Note that the amount of remaining liquid between grains is highlighted in yellow.

Fig. 4.5 outlines the rounding process of a grain corner along the edge. The approximation of the curvature radius was initially proposed by Vernède and Rappaz [117] for 2D mesh, and was applied to 3D geometry by Sistaninia et al. [1]. In 3D geometries, the rounding is only along the edge not at the vertices as shown in Fig. 4.5.

Assuming that the temperature of a whole element is homogeneous, the solute will flow from enriched areas associated with low curvature to zone with high curvature, similar to the coarsening effect. Based on the fundamental of solute balance, in the other words, the solute flux will flow from the flat solid/liquid interface to the zones near the corner and remelt the high curved edge. The radius of the curvature r near the corner shown in Fig. 4.5 is given by,

$$r = \left[A_c \frac{2}{\tan\alpha - \alpha} \frac{\Gamma_{sl} D_l}{-\dot{T}} \right]^{1/3}, \tag{4.1.8}$$

where A_c represents the dimensionless constant, α indicates half of the supplementary angle of the grain corner angle shown in Fig 4.5. The additional liquid volume added due to the rounding edge is determined via,

$$\vee = L_e r^2 \left(\tan\alpha - \alpha\right), \tag{4.1.9}$$

where L_e is the edge length shown in Fig 4.5.

The modification of a rounding edge results in an increase of the liquid volume. Considering the redistribution of liquid phase due to curvature effect, the solid/liquid interface position needed to be slightly moved forward accounting for the additional liquid volume near the corner given a constant solid fraction. Due to the fact that liquid pockets exist at the triple point between grains, the coalescence will occurs at a lower solid fraction due to the readjustment of the solid/liquid interface position. The critical liquid film thickness for coalescence is determined via,

$$2\widehat{h} = 2h - 2\left[2A_c\frac{\Gamma_{sl}D_l}{-\dot{T}}\right]^{2/3}\frac{\sum_{i=1}^{n} L_e^i[\tan\alpha - \alpha]^{1/3}}{2S_{sl}}, \tag{4.1.10}$$

where i=1, 2,..., n represents the edges of the two neighbor facets, $2S_{sl} = \sum_{i=1}^{n} S_{sl}^{e\,i}$ is the total interfacial area of the two facing grains, and $2h$ represents the liquid channel thickness calculated without considering the rounding edges.

4.1.3 Dendritic fluid flow model

The formation of casting defects, especially hot tearing and segregation, have been shown to be related directly to the flow of liquid through the dendritic network at the microscale [12], due to the concomitant phenomena of solidification induced shrinkage and mushy zone deformation. A semisolid's resistance to liquid flow is known as permeability. This important macroscopic parameter is associated with a pressure drop inside mushy zone, bridges the microscale structure with macroscale fluid flow, and is critical for accurate prediction of defect formation. Measurement of permeability is usually associated with determination of the structure first followed by a prediction of the fluid flow behavior [135]. The challenge when measuring this quantity in metallic systems lies in controlling the semisolid microstructure during the experiment; reliable data for high temperature alloys remains rare [136]. Accurate prediction through numerical simulation is also challenging since permeability is a characteristic that is based on the channel width, surface area and tortuosity of the flow channels [137]. For industrial applications, there is a need for improved understanding of permeability in a wide range of microstructures.

In this section, a 3D dendritic fluid flow model is proposed to simulate fluid flow within a mushy zone containing both intra-dendritic and extra-dendritic flow and taking into account shrinkage caused by the peritectic transformation and deformation. The 3D semisolid structure created by the dendritic solidification model at a given solid fraction for a specified cooling rate and grain size is used as the input geometry for the fluid flow model at the same solid fraction. The two models, solidification and fluid flow, are only one-way coupled.

First, the velocity profile between two facing dendrites is reviewed. Second, the mass balance performed to derive the controlling equation is described. Third, the numerical implementation is covered.

Velocity profile of fluid

The mesh consists of a set of elements, each made up of two facing tetrahedrons as shown in Fig. 4.6, that are ultimately reduced to a set of two 3-node 2D triangular elements. The regions enclosed by the dendrite envelopes of each tetrahedron are treated as a uniform porous medium [78] with an internal liquid fraction given by $g_l' = g_l^{id}/(g_l^{id} + g_\delta + g_\gamma)$. The extra-dendritic regions of each element, having a width equal to the distance between the facing envelopes, are treated as an extra-dendritic fluid channel. Note that the two facing tetrahedrons are identical due to symmetry [121]. Flow can occur simultaneously through both the intra- and extra- dendritic regions as shown schematically in Fig. 4.6 (solid blue line). In the limit of $g_l' = 0$, the model is reduced to the model of flow between two globular grains, equivalent to the model of Sistaninia [121]. In another limit, where the dendrite tips touch and all remaining liquid is intra-dendritic liquid ($g_l^{ed} = 0$, $g_l^{id} = g_l'$), the whole structure behaves as a porous medium with a liquid fraction g_l' and a characteristic length scale given by the secondary dendrite arm spacing. In these two situations, also shown in Fig. 4.6, the corresponding flow is either Poiseuille flow (red dashed line) or Darcy-Brinkman flow (green dashed line).

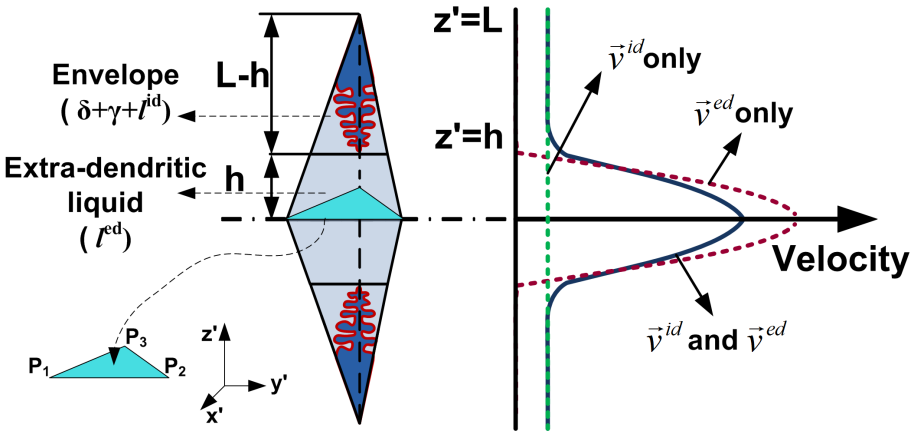

Figure 4.6: Schematic diagram of two facing tetrahedrons, the velocity profile of fluid passing through the inter- and extra- dendritic regions, and the corresponding 3-node 2D triangular element. The velocity profiles for the cases with only intra-dendritic and only extra-dendritic flow are also shown.

The flow in the extra-dendritic region is described as a Poisseuille flow and the flow in the intra-dendritic region is described by the Darcy-Brinkman

equation, using a averaged form of the Navier-Stokes equation. The model assumptions include quasi-steady-state as well as irrotational flow that is parallel to the triangular facet highlighted in blue in Fig. 4.6 where the two tetrahedrons meet. Both gravity and pressure gradients along the length L of the element are neglected. Altogether, this is expressed as,

$$-\nabla p + \mu_l \frac{d^2 \vec{v}^{ed}}{dz'^2} = 0, \tag{4.1.11}$$

$$-g_l' \nabla p + \mu_l \frac{d^2 \vec{v}^{id}}{dz'^2} - \frac{\mu_l g_l'}{\kappa\left(g_l'\right)} \vec{v}^{id} = 0, \tag{4.1.12}$$

where μ_l represents the dynamic viscosity, $\vec{v}^{ed}$ is the fluid velocity in the extra-dendritic region, p is the gauge pressure, $\vec{v}^{id}$ is the intra-dendritic fluid velocity vector and $\kappa\left(g_l'\right)$ is the local permeability within the dendrite envelope. The reader is referred to [138] for detailed information of the averaging concepts along with the process of deriving the average form of the master equation. The Carman-Kozeny equation [89],

$$\kappa(g_l{}') = \frac{\left(g_l{}'\right)^3}{5 S_s^2}, \tag{4.1.13}$$

where S_s represents the interfacial area concentration is simplified as $S_s = \frac{2}{\lambda_2}$ with λ_2 representing the secondary dendrite arm spacing, is used to determine κ as the scale of an individual element.

It is assumed that $\frac{\partial}{\partial z'} \vec{v}^{ed}|_{z'=0} = 0$ and $\vec{v}$ is finite when $z' \to \infty$. At the envelope, the boundary conditions between the porous medium and a fully liquid zone, proposed by Le Bars and Grae Worster [138] is used: $\vec{v}^{ed}|_{z'=h} = \vec{v}^{id}|_{z'=h}$ and $\frac{\partial}{\partial z'} \vec{v}^{id}|_{z'=h} = \frac{\partial}{\partial z'} \vec{v}^{ed}|_{z'=h}$. Eq. 4.1.11 and Eq. 4.1.12 can be solved analytically,

$$\vec{v}^{ed} = \left(\frac{z'^2}{2\mu_l} + C_1 \right) \nabla p, \tag{4.1.14}$$

$$\vec{v}^{id} = \left(C_2 e^{\frac{z'}{\xi}} - C_3 \right) \nabla p. \tag{4.1.15}$$

In Eqs. 4.1.14 and 4.1.15, C_1 and C_2 represent two unknown constants, $C_3 = \frac{g_{l'} \xi^2}{\mu_l}$ and $\xi = \sqrt{\frac{\kappa\left(g_l'\right)}{g_l'}}$. The unknown constants can be further solved with additional constraints at the envelope shown above: all of the fields within the representative volume are continuous, the velocity $\vec{v}$ and the viscous stress at the interface between the intra-dendritic and extra-dendritic regions must be

continuous. Then,

$$C_1 = -\frac{\xi h}{\mu_l} - \frac{g_l' \xi^2}{\mu_l} - \frac{h^2}{2\mu_l}, \text{and,} \tag{4.1.16}$$

$$C_2 = \frac{-\frac{\xi h}{\mu_l}}{e^{-\frac{h}{\xi}}}, \tag{4.1.17}$$

where h is the half width of the extra-dendritic region.

Mass balance

The controlling equation for the fluid flow problem can be derived through integration based on a mass balance over the two facing tetrahedrons shown in Fig. 4.6 assuming liquid incompressibility, *i.e.* $\nabla \cdot \vec{v}_l = 0$. This region includes both flow as a porous medium within the dendrite envelope and free liquid flow in the extra-dendritic region. This mass balance also needs to consider both the solidification shrinkage and deformation as factors that would induce liquid flow. The shrinkage induced by solidification due to the density variations in the solid and liquid phase will induce a normal velocity of liquid flow at the solid/liquid interface [12],

$$\vec{v}_l = -\beta_s v_T, \tag{4.1.18}$$

where v_T is the solid/liquid interface velocity predicted by the 3D meso-scale solidification model at the specific solid fraction being used in the fluid flow simulation, and $\beta_s = (\rho_s/\rho_l - 1)$ is the shrinkage factor with ρ_s and ρ_l representing the temperature-dependent solid and liquid densities. For non-peritectic alloys, $\rho_s = \rho_\delta$. For peritectic alloys ρ_s is given by

$$\rho_s = \frac{\rho_\delta g_\delta + \rho_\gamma g_\gamma}{g_\delta + g_\gamma}, \tag{4.1.19}$$

$$\rho_\delta = 3.07 \times 10^{-1} \left(T_{\delta,start} - T\right) + 7270, \tag{4.1.20}$$

$$\rho_\gamma = 4.8 \times 10^{-1} \left(T_{\gamma,start} - T\right) + 7410, \tag{4.1.21}$$

$$\rho_l = -7.5 \times 10^{-1} \left(T - T_{L,start}\right) + 7020, \tag{4.1.22}$$

where ρ_δ, and ρ_γ represent the densities (kg.m^{-3}) of the δ and γ phases in steel alloys given by the expressions in Eqs. 4.1.20, 4.1.21, 4.1.22 [139], T represents the temperature with $T_{i,start}$ being the transformation temperatures of the i phase ($i = l, \delta$ or γ), and g_δ and g_γ are given by the 3D meso-scale solidification model at the specified solid fraction being used in the fluid flow

simulation. Note that the shrinkage factor will vary during solidification since the individual densities ρ_δ, ρ_γ, and ρ_l are temperature-dependent.

Deformation of the semi-solid skeleton will also induce liquid flow. Assuming rigid body motion of the grains and deformation localized to the liquid phase, the increase in volumetric flow rate Δv_{liq} that is required to compensate for deformation at the scale of an individual element can be approximated as

$$\Delta v_{liq} = \frac{\dot{\varepsilon}_{sv}}{(1-g_s)} * V_{liq}, \tag{4.1.23}$$

where $\dot{\varepsilon}_{sv}$ is the volumetric part of the strain rate applied on the domain, and calculated via $\dot{\varepsilon}_{sv} = \dot{\varepsilon}_{xx} + \dot{\varepsilon}_{yy} + \dot{\varepsilon}_{zz}$, and V_{liq} represents the volume of liquid present in an element. Note that while Eq. 4.1.23 simulated the effects of mechanical deformation on fluid flow in a semi-solid, mechanical deformation itself is not directly simulated.

Applying the divergence theorem, the mass balance becomes

$$\int_{V_l^e} \nabla \cdot \vec{v}_l dV = 2 \cdot \int_{S_{sl}^e} \vec{v}_l \cdot \vec{n} dS + 2 \cdot \int_{S_l^e} \vec{v}_l \cdot \vec{n} dS + 2 \cdot \Delta v_{liq} = 0, \tag{4.1.24}$$

where V_l^e represents the total volume of the two facing tetrahendrons, $S_{sl}^e = S_v \cdot V^e$ is the dendritic solid/liquid interfacial area, V^e represents the total volume of dendrite envelope, and S_l^e represents the total lateral area of the two tetrahedral elements. Then, by substituting Eq. (4.1.14) and Eq. (4.1.15) into the second right term of Eq. (4.1.24), and assuming that the first right term of Eq. (4.1.24) can be replaced by $S_{sl}^e \cdot \vec{v}_{l \cdot n} = -S_{sl}^e \cdot \beta_s v_T$, one obtains the master fluid flow equation for dendritic flow,

$$2 \int_{S_l^e} \left(\frac{z'^2}{2\mu_l} + C_1 \right) \nabla p \cdot \vec{n} dS + 2 \int_{S_l^e} \left(C_2 e^{\frac{z'}{\xi}} - C_3 \right) \nabla p \cdot \vec{n} dS$$
$$- 2 v_T \beta_s S_{sl}^e + 2 \cdot \Delta v_{liq} = 0. \tag{4.1.25}$$

Numerical implementation

At the scale of a single element, integration of Eq. (4.1.25) over the intra-dendritic and extra-dendritic parts is computed numerically by dividing both the grain envelope length and extra-dendritic liquid channel width into $n = 1000$ segments along the height of tetrahedral element. By doing the integration and applying Green's theorem over each segment, one obtains the coefficient of the Laplacian of the pressure field, $\nabla^2 p$. Then, as it has been assumed that the flow direction is parallel to the exterior triangular facet of

each tetrahedron, the 3D mesh is simplified to a set of 3-node 2D triangular elements. The resulting pressure field is given by

$$p_l = \sum_{i=1}^{3} N_i p_i^*, \tag{4.1.26}$$

where p_i^* represents the nodal pressures, and N_i represents the shape functions of the triangular element that approximate the pressure field within element e in the local (x', y', z') coordinate system. Applying the Galerkin finite element method to Eq. (4.1.25), the elemental matrix equation is obtained:

$$[K]^e \begin{Bmatrix} p_1^* \\ p_2^* \\ p_3^* \end{Bmatrix} = b^e + \{\phi\}^e, \tag{4.1.27}$$

where $[K]^e$ represents the element stiffness matrix, b^e is the load vector which results from solidification shrinkage and/or deformations exerted on the domain, and $\{\phi\}^e$ is related to the external boundary conditions.

Once the individual element matrices have been developed, they are assembled together into the global stiffness matrix. This global matrix is then solved with a conjugate gradient linear iterative method using a free open access program C++ library known as IML++ [140]. The solution provides the pressure throughout the domain. Complete details of the numerical implementation can be found in [121].

4.1.4 Semisolid deformation model

In this section, a 3D semisolid deformation model is used and modified for the prediction of the semisolid mechanical behavior using a discrete element method [120]. This model allows for the prediction of stress and strain localization within a semisolid at a specific solid fraction with a semisolid geometry obtained via the dendritic solidification model. Like the semisolid geometry described in the prior sections, it consists of irregular arrange of solid grains (Fig. 4.7(a)) surrounded by liquid channels. Fig. 4.7(b) shows a series of tetrahedral elements representing the solid phase which are in contact with other three solid elements belonging to the same grain in Fig. 4.7(a). The fourth face of the tetrahedral element is either in contact with the symmetric element of the neighboring grain or is separated from it by a liquid film if the two facing grains are not coalescenced yet.

The deformation of a semisolid is different from the fully solid materials due to the presence of two phases: solid and liquid. The stress state is inhomogeneous as the two phases bear unequal loads and the solid phase has

a great impact on the mechanical behavior [12]. In the deformation calculation, the mechanical behavior of a semisolid is assumed to be anisotropic due a statistically large number of irregular arrangements of grains. Within each homogeneous solid phase, finite element method is applied to predict of continuous deformation while the discrete element method is used to model the discontinuous deformation of the entire domain containing two phases [120]. Similar as in the prior semisolid mechanical model [120, 134], different types of elements are used as shown in Fig. 4.7:(i) 3D solid element, (ii) multi-point constraint (MPC) elements for the continuity between the faces of solid element belongs to the same grains, (iii) contact elements at the grain boundary.

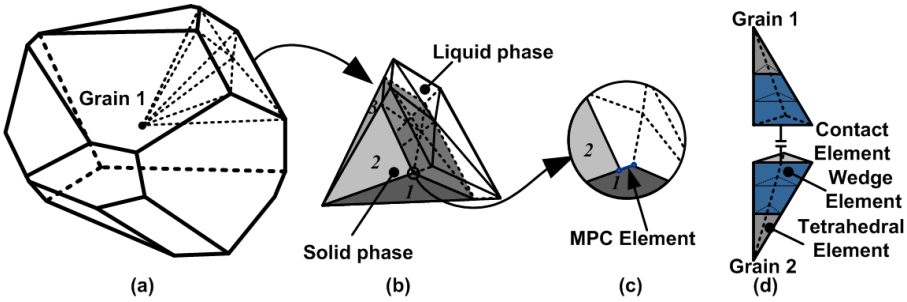

Figure 4.7: Schematic of equiaxed grains and three different types of finite element used in the simulation: (a) Voronoi grain, (b) 3D solid element consists of multiple tetrahedral elements, (c) multi-point constrained element between two nodes belong to one grain and (d) contact element located between two solid elements across the grain boundary.

Solid elements

In order to predict the mechanical behavior within each solid element, a constitutive law is used to link the stress and strain under a deformation. The isotropic elastic modulus and Poisson's ratio are assumed to be constant at high temperatures. The flow behavior of solid grains of carbon steel at various strain rates and temperatures is modeled by the following equation [141],

$$\dot{\varepsilon}_e = A \exp\left(-Q_a/RT\right) \left[\sinh\left(\beta_e K_e\right)\right]^{1/m}, \tag{4.1.28}$$

$$\sigma_e = K_e \varepsilon_e^n, \tag{4.1.29}$$

where $\dot{\varepsilon}_e$ is the effective plastic strain rate, A and β_e are constants, Q_a is the activation energy for deformation, R is the gas constant, T is the temperature, m represents the strain rate sensitivity, K_e is the strength coefficient, n is the strain hardening exponent. σ_e and ε_e represent the effective stress and strain, respectively. The deformation behavior of steel alloy is predicted utilizing the

Table 4.1: List of parameters used for δ and γ phase in the simulation [3].

	$A(s^{-1})$	Q_a (kJ/mole)	β_e (MPa^{-1})	m	n
δ phase	6.754×10^8	216.9	0.0933	0.1028	0.0379
γ phase	1.192×10^{10}	373.4	0.0381	0.2363	0.210

constitutive Eq. 4.1.28 and Eq. 4.1.29, and the parameters of δ and γ phases measured by Seol et al. [3] listed in Table 4.1 are used in this simulation.

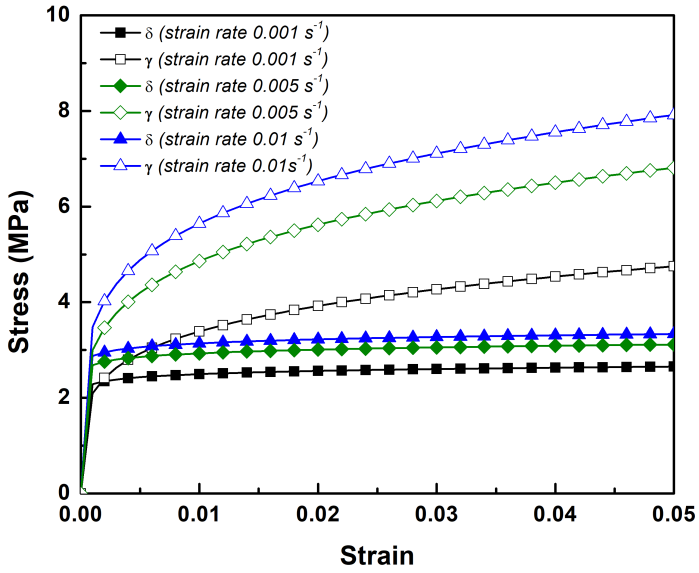

Figure 4.8: Comparison of stress and strain curve for δ and γ phase under different strain rates at 1480 °C: 10^{-3} s^{-1}, $5{\times}10^{-3}$ s^{-1} and 10^{-2} s^{-1}, respectively.

Fig. 4.8 shows the constitutive behavior of solid δ and γ phases at various strain rates at 1480 °C calculated via Eq. 4.1.28 and Eq. 4.1.29 using the parameters list in Table 4.1. The input results for both δ and γ illustrate that the stress increases with the increase strain rate. The stress of γ is shown to be larger than δ at a given strain.

The constitutive behavior of solid phase of steel containing different phases δ and γ is obtained through the rule of mixture, and the mechanical property within each dendrite envelope is treated as a porous medium due to the presence of the inter-dendritic liquid associated with very weak mechanical strength.

Multi-point constraint elements

The 1D solidification within each tetrahedral element is conducted independently where the solute exchange between the neighboring grains is not considered. This simplified 1D solidification model within each element inside a semisolid created by Voronoi tessellation fails to predict a continuous solid/liquid interface across two neighboring elements. The multi-point constraint element is used to tie two neighboring facets via the edge nodes shown in Fig. 4.7(c), achieving a continuity of displacements and stresses across the interface belongs to the same grain [142].

Contact elements

The contact elements are used to link between the solid grains. In particular, this element type permits the prediction of large sliding and finite deformations. Separation and arbitrary rotations may also be modeled. In this coupled model, a frictionless hard contact pressure–overclosure element is implemented, which assumes zero overclosure with infinite contact stiffness. The hypothesis of frictionless surface indicates that only normal pressure is transmitted between contacting surfaces. The contact element also allows to prevent the solid grain penetration. The simplified treatment of the contact element holds as the dominant factor of resistance of the liquid channel to separation is due to the liquid pressure acting on the solid/liquid interface [134].

Numerical implementation

Once the semisolid geometry and elements are created within the domain, an in-house software is then used to convert the solid phase of a semisolid geometry into finite element mesh while the liquid film remains free from meshing. Every solid phase is meshed into two wedge elements and one tetrahedral element which can be seen in Fig. 4.7(d). The coarse mesh used for the solid phase helps to save the computational time. The semisolid deformation analysis is predicted by using the finite element software Abaqus [143] and are coupled with the dendritic fluid flow model for the prediction of crack which will be presented in the section hereafter.

4.2 Defect prediction

For the prediction of cracking and segregation within a semisolid, the submodels described above are coupled together in two different ways following the flow chart shown in Fig. 4.9.

4.2.1 Semisolid cracking model

In order to predict the crack, a 3D semisolid cracking model initially developed by Sistaninia et al. [134] is extended and used in this investigation. Different from the prior model which focused on the globular structure of Al alloys, this study focuses on the investigation of hot tearing sensitivity of semisolid steel associated with peritectic transformation. The semisolid cracking model consists of several sub-models and the coupling between the sub-models follows the flow chart shown in Fig. 4.9. In this chapter, the different models incorporated inside the semisolid cracking model are briefly reviewed, followed by an introduction of the pressure-mechanical coupling process.

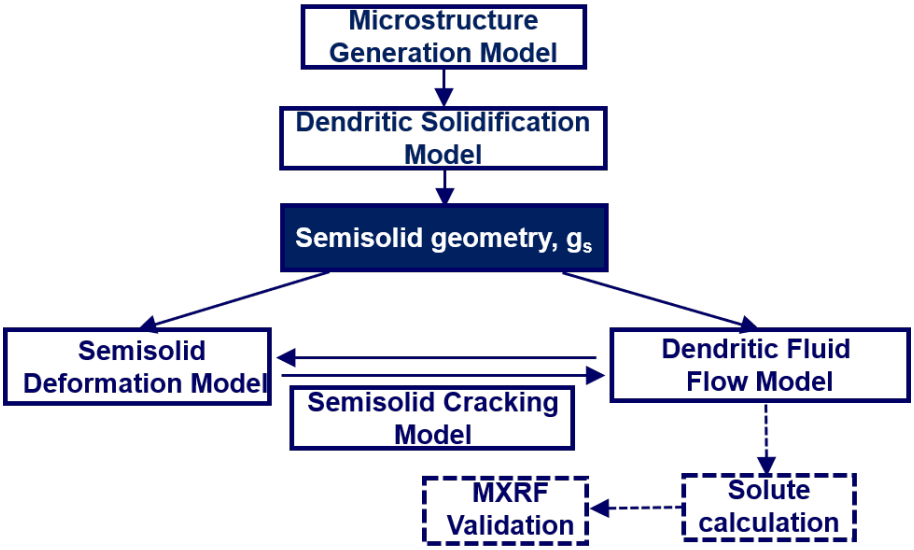

Figure 4.9: Schematic of coupling between sub-models for the prediction of cracks.

Overview of models

Given the known grain size, a microstructure generation model is firstly used to create the fully solidified equiaxed grains under the same procedures mentioned in Section 4.1.1. The fully solidified equiaxed microstructure is further split into smaller tetrahedral elements ready for the microsegregation analysis using the dendritic solidification model in Section 4.1.2. This two models allows for the prediction of semisolid geometry at a given g_s, indicated in Fig. 4.9. This semisolid geometry containing at least two phases is used for the pressure and stress calculation.

The pressure calculation is achieved by using a dendrite fluid flow model but with a different assumption from Section 4.1.3. The liquid phase in the

modified dendritic fluid flow model is assumed to be compressible and is able to compensate the solidification shrinkage and deformation via density change. The mass balance equation for the liquid phase is given,

$$\frac{\partial \rho_l}{\partial t} + \nabla \left(\rho_l \vec{v}_l \right) = 0, \tag{4.2.1}$$

where ρ_l represents the liquid density.

Integrating Eq. 4.2.1 over the two facing tetrahedral elements and using the divergence theorem, one obtains an equation similar to Eq. 4.1.25 but with an additional term related to the variation of liquid density,

$$\frac{1}{\rho_l} \int_V \frac{\partial \rho_l}{\partial t} dV + \int_{S_l^e} \left(-\frac{\kappa \left(g_{l'} \right)}{\mu_l} \right) \nabla p \cdot \vec{n} dS - v_T \beta_s S_{sl}^e + \Delta v_{liq} = 0. \tag{4.2.2}$$

The first term can be linked to the liquid pressure drop via the bulk modulus of the liquid K_l,

$$\frac{1}{\rho_l} \frac{\partial \rho_l}{\partial t} = \frac{1}{K_l} \frac{\partial p}{\partial t}. \tag{4.2.3}$$

The modified equation avoids the convergence problem at high solid fractions where the liquid is likely to form into isolated pockets. The numerical implementation of Eq. 4.2.2 is similar as Section. 4.1.3.

The modified dendritic fluid flow is then coupled with the semisolid deformation model in Section 4.1.4 for the prediction of the rheological behavior of the semisolid, the detail pressure-mechanical coupling between this two models is presented in the coming section.

Failure criterion

In order to identify the crack initiation site, a failure criterion needs to be incorporated inside the semisolid cracking model. In the prior investigations related to crack initiate prediction [134], the atmosphere-induced liquid rupture model is used. For clarification, the salient points of this failure criterion are recalled in this section.

Assuming that there is a contact between the liquid film and atmosphere, shown in Fig 4.10, it is shown that the overpressure required to overcome capillary forces at the liquid-atmosphere interface inside the micro liquid channel can be estimated by assuming a semi-cylindrical void shape with a radius denoted as r,

$$p_a - p_l = \frac{\lambda}{r} = \frac{\lambda \cos \Theta}{h}, \tag{4.2.4}$$

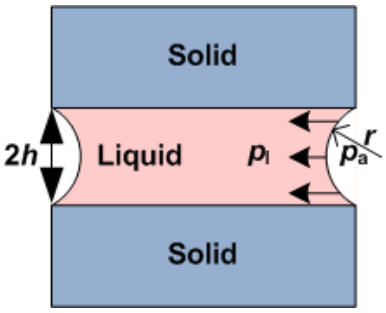

Figure 4.10: Schematic of two facing grains with a liquid film in between where a meniscus with a hemi-cylindrical shape forms.

where p_a and p_l represent the atmosphere and the liquid pressure, λ is the surface tension at the atmosphere–liquid interface, Θ is the dihedral angle and h represents half of the liquid channel width.

In steel, the presence of a small amount of solute elements such as sulfur and oxygen presenting in the liquid phase will dramatically decrease the liquid surface tension and affects the reactions between gas and liquid phase [144]. The effects of oxygen and sulfur contents on surface tension for liquid iron at 1550 °C are given as,

$$\lambda = 1788 - 281 \ln\left(1 + K_o\,[\%\mathrm{O}]\right) \mathrm{mN/m}, \tag{4.2.5}$$

$$\lambda = 1788 - 195 \ln\left(1 + K_s\,[\%\mathrm{S}]\right) \mathrm{mN/m}, \tag{4.2.6}$$

where K_s and K_o represent the absorption coefficients for oxygen and sulfur on liquid iron, and can be calculated via,

$$\log K_o = \frac{11370}{T} - 4.09, \tag{4.2.7}$$

$$\log K_s = \frac{5874}{T} - 0.95, \tag{4.2.8}$$

where T is the temperature (K). Fig. 4.11 indicates the results of surface tension calculated based on different sulfur contents and oxygen contents at 1550 °C.

Note that for an internal crack occurring in the center of the casting slabs, the lack of air makes the crack initiation mechanism different. Compared with the liquid pressure required to break the bonds in a gas-free liquid, a crack is very difficult to form due to the low strength of a high temperature semisolid [1]. However, the gas dissolved in the liquid enables the formation of porosity when the melt is supersaturated with the gas, which has been found to be a necessary condition for the initiation site of hot tearing [145, 146].

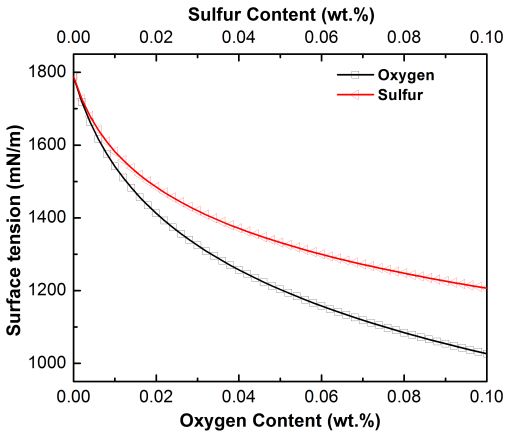

Figure 4.11: Influence of sulfur and oxygen contents on surface tension of liquid iron.

In this thesis, Eq. 4.2.4 is used to simulate the liquid rapture at the surface of a semisolid, and the ruptured liquid will propagate into the liquid channels directly connected to it. The value of $\cos\Theta$ is fixed to 1 due to the good wettability of liquid steel on the solid grains. The surface tension of liquid steel on the surface of a semisolid is assumed to be higher than the interior atmosphere-liquid layer due to the negligible oxide layer inside the domain. This criterion is implemented within the present mesoscale model through a multi-step technique.

Numerical implementation of coupling

For the prediction of cracking in semisolid steel, all the sub-models are coupled following Sistaninia's method [134]. First, with a given semisolid geometry obtained from dendritic solidification model (DSM) shown in Fig. 4.9, the coupling procedures are illustrated in Fig. 4.12. The dendritic fluid flow model (DFFM), semisolid deformation model (SDM) and semisolid cracking model (SCM) are coupled incrementally for the prediction of crack within a semisolid until the overall failure occurs, where the SDM is used to determine the mechanical response of the mushy zone under imposed displacement. The results from SDM provide the strain rate on each liquid channel and updated liquid channel width, which are used for the pressure calculation via DFFM.

The iteration starts when the output pressure obtained from DFFM is imposed to SDM for the next iteration, and ends until p_l is converged. Finally, the failure criterion mentioned in Section.4.2.1 will be applied to liquid channels when the convergence of p_l is reached. Once a liquid channel ruptures, the liquid initially located at the cracked channel will be sucked into the rest of the liquid channels that are not cracked, and the pressure in the ruptured channel

is set to be p_a for the semisolid stress calculation as this channel between two facing solid grains is open and filled with air. The cracked liquid channel will no longer participate in the fluid flow calculation and is closed by fixed a local displacement.

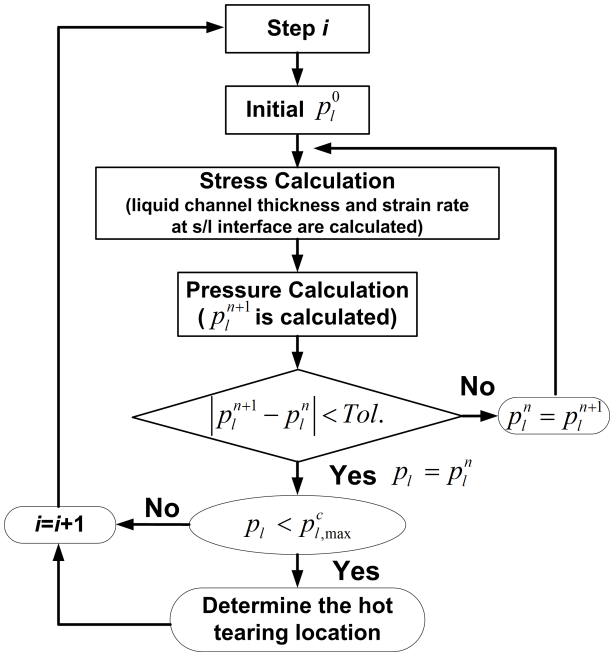

Figure 4.12: Flow chart of the hydro-mechanical coupling procedures following Sistaninia et al. [1].

4.2.2 Mesoscale solute transportation model

Macrosegregation during solidification is often resulted from complicated factors as identified in Section 1.3.2 occurring at different length scales. Another application of the present mesoscale model is to predict the macrosegregation at a mesoscale. Building on the 3D mesoscale dendritic solidification model in Section 4.1.2 and dendritic fluid flow model in Section 4.1.3 as shown in Fig. 4.9, a solute transport model is proposed that directly combines solute transport at the scale of the casting with solute partitioning at the scale of the grains. The random arrangement of the equiaxed grains created by the microstructure generation model in Section 4.1.1 allows for consideration of stochastic effects and the interaction between the liquid and solid is also considered. In contrast to conventional continuum methods that are based on the averaging over a representative volume element, the discrete mesh representing the geometry of individual grains and the connectivity of the liquid channels

allows for an accurate prediction of the relative motion between intra-dendritic flow and solid grains.

In this section, first, the methodologies for creating intra-dendritic fluid flow through a dendritic network are reviewed. Second, the 3D mesoscale solute transport model is introduced. Then, the numerical implementation based on the finite element method is described.

Intra-dendritic fluid flow

Liquid flow through the intra and extra dendritic regions is predicted via a mesoscale fluid flow model in Section 4.1.3 for a given solid fraction and average grain size. The relative amounts of flow through the intra and extra dendritic regions depends on the solidification morphology predicted by the solidification model. For the present investigation, only the case of intra-dendritic flow is considered. During continuous casting of steel, the common grain size near the centre of the slab can be up to ∼800 µm. For such large grains, the microstructure predicted via the solidification model is fully dendritic and reduces the model to have only intra-dendritic liquid. In other words, even at low solid fraction a dendrite envelope reaches to its facing dendrite thus removing all the extra-dendritic liquid.

Similar as Section 4.1.3, assuming 2D quasi-steady-state as well as irrotational flow that is parallel to the triangular facet where the two tetrahedrons meet, and neglecting both gravity and pressure gradients along the length of the element, the intra-dendritic fluid velocity can be expressed as

$$-\nabla p - \frac{\mu_l}{\kappa\left(g_{l'}\right)}\vec{v}^{id} = 0. \tag{4.2.9}$$

This expression is equivalent to Eqs. 4.1.11 and 4.1.12 in Section 4.1.3 assuming that $g_l^{ed} = 0$. By conducting a mass balance over the two facing tetrahedrons and assuming liquid incompressibility ($\nabla \cdot \vec{v}^{id} = 0$) the pressure within the mushy is then given by

$$\int_{S_l^e} \left(-\frac{\kappa\left(g_l'\right)}{\mu_l}\right) \nabla p \cdot \vec{n} dS - v_T \beta_s S_{sl}^e + \Delta v_{liq} = 0. \tag{4.2.10}$$

With appropriate boundary conditions as specified in [147], Eq. 4.2.10 can then be solved to determine the mesoscale pressure field within the semi-solid domain containing dendritic microstructures.

Mesoscale solute transport model

The governing equation for steady-state solute transport due to convection and diffusion in the intra-dendritic liquid at the mesoscale resulting from solidification shrinkage and mechanical deformation is given by

$$\vec{v} \cdot \text{grad } c_l - div(D_l \text{ grad } c_l) = Q, \tag{4.2.11}$$

where D_l represents the diffusion coefficient of the solute in liquid phase, $\vec{v}$ is the intrinsic fluid velocity and Q is the source term representing the solute transfer rate at the solid/liquid interface due to solute partitioning, i.e.,

$$Q = S_{sl}^{e} v_T c_l^* \left(1 - k\right), \tag{4.2.12}$$

where c_l^* is the equilibrium solute concentration in the liquid phase at a temperature of interest, and k is the partition coefficient. The solid phase is assumed to be rigid and stationary, $\vec{v}_s = 0$. Solute flow due to buoyancy is not considered.

Numerical implementation

In order to determine the solute distribution within the mushy zone, the variation in $\vec{v}$ throughout each dendritic grain must be known. This quantity can be determined from the fluid flow model by applying Darcy's law utilizing the known pressure field and local permeability to calculate the intra-dendritic flow velocity $\vec{v}^{id}$ (also known as the superficial fluid velocity),

$$\vec{v}^{id} = -\frac{\kappa\left(g_l'\right)}{\mu}\left(\frac{\partial p}{\partial x'} + \frac{\partial p}{\partial y'}\right), \tag{4.2.13}$$

and then transforming $\vec{v}^{id}$ to $\vec{v}$ via

$$\vec{v} = \vec{v}^{id} / g_l^{id}. \tag{4.2.14}$$

By applying triangular shape functions, a single intrinsic velocity can then be determined for each element,

$$\vec{v}_{x'} = -\frac{\kappa\left(g_{l'}\right)}{\mu g_l^{id}}\left(\frac{\partial(N_i \cdot p_i)}{\partial x'}\right), i = 1, 2 \text{ or } 3. \tag{4.2.15}$$

$$\vec{v}_{y'} = -\frac{\kappa\left(g_{l'}\right)}{\mu g_l^{id}}\left(\frac{\partial(N_i \cdot p_i)}{\partial y'}\right), i = 1, 2 \text{ or } 3. \tag{4.2.16}$$

where x' and y' represent the velocity components parallel to the triangular facet as illustrated in Fig. 4.6(c) (the assumptions listed previously result in a zero pressure gradient and thus zero flow in z'), and N_i represents the

triangular shape functions. $\vec{v}$ will vary spatially throughout the mesoscale domain due to the variations in pressure gradient and local permeability.

The solute distribution within the mushy zone is then determined as follows. First, by making similar assumptions to the fluid flow model, the 3D tetrahedrons are simplified to a set of 3-node 2D triangular elements. Second, the solute concentration in the liquid phase within each element is approximated as

$$c_{elem} = \sum_{i=1}^{3} N_i c_i, \tag{4.2.17}$$

where the c_i are the nodal solute concentrations in the liquid phase, and the N_i are the triangular shape functions to approximate the solute concentration field within the local (x', y', z') coordinate system. Applying the Galerkin finite element method to Eq. (4.2.11), the elemental matrix equation is obtained,

$$[K]^e \left\{ \begin{array}{c} c_1 \\ c_2 \\ c_3 \end{array} \right\} = b^e + \{\phi\}^e, \tag{4.2.18}$$

where $[K]^e$ represents the element stiffness matrix, b^e is the load vector depending on the solute partitioning, and $\{\phi\}^e$ is the external boundary condition imposed, i.e.

$$[K]^e_{ij} = \int_{\Omega} N_i \vec{v}_{x'} \frac{\partial N_j}{\partial x'} + N_i \vec{v}_{y'} \frac{\partial N_j}{\partial y'} + D \frac{\partial N_i}{\partial x'} \frac{\partial N_j}{\partial x'} + D \frac{\partial N_i}{\partial y'} \frac{\partial N_j}{\partial y'} dS, \tag{4.2.19}$$

$$\{b\}^e_i = \int_{\Omega} N_i Q dS, \tag{4.2.20}$$

$$\{\phi\}^e_{ij} = \int_{\partial\Omega} N_i q dS, \tag{4.2.21}$$

where q represents the solute flux at the boundaries and remains only on the external boundary of the model domain, and i and j are counters representing the local node numbers $(i, j = 1, 2, 3)$.

Once the individual element matrices have been developed, they are assembled together into the global stiffness matrix, and then solved via matrix operations using a free open access C++ matrix solver/library known as IML++ [140]. Due to the presence of the velocity in Eq. (4.2.11), $[K]^e$ is not symmetric and thus must be solved via a generalized minimal residual method.

4.3 Validation of mesoscale models

The 3D mesoscale sub-models and coupled models described in the prior sections require validations before further applications. Note that the microstructure generation model and the dendritic solidification model are not necessary for validation as they only provide the semisolid geometry at a specific solid fraction used for pressure and deformation analysis. The results of the dendritic fluid flow model can be compared with the empirical equations which are already validated with experimental measurements. Due to the lack of high temperature constitutive data for semisolid steel, in this thesis, validation of the semisolid cracking model is achieved by comparing the results with the semisolid tensile test measurements conducted by Seol et al. [27]. The results from the mesoscale solute transport model can be validated with the solute map measured experimentally.

In this section, the semisolid tensile experiment used for validating the coupled semisolid cracking model is presented firstly followed by the validation work for the segregation prediction via MXRF. In the validation of the mesoscale solute transport model, the materials used for the characterization is described. Sample preparations and the casting conditions for these samples will also be presented. Then, an introduction of the apparatus is described, followed by the test methodology and quantitative characterization method.

4.3.1 Validation of semisolid cracking model

Due to the difficulty associated with the measurement of high temperature properties of semisolid steel, the tensile strength of the semisolid steel is limited. Seol el al. [27] conducted a high temperature tensile test using the Gleeble 1500 system to characterize the semisolid mechanical behavior of carbon steel during solidification. The detailed information related to the experimental procedures are summarized as follows: the chemical composition compositions of the sample machined from the continuous casting slab is listed in Table 4.2. In order to reproduce the continuous casting process, the test sample was fully melted by electrical current and then cooled at a constant cooling rate of 1 K/s during the tensile test experiment. This cooling condition results the formation of equiaxed grains with an average grain size of $\sim$ 100 µm. A tensile load with a strain rate of 10^{-2} s^{-1} was imposed on the sample during solidification. The measured ultimate tensile strength was reported in a relation to solid fraction evaluated by a microsegregation model [148].

Readers can refer to Ref. [27] for the detailed experimental procedure used during the semisolid tensile test.

Table 4.2: Chemical compositions of the sample test in Gleeble machine [27] (wt.%)

	C	Mn	Si	P	S
Steel sample	0.12	0.59	0.25	0.015	0.008

4.3.2 Validation of mesoscale solute transport model

Materials

To perform a macroscale solute mapping experiment via MXRF, a steel sample was cut from the continuously casting slab cast at a constant speed of 0.8 m/min from Arcelor Mittal Dofasco at Hamilton, Canada. The experimental samples are approximated as Fe-0.105wt.%C-1.55wt.%Mn alloys. Fig. 4.13 shows the location of the sampling. The selection of this steel grade is due to its high susceptibility to segregation associated with peritectic transformation; besides, the sampling is located at the center, which allows for the investigation of centreline segregation. The sample size of 90 mm x 90 mm is associated with longer solidification time and likely to show macrosegregation over such a large scale. The sample was prepared using standard metallographic procedures: it was manually ground using the 320, 400, 600, and 800 SiC papers in order to remove the cutting edges on the surface, and then thoroughly cleaned by swabbing the specimen in the running water and dried immediately. The sample was finished with parallel sides ready for the analysis.

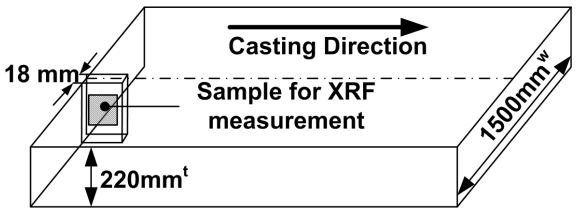

Figure 4.13: Schematic diagram of sampling within the continuous casting slab.

Apparatus

MXRF introduced in Section 2.2.1 is used to measure the solute map over the well prepared steel sample. The apparatus used in this investigation is presented in this section.

The front-view of the apparatus is shown in Fig. 4.14(a). This instrument is built at Arcelor Mittal Dofasco with the collaboration of IXRF Systems

(Texas, USA). It is a scaling-up of the common XRF technique and consists a chamber equipped with a sampling scanning stage shown in Fig. 4.14(b), an X-Ray excitation source and a 80 mm^2 liquid-nitrogen cooled, Silicon Drifted Detector (SDD). The scanning stage is with a dimension of 320 mm x 320 mm motorized in X-Y-Z direction, allowing for a maximum sample size of 200 mm x 100 mm by 20 mm thick. The source is a rhodium X-Ray tube with maximum operation at 50 kV and 1 mA. The front door of the chamber allows for sample placement and change, and the experiment is conducted either in air or vacuum environment.

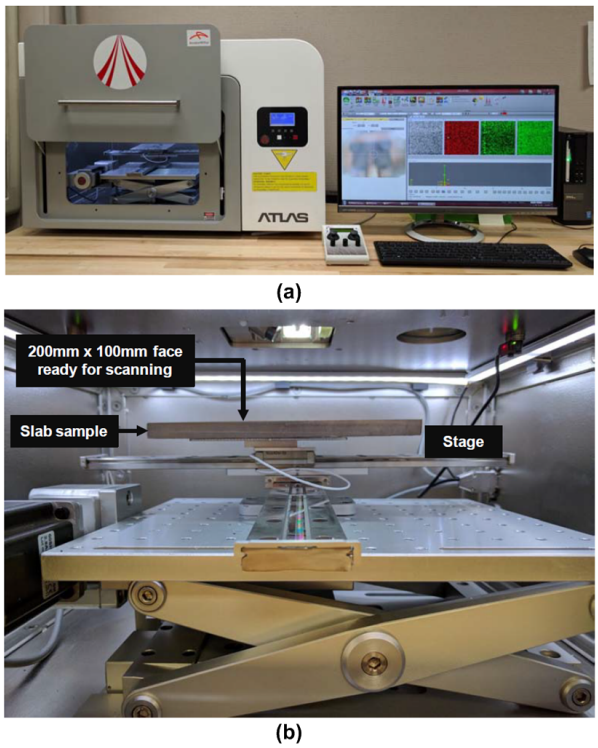

Figure 4.14: (a) Photograph of experimental setup of Micro X-Ray Fluorescence device at Arcelor Mittal Dofasco, and (b) MXRF scanning stage [25, 26].

This apparatus is also incorporated with a Software Suite (Iridium), including an operational control system, spectral data acquisition and post processing, MXRF mapping of line and area scans and elemental ratio mapping for segregation analysis. The unique combination of different software packages manages to detect a wide range of elements from Sodium to Uranium in multiple environments.

Safe operation is also guaranteed respected to the X-Ray during the experiment. The X-Ray source will be automatically shut down when the front chamber door is open, and any X-Ray exposures can be avoided; Also, the

emergency X-Ray shut-off button in the front panel manages to close the X-Ray source when any malfunctions occur. Once the samples are removed from the slot will be immediately detected by a camera and a laser sensor, and the lock-out key will stop all the operations to prevent the damage of the source and detector. The detail introduction of this apparatus can also be found in Ref. [25, 26].

Test methodology

The well prepared sample was then mounted on the scanning stage before MXRF analysis was carried out on the cross-section of sample with a target area of 8100 mm^2. During the test, atoms on the surface of the sample were excited by X-radiation generated through a rhodium X-Ray tube which knocked out some electrons from the inner electron shells. Electrons from outer electron shells filled the voids in the inner shells, and emitted a fluorescence radiation. The X-Ray beam was focused on the sample by a polycapillary optic to produce spot size varies from 40 µm to 2.0 mm. For the current investigation, beam size was 250 µm which is definitely small enough for the purpose of detecting macroscale elemental inhomogeneity. The beam energy used was 50 kV, with a beam of current 400 µA. Finally, the characteristic X-Ray fluorescence generated by the alloying elements in the steel sample was then detected by the SDD.

Quantitation

Once the XRF spectral data of the entire scanning area are obtained, the Iridium software suite automatically performs post-processing calculations to convert the XRF intensities to wt.% data. There are two methods for quantitation developed by IXRF: Fundamental Parameter method (FP method) and Least Squares methods (LS method). For detail information regarding these two methods, please refer to [25, 26]. LS quantitation has been tested and validated at ArcelorMittal Dofasco, and used in the present study to measure the centreline segregation. When the LS quantitation is finished, the Iridium software suite generates the Mn wt.% map of the scanning surface.

Chapter 5

Results and Discussions

In this chapter, the model developed in this thesis is applied to investigate solidification behavior of steel. The output from the microstructure generation model in Section 4.1.1 is used as an input for solidification, fluid flow, deformation and solute transport analysis. This chapter firstly provides the results from the sub-models: dendritic solidification model, dendritic fluid flow model, semisolid deformation model followed by the coupled models including the semisolid cracking model and the mesoscale solute transport model, respectively. Note that the results of the semisolid deformation model are not presented explicitly due to its contribution to predict cracking and are included in the semisolid cracking model.

In the dendritic solidification model, the solidification of equiaxed grains are discussed firstly. The results of the dendritic fluid flow model are presented hereafter, including detailed investigations of permeability in a wide combination of microstructures, alloy compositions and flow configurations and the results are also assessed in the context of casting defects. The semisolid mechanical behavior in responding to deformation and its sensitivity to cracking under different conditions are presented and discussed in the semisolid cracking model. Finally, another application of this mesoscale model is to predict the centreline segregation within the continuous casting slab induced by solidification shrinkage. The result of this application is compared with the experimental measurement via MXRF; the effects of semi-solid mechanical deformation and alloy composition on the degree of segregation are also discussed. Note that the properties of steel is approximated as a binary Fe-C alloy and the influence of other alloy elements are neglected in this investigation.

5.1 Dendritic solidification model

Given the microstructure generated by the microstructure generation model shown in Section 4.1.1, the solidification process of each individual grain is

Table 5.1: List of parameters used in the simulation for Fe–C alloy [28, 29, 30, 31, 32]

	Property value
ΔS_f (J K^{-1} m^{-3})	1.07×10^6
η (nm)	5
γ_{sl} (J m^{-2})	0.319
D_l (m^2/s)	2.0×10^{-8}
D_δ (m^2/s)	6.0×10^{-9}
D_γ (m^2/s)	1.0×10^{-9}
Γ (m K)	1.9×10^{-7}
k	0.17
T_m ($^\circ C$)	1538
T_p ($^\circ C$)	1493
m_l (K wt frac^{-1})	-84.90

simulated using the 3D dendritic solidification model described in Section 4.1.2. The relevant material properties used in the simulation are listed in Table 5.1.

In this section, a description of the gradual formation of grain clusters during solidification which is given to show the disappearance of liquid films between the neighboring two grains is presented; and the influence of carbon composition, cooling rate and grain size on the microstructure evolution and liquid channel width distribution is discussed.

5.1.1 Grain cluster formation

As mentioned in Section. 4.1.2, the solidification model is able to reproduce the microstructure morphology evolution during solidification. The transition from individual solid grains surrounded by continuous liquid films to the formation of a single coherent solid cluster in a peritectic alloy containing 0.16 wt.% carbon is given in Fig. 5.1, where the domain is continuously cooled down at a cooling rate of 50°C/s. The coalescence undercoolings shown in Fig. 4.4 will be used as the input data for the grain cluster formation analysis.

Fig. 5.1(a) shows the morphology of grain clusters at different times (0.53 s, 1.07 s, 1.66 s, 2.63 s, 2.72 s and 2.79 s), where each color within the domain represents a single grain cluster that consists of multiple/single grain(s). During initial solidification, the grains are separated by continuous liquid films, and the number of clusters is equal to the number of grains. As grains coalescence, the size of the largest grain cluster grows, reducing the number of liquid films between individual grains. Further, the liquid channel thicknesses will narrow to a few nanometers. Due to different misorientations between two

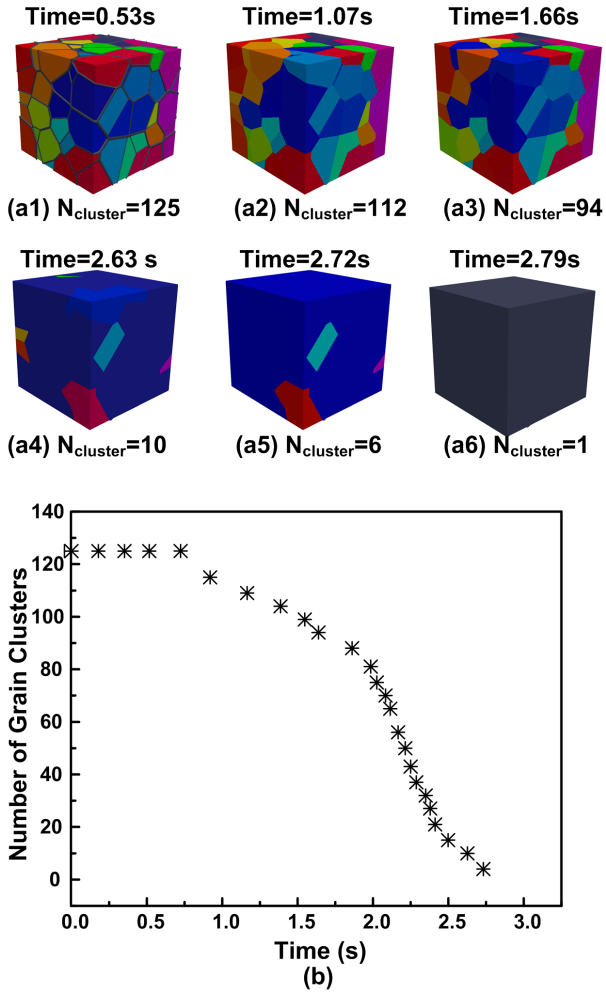

Figure 5.1: Simulation domain (5mm×5mm×5mm) containing 125 grains for a Fe-0.16wt.%C alloy: (a) coalescence of grain clusters at different time; (b) evolution of the number of grain clusters as a function of time.

distinct grains, the required coalescence undercoolings for bridging are different depending on their respective grain boundary energies. Based the energies given in Fig. 4.4(b), most of the grain boundaries are repulsive and thus neighboring grains will only coalesce once the necessary undercooling temperature is reached. Fig. 5.1(a2 – a5) all contain a solid fraction greater than 0.99; at such a high solid fraction, the presence of liquid films will increase hot tearing susceptibility when deformation is applied. Finally, all 125 grains coalescence to form a single grain cluster at 2.79 s, shown in Fig. 5.1(a6). At this point, the material is able to sustain tensile deformation, having achieved mechanical coalescence. The evolution in grain clusters with time is quantified in Fig. 5.1(b). As can be seen, the speed of grain coalescence first increases because many of the grains require only a low coalescence undercooling, and then decreases because the final liquid films require significant undercooling to disappear.

5.1.2 Microstructure evolution

Influence of carbon content

The solidification morphology of various Fe-C alloys (non-peritectic: 0.07wt.%; hypo-peritectic: 0.12wt.%, peritectic: 0.16wt.% and hyper-peritectic: 0.18wt.%) is compared in Fig. 5.2 at three different temperatures. All simulations used the same cooling rate (50°C/s) and the same microstructure (500 µm average grain size). For the non-peritectic grade at high fraction solid, Fig. 5.2(a), it can be seen that many of the liquid channels are quite narrow although a few liquid pockets remain. As the grains solidify, they form a coherent solid (Fig. 5.2(a2). The short freezing range results in limited hot tearing susceptibility. In comparison, a hypo-peritectic grade has a lower solid fraction at the same temperatures, and thus wider liquid channel widths, Fig. 5.2(b1), and multiple liquid pockets coexisting with the solid phase. At T=1492.2°C, a thin layer of austenite (highlighted in red) forms at δ/L interface, Fig. 5.2(b2), concurrently narrowing the remaining liquid channel width without enabling coalescence. Considerable liquid is required at this temperature to feed the shrinkage associated with solidification and the peritectic transformation. The austenite phase then continues to grow into the liquid and δ phases as temperature decreases, resulting in a microstructure shown in Fig. 5.2(b3). The solidification of peritectic and hyper-peritectic grades are shown in Fig. 5.2(c) and (d). With increasing carbon content, the liquid pockets increase in number and size. Compared with the microstructure of the peritectic grade shown in Fig. 5.2(c1), the hyper-peritectic grade (Fig. 5.2(d1)) tends to display thicker liquid channel widths enabling easy liquid feeding. As solidification proceeds, the peritectic phase is seen to form, Fig. 5.2(c2-c3) and (d2-d3). In the hyper-peritectic grade, a number of liquid pockets remain that could feed the shrinkage, whereas these pockets are largely absent in the peritectic grade and do not

exist in the hypo-peritectic grade when the peritectic transformation occurs. Given the differences in composition, a greater amount of austenite forms in the hyper-peritectic grade as compared to the peritectic, and hypo-peritectic grades.

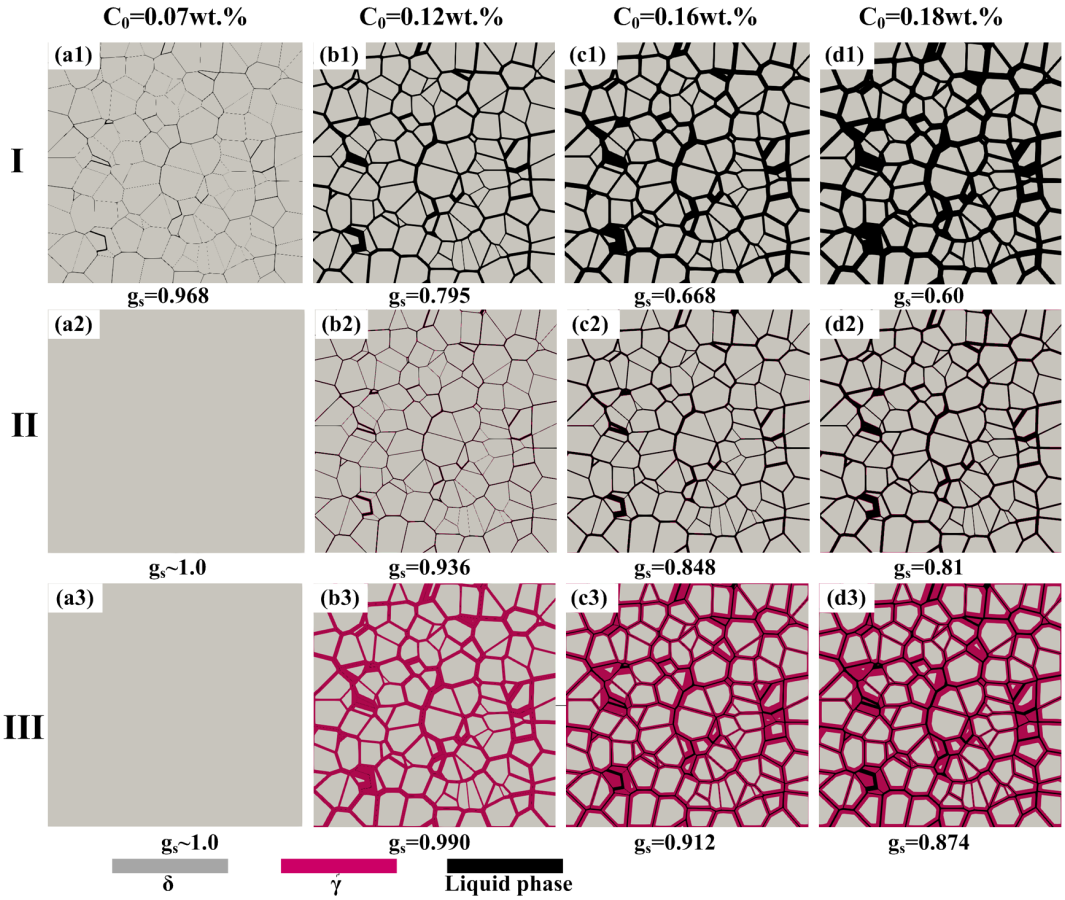

Figure 5.2: 2D Cross-sections from the 3D meso-scale solidification model of steel consisting of 1000 grains and a total domain size of 125 mm^3. (a-d) represent simulations with different carbon compositions, each for three different temperatures. (I-III) presents three different temperatures of 1507.1°C, 1492.2°C and 1491.8°C, respectively. Note that g_{l_extra}~0.

Fig. 5.3 quantifies the variation in liquid channels widths in the three peritectic grades just after the peritectic transformation has occurred, corresponding to Fig. 5.2(b3, c3, and d3). As can be seen, thicker liquid channel widths exist with higher carbon contents thus reducing hot tearing susceptibility at a given temperature as compared to the hypo-peritectic grade. Specifically, the majority of the liquid channel widths is ~28 µm for Fe-0.16wt.%C and 2 µm for Fe-0.12wt.%C. Of course, the solid fraction is also lower for these cases but nevertheless the thin liquid channels make feeding very difficult at the point

where liquid is needed to support the shrinkage associated with the peritectic transformation.

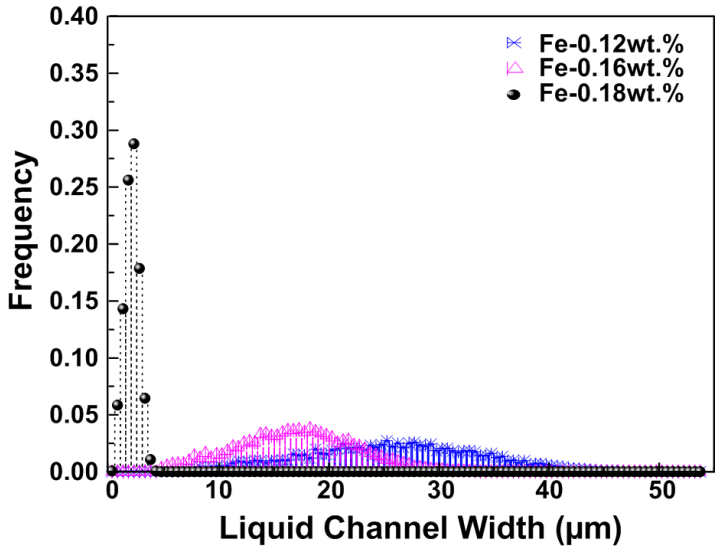

Figure 5.3: The distribution in liquid channel widths for cases (b3), (c3), and (d3) from Fig. 5.2 corresponding to compositions of 0.12wt.%, 0.16wt.%, and 0.18wt.%

It should be noted that the equivalent liquid channels shown in Fig. 5.2 represent the intra-dendritic liquid; as shown in Fig. 4.3(b) the dendrite tip quickly reaches the grain edge under high (industrial) cooling rate conditions. Distinguishing between intra-dendritic liquid and the extra-dendritic liquid is of vital importance with respect to their relative effects on flow hindrance. For equivalent amount of liquid flow, the permeability of the intra-dendritic region will be much less in the extra-dendritic region because of the additional presence of the dendrite. Conceptually, grains that solidify with a globular microstructure will have improved flow as compared to dendritic microstructure at equivalent solid fraction. Numerically, this is shown through the solid/liquid interfacial area concentration S_v. For dendritic structures the S_v term, related to the secondary arm spacing [52, 78], will be much larger than globular structures, which in turn results in a greater resistance to the liquid flow in the mushy zone as predicted by the Carman-Kozeny equation [89]. Lower permeability of the mushy zone indicates a poor feeding scenario and leads to higher pressure drop which would accelerate the formation of hot tearing. The feeding behavior of various semi-solid microstructures with both dendritic and globular morphology can be examined using the Darcy-Brinkman equation, and will be the subject of Section 5.2.

Influence of cooling rate

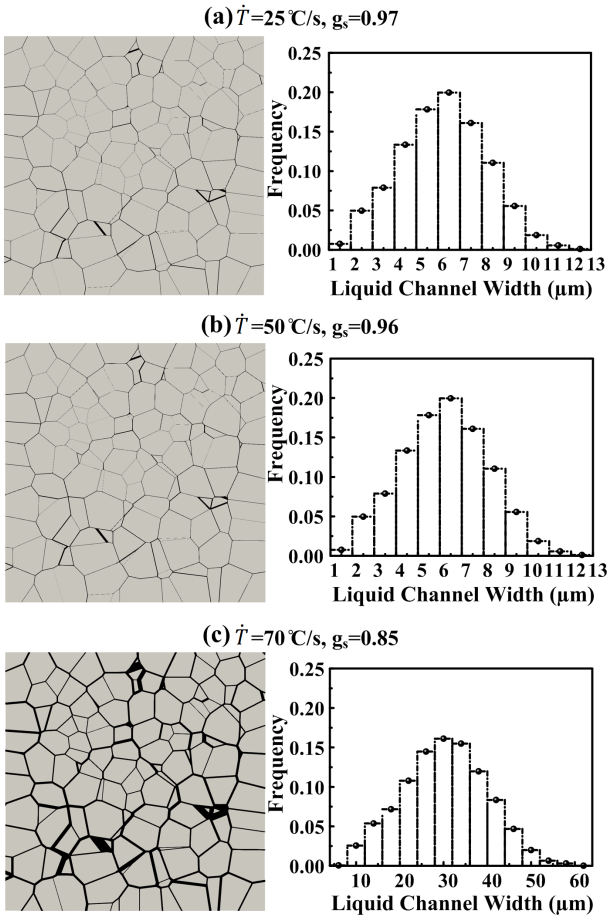

Figure 5.4: The evolution of semi-solid microstructure and the liquid channel thickness within the domain size of 125 mm^3 consisting of 1000 grains for a Fe-0.07 wt.%C alloy at T=1507°C under different cooling rates: (a) 25 °C/s; (b) 50 °C/s and (c) 75 °C/s. Note that $g_{l\_extra} \sim 0$.

Fig. 5.4 compares the meso-scale model predictions of the semi-solid microstructure for a Fe-0.07 wt.%C alloy solidified at three different cooling rates (25 °C/s, 50 °C/s and 75 °C/s), along with the corresponding distribution in liquid channel widths. All three images represent the same temperature, 1507°C. The secondary dendrite arm spacing used in the solidification model is cooling rate-dependent and will decrease with increasing cooling rate. The results demonstrate the ability of the solidification model to capture the differences in microstructure evolution under different cooling rates. At the temperature provided, the solid fraction decreases from 0.97 to 0.85 with increasing cooling rate. This is expected since higher cooling rates show a greater deviation from the equilibrium conditions leading to a decrease in the solid fraction

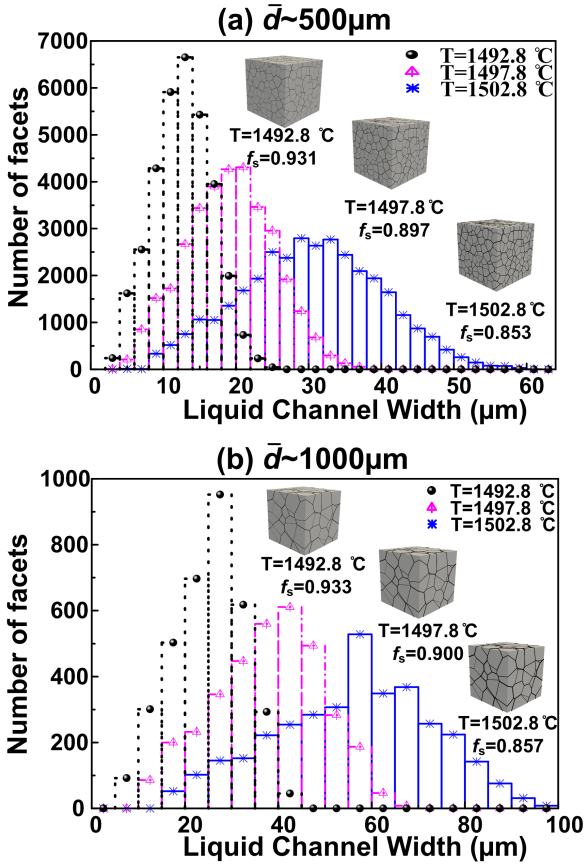

Figure 5.5: The evolution of liquid channel width at different temperatures within the domain size of 125 mm^3 for a Fe-0.16 wt.%C alloy consisting grains with average grain size of: (a) 500 μm; (b) 1000 μm. Note that g_{l_extra}~0.

at the same temperature compared with lower cooling rate. Further, a significant change in the liquid channel migration can be observed. A higher cooling rate of 75°C/s results in a structure with thicker liquid channel thicknesses as compared to the thinner liquid channels observed in the microstructure when the cooling rates are 25°C/s and 50°C/s. The localization of the liquid between the grains and the liquid pockets remain obvious when the cooling rate is high. The liquid channel widths shift from an average of 7.5 μm to ~30 μm with the increase in cooling rate.

Influence of grain size

Experimental measurement on grains size in steel indicates that the value ranges from the 400 to 800 μm near the surface of the cast slab, and 600 to 1600 μm at the bottom of oscillation marks [149]. The size of abnormally coarse

grains, can be up to seven millimeters [150]. Regardless of the mechanism behind the formation of these large austenite grains, it is thought that they originate from large primary ferrite grains [151]. In this section, the influence of two different average grain sizes, 500 µm and 1000 µm, on the microstructure evolution of Fe-0.16 wt.%C is investigated. The cooling rates used for grain size of 500 µm and 1000 µm are 50 °C/s and 6.25 °C/s based on an empirical equation relating the average final grain size with cooling rate [12].

The simulated semi-solid microstructure and the liquid channel width variation at three different temperatures (T=1502.8 °C, 1497.8 °C and 1492.8 °C) are shown in Fig. 5.5. First, independent of grain size, the solid fraction increases with a decrease in temperature along with the narrowing of the liquid channel widths as seen in both Fig. 5.5(a) and (b). At low solid fraction, the liquid channels vary considerably in size whereas at high solid fraction they are more likely to localize around a unique value. Second, the microstructure evolution clearly depends on the average grain size with numerous thin liquid channels in the domain with 500 µm grains and few large channels in the one with 1000 µm grains at the same temperature. The quantification of channel width for both grain sizes show a Gaussian-like distribution at all temperatures although some discrepancy exists. As indicated in the figure, the number of facets in the domain with finer grain is about seven times as large as compared with the coarser domain, and the overall solid/liquid interfacial area associated with smaller grains is 7469 mm^2 which is much larger than large grains of 3389 mm^2. Third, there is also a slight difference in the solid fraction of the two grain sizes for the same temperature. This is due to the statistical nature when placing grain nuclei inside a domain and performing a Voronoi tessellation. Higher cooling rates should also lead to a greater deviation from the equilibrium solidification, and cause a lower overall solid fraction, also the effect is seen to be marginal between cooling rates of 6.25 °C/s and 50 °C/s.

5.1.3 Hot tearing sensitivity analysis

The main purpose of the present research has been to develop a meso-scale semi-solid framework for simulating the solidification of steel, and to provide quantitative information about the distribution of liquid channel widths and the proportion of each phase within individual grains for different physical and process parameters. It is well known that hypo-peritectic alloys are more sensitive to hot tearing as compared with other steel compositions. As shown in Fig. 5.2(b3), the liquid channel widths for this chemistry are much smaller than the ones found in peritectic and hyper-peritectic grades. The shrinkage caused by peritectic transformation requires additional liquid over top of the solidification shrinkage. Due to the thin liquid channel widths predicted to be present in the hypo-peritectic grade when the transformation occurs, the

feeding through these liquid channels will be quite difficult. This is likely to increase hot tearing susceptibility. The present model thus demonstrates the underlying microstructure responsible for high hot tearing susceptibility in hypo-peritectic grades that has been previously experimentally reported [55]. Further, the results given in Fig. 5.4 indicate that larger cooling rates are more likely to lead to a lower overall solid fraction and thus wider liquid channels as compared with small cooling rates. These results are consistent with experimental findings that slow-cooled castings can sometimes be difficult to feed and thus prone to hot tearing. Finally, it is known that transverse cracks are usually found around abnormally coarse grains [152]. Based on Fig. 5.5, it is hypothesized that the larger interfacial area of small grains, and the resulting even distribution of liquid channels and coalesced channels provide better liquid feeding in response to tensile deformation [153].

5.2 Dendritic fluid flow model

To study liquid feeding within a semisolid, the microstructure and the solid fraction of individual grain needs to be determined first; the local solid fraction predicted by the dendritic solidification model provides both the local permeability at the grain scale through Eq. 4.1.13 and the extra-dendritic liquid channel width.

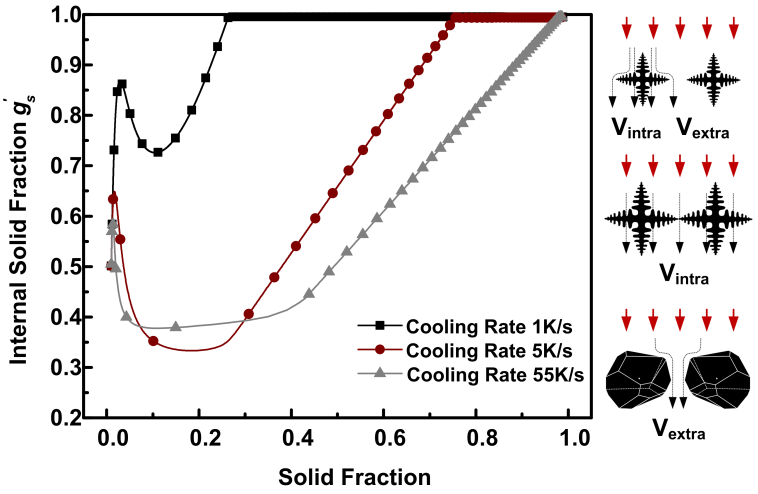

Figure 5.6: Internal solid fraction evolution within a single grain with a final diameter of 300 µm under three cooling rates along with the schematic diagrams of intra-dendritic, extra-dendritic and both fluid flow types.

Fig. 5.6 shows the evolution in internal solid fraction ($g_s' = 1 - g_l'$) given by the solidification model under three cooling rates (1, 5, and 55 K/s) for an

Fe-0.07 wt.%C grain with a final diameter of 300 µm, along with schematics of the corresponding flow patterns.

At the highest cooling rate of 55 K/s, the solidification model predicts a semisolid structure where the dendrite tips touch each other at low solid fraction, and thus the flow would be intra-dendritic as illustrated in the "upper right" diagram of Fig. 5.6. As g_s increases, the permeability of the porous medium would correspondingly be reduced. For the low cooling rate of 1 K/s, the grain morphology transitions from dendritic to globular at g_s=0.22 as $g_s' \to 1$. It is at this point that the existing dendrite structure becomes fully solid; the remaining extra-dendritic liquid within the element then solidifies in globular fashion. In a globular grain morphology, the permeability within the dendrite envelope is zero, and fluid flow will only take place in the extra-dendritic region as shown in the "middle right" diagram. At moderate cooling rates, both intra-dendritic and extra-dendritic flow can take place as shown in the "lower right" diagram since the grain is dendritic yet the dendrites from adjoining grains have not yet touched. In the case of 5 K/s, this flow pattern is possible until $g_s \sim 0.75$ at which point the flow would become extra-dendritic since $g_s' \to 1$.

The flow patterns qualitatively described in Fig. 5.6 can be quantitatively described using the 3D fluid flow model. For these simulations, a domain 6×6×6 =216 mm^3 with 8000 cubic grains each 300 µm in equivalent diameter ($d = \sqrt[3]{V_g}$ with V_g being the grain volume), assuming a dynamic viscosity of $\mu_l = 7.0 \times 10^{-3}$Pa · s [154], and neglecting solidification shrinkage and deformation (β_s=0, $\dot{\varepsilon}_{sv}$=0) was utilized. The secondary arm spacing was kept λ_2=20 µm. The boundary conditions were set as follows: a constant pressure on the top surface where the fluid is drawn in, *i.e.* $p_0 = 0$ Pa, a constant non-zero average flux on the bottom surface of -20 µm^3/µm^2 · s^{-1} and closed lateral boundaries, *i.e.* $q_l = 0$ µm^3/µm^2 · s^{-1}. Due to non-zero fluid flux on the bottom surface and closed lateral surfaces, downward flow inside the domain occurs, drawing fluid in from the top surface.

Fig. 5.7 shows pressure maps for three semisolids, each at $g_s = 0.60$, containing cubic equiaxed grains created under different cooling rates (1, 5, and 55 K/s). The results provide a general view of the pressure distribution and the different pressure drops resulting from different microstructures. The pressure is seen to decrease almost linearly from the top to the bottom, indicating that the further away from the top of the domain the lower pressure is. A significant pressure drop is observed with the high cooling rate of 55 K/s (Fig. 5.7(c)), achieving a local value of -986 Pa. This is an indication that a higher resistance of liquid is found when liquid going through an intra-dendritic network as compared to globular structure (Fig. 5.7(a)), where free fluid flow occurs only in the extra-dendritic zone. Between the two extreme cases, the presence

of the liquid in both extra-dendritic and intra-dendritic region leads to an intermediate pressure drop (Fig. 5.7(b)). Although it is unrealistic to assume a constant grain size (the same equivalent grain diameter) for different cooling rates, it has been done for the purpose of decoupling cooling rate and grain size effects as they relate to flow behaviour. As the fully solidified structure is generated using a Voronoi tessellation, the average grain size could easily be modified according to the cooling rate based on an empirical equation. Unfortunately, grain size measurement of primary delta grains are very challenging because of the δ to γ solid state phase transformation.

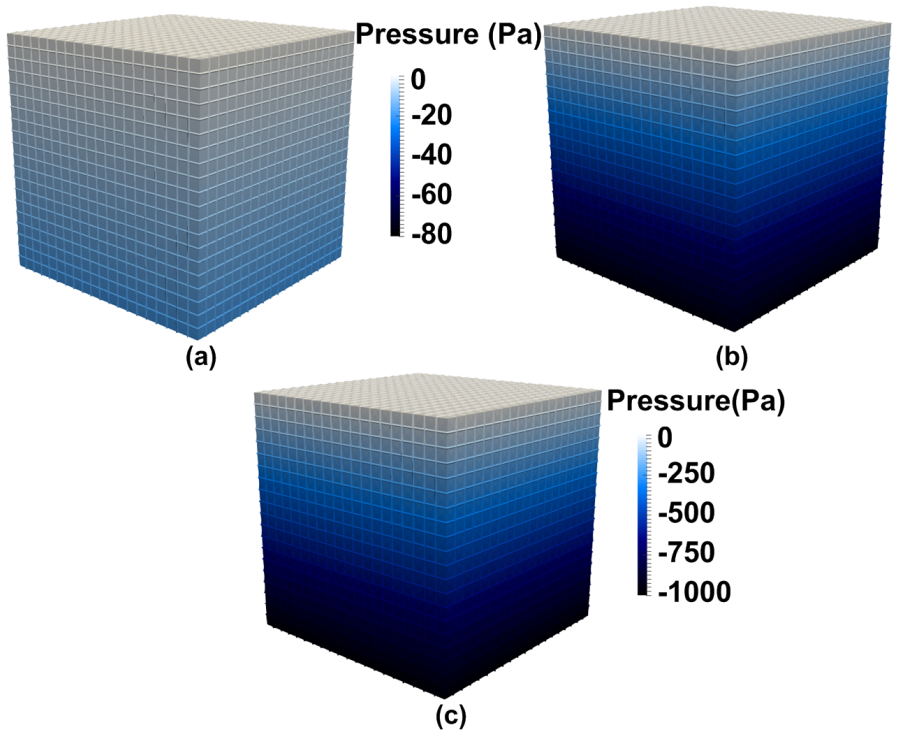

Figure 5.7: Pressure distribution within a domain containing 8000 grains at g_s=0.60 solidified under three cooling rates: (a) CR=1K/s, (b) CR=5K/s and (c) CR=55K/s. Note that Fig. 5.7(a) and (b) share the same color bar.

5.2.1 Permeability assessment

Limiting cases and transition tested

The dendritic fluid flow model can be verified by comparing its predictions of permeability against corresponding predictions from the analytical Carman-Kozeny equation[89, 155] for two scenarios: a dendritic structure with $S_v = \frac{2}{\lambda_2}$ [78] (termed Dendritic S_v) and a globular structure with S_v calculated as

the sum of the grain surface areas assuming globular structure divided by the volume of the whole domain [121] (termed Globular S_v). For these tests, a series of simulations were performed between $0.5 < g_s < 1$ under the conditions described previously using uniform cubic grains. The permeabilities predicted by the simulations can then be calculated from the average pressure difference between the top and bottom surfaces,

$$\kappa = \mu_l \frac{q_1}{\left(\frac{p_1 - p_0}{L_{dis}}\right)}, \tag{5.2.1}$$

where L_{dis} is the distance between the two surfaces, p_1 is the averaged pressure on the bottom side of the domain, and q_1 is the flux on the bottom surface. Note that as there is a single grain size and a uniform temperature applied to the entire domain, there can be no variation in the permeability between individual cubic grains.

Fig. 5.8 compares the permeability predicted by the 3D fluid flow model and the values calculated with the Carman-Kozeny equation utilizing the Dendritic S_v and the Globular S_v. As can be seen, an excellent match is achieved between the simulations with a cooling rate of 55 K/s (green diamonds) and the dendritic-flow analytical solution. In this scenario, $\vec{v}^{ed}$ is zero and the domain is a porous medium with a uniform $\vec{v}^{id}$ flowing through the intra-dendritic regions. Further, an excellent match is achieved between the simulations with a cooling rate of 1 K/s (red circles) and the globular-flow analytical solution. In this scenario, flow occurs only in the extra-dendritic regions.

The interesting result occurs for the permeabilities calculated from the simulation using a cooling rate of 5 K/s (blue triangles). As can be seen, there is a significant deviation between the model's predictions and the Carman-Kozeny equation using the two limiting values for S_v up to a solid fraction of ≈ 0.75. Initially, the dendrite envelope grows into the liquid and g_s' is relatively low (Fig. 5.6). Fluid thus flows through both the intra-dendritic and extra-dendritic regions, causing the permeability to fall between the dendritic and globular cases. As $g_s' \to 1$, flow becomes predominantly extra-dendritic and eventually the permeability follows the Carman-Kozeny equation derived based on the Globular S_v.

By testing the numerical results against an analytical equation, the present model is shown to be an alternative technique for obtaining the semisolid permeability. The calculated values could also be compared to experimental measurement using the given interfacial surface area concentration to provide additional insight.

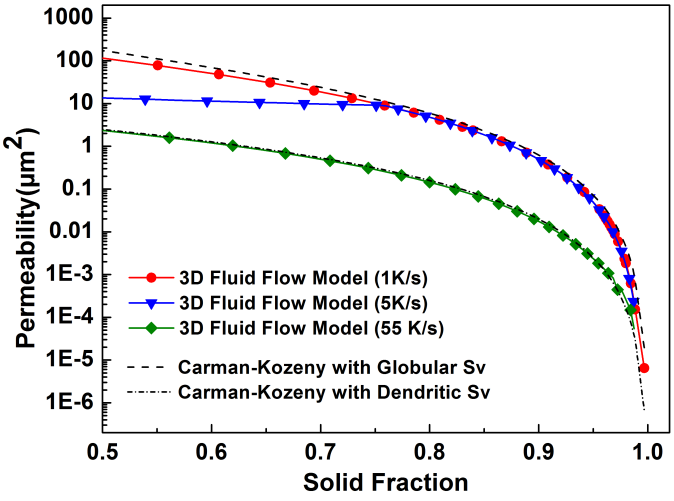

Figure 5.8: Validation of permeability predicted by present model with the Carman-Kozeny equation for a uniform network of grains with microstructure solidified under the cooling rate of 1K/s, 5K/s and 55K/s.

Influence of grain size on the permeability

The assumption made in Fig. 5.8 was of uniform grain size. However, this is not a realistic description of microstructure. Fig. 5.9(a) shows the relative frequency of grain size in a 3D domain created using the Voronoi tessellation for an average grain size of 300 µm. Fig. 5.9(b) shows the corresponding evolution in g_s' for five different grain sizes each solidified using a cooling rate of 5 K/s. As can be seen, for smaller grains (60 µm), g_s' quickly approaches 1 and thus forms a globular structure due to the constraints of solute enrichment in front of the solid/liquid interface, whereas for coarse grains (722 µm) the dendrite tip is free to move until impingement with neighbouring grains. Thus, at a specific time, which corresponds to a specific bulk solid fraction, fluid flow takes place in the extra-dendritic region for smaller realistic grains, passes through the intra-dendritic region for these grains which are impinging with their neighbours, and has mixed characteristics for grains at intermediate size levels.

Given the intrinsic variability in grain size, the permeability within a semisolid will be influenced by this quantity. Fig. 5.10 shows the permeability within a domain with 8000 grains, having an average grain size of 300 µm, predicted by the fluid flow model containing a mixture of both globular and dendritic grains of realistic geometry. It can be seen that at lower solid fraction, the permeability of the mushy zone neither follows the intra-dendritic flow behaviour (Carman-Kozeny with Dendritic S_v) nor the extra-dendritic

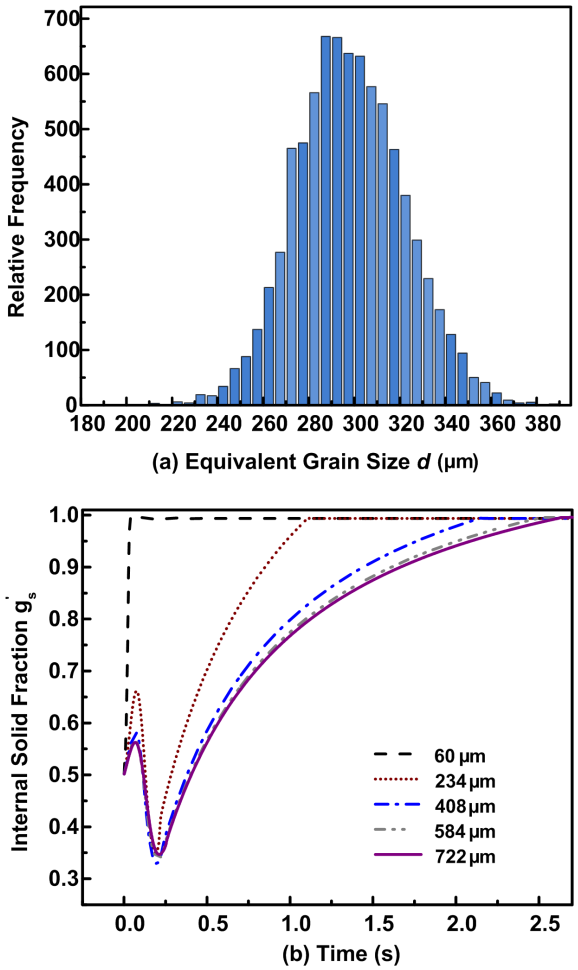

Figure 5.9: (a) Equivalent grain size d distribution within the semisolid domain and (b) the variation in g_s' for five grains containing different sizes.

flow behaviour (Carman-Kozeny with Globular S_v) but is a mixture of both. Eventually, the permeability approaches the Carman-Kozeny permeability for structure with Globular S_v. In this realistic case the Carman-Kozeny equation with Dendritic S_v does not provide a good analytical description of permeability until $g_s = 0.96$.

Permeability-microstructure map

Referring to Fig. 5.10, it can be seen that the semisolid permeability can only be predicted by the Carman-Kozeny equation with Dendritic S_v or Globular S_v over a small range of solid fraction; outside of this range there is a great deviation from either the dendritic or the globular cases. This deviation has not

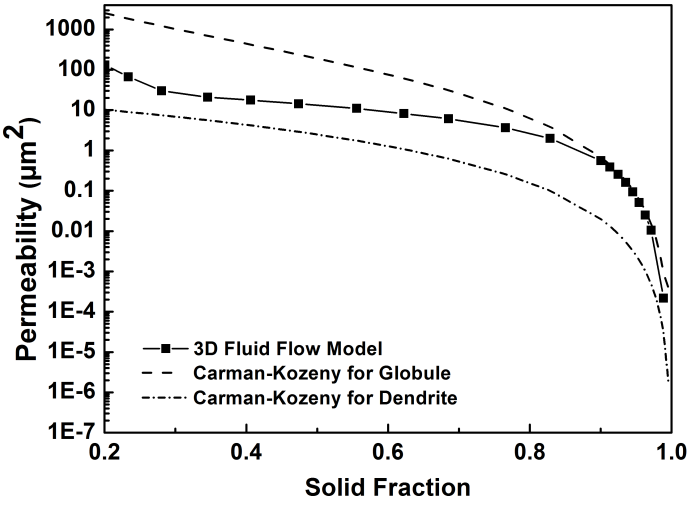

Figure 5.10: Variations of permeability as a function of solid fraction for a semisolid domain containing both intra-dendritic and extra-dendritic flow.

been identified before. In order to show the range of validity of the Carman-Kozeny equation using these two limiting cases in predicting the mushy zone permeabilities in metallic alloys, a series of quasi-steady flow simulations were performed, by varying the solid fraction (30 values), cooling rate (10 values assuming an average grain size of 300 μm and a secondary arm spacing of 20 μm), and grain size (10 different values assuming a cooling rate of 10 K/s), using a domain containing 8000 realistic grains with an average grain size of 300 μm, to provide over 600 unique permeability values. These simulations again neglected solidification shrinkage and deformation (β_s=0, $\dot{\varepsilon}_{sv}$=0).

Fig. 5.11 provides two permeability maps that show the range of solid fraction where the Carman-Kozeny equation with Dendritic S_v or Globular S_v is valid in predicting permeability; (a) as a function of cooling rate and (b) as a function of dimensionless grain size $d/(2 \cdot \lambda_2)$. Each map is divided into two shaded areas corresponding to Globular S_v and Dendritic S_v, and an unshaded area where neither expression matches the simulation result within the tolerance of 50%. Beginning with Fig. 5.11(a) it can be seen that under conditions of lower cooling rates the Carman-Kozeny equation with Globular S_v is most appropriate; the valid solid fraction range will decrease with increasing cooling rate and is no longer valid once the cooling rate exceeds 15 K/s. At high cooling rates especially greater than 10 K/s, the Carman-Kozeny equation with Dendritic S_v is most appropriate over a wide range of solid fraction. However, at low solid fraction there are no circumstances where the simulated

permeability matches the analytical expressions. Further, there is an important combination of cooling rate and solid fraction where neither analytical expression is valid, covering all solid fractions. Any macroscale model, having the same solidification conditions, and utilizing the Carman-Kozeny equation with one of these two limiting cases could show discrepancies as compared to experimental findings. Turning now to Fig. 5.11(b), it can be seen that the Carman-Kozeny equation with Dendritic S_v or Globular S_v is no longer valid when $d/(2 \cdot \lambda_2)$ is greater than 30 for the specific cooling rate of 10 K/s. At lower values of this dimensionless grain size the Carman-Kozeny expression for globular structures is found to be valid at very high solid fractions as the liquid is mostly dominated by the extra-dendritic flow whereas the Carman-Kozeny expression for dendritic structures is only valid over a very small range of parameters.

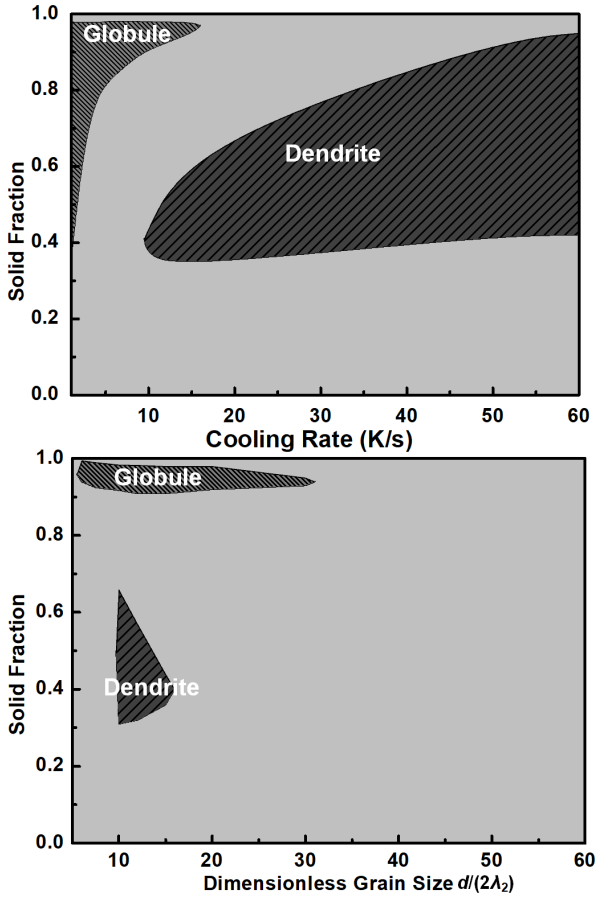

Figure 5.11: Permeability map as a function of solid fractions and (a) cooling rate as well as (b) dimensionless grain size, $d/(2 \cdot \lambda_2)$.

It is clear that from Figs. 5.9 to 5.11 that the permeability of a semisolid

domain containing a mixture of two morphologies cannot be predicted with the Carman-Kozeny equation via a single scaling law for S_v throughout the whole solid fraction range. This, as is commonly done in macrosegreation simulations, makes the permeability assessment less accurate. Utilizing our 3D equiaxed-dendritic meso-scale solidification model [156], it is possible to calculate S_v for a domain containing multiple morphologies as

$$S_v = \frac{\sum_{i=1}^{N_{elem}} S_{sl}^e}{V_{domain}}, \tag{5.2.2}$$

with $S_{sl}^e = \begin{cases} \frac{2}{\lambda_2} \cdot V_{env}, g_s' < g_{critical}' \\ \mathrm{S}_{globule}, g_s' \geq g_{critical}' \end{cases}$

where N_{elem} represents the total number of elements within the domain. S_{sl}^e represents the solid/liquid interfacial area of an individual element, V_{domain} is the total volume of the domain, V_{env} is the volume of the dendrite envelope and $S_{globule}$ is the surface area of globular element.

The key point in determining the S_v through our solidification model is identification of the internal solid fraction g_s' at which flow within an individual element is dominated by intra-dendritic or extra-dendritic character; if the g_s' is greater than critical point $g_{critical}'$ the element is treated to as globular and intra-dendritic liquid flow is ignored.

Fig. 5.12 plots the permeability calculated from the Carman-Kozeny equation utilizing the solidification model -calculated S_v for five different critical values of g_s' , as well as the prediction from the 3D fluid flow model. As can be seen, this approach to calculating S_v results in a clear transition zone in permeability from dendritic to globular character and matches much more closely to the model-predicted value than the Dendritic S_v and Globular S_v cases. However, deviations still exist and the importance of selecting the "right" value of g_s' is evident since a higher critical value of g_s' provides smaller deviation at higher solid fractions but then under-estimates the permeability at lower solid fraction. The determination of the critical point of g_s' requires further investigations both experimentally and numerically. The observed differences could also be due to limitations within the 3D fluid flow model, which is built on the following assumptions: a uniform porous medium within the dendrite envelope with locally $S_v = \frac{2}{\lambda_2}$ and Poiseuille flow when $g_s' \sim 0$. Another option for overcoming the limitations of using S_v calculated by λ_2 would be to use a general form that considers grain growth, coalescence and impingement [53].

Localization of liquid feeding

In a domain that contains different grain sizes, different semisolid morphologies are possible as shown in Fig. 5.9(b). Due to these different morphologies,

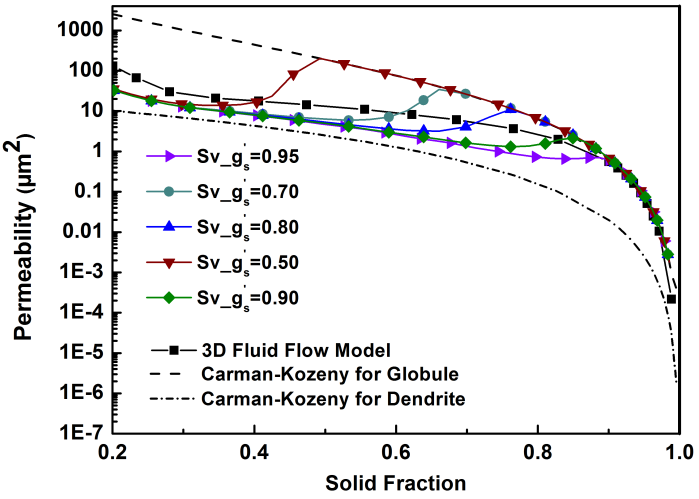

Figure 5.12: Influence of S_v calculated based on different internal solid fractions on the prediction of the permeability within mushy zone via Carman-Kozeny equation.

flow is likely to concentrate in areas with a higher local permeability. To reproduce the this feeding localization, a set of simulations were carried out by imposing a pressure difference between the top and bottom surfaces of the domain consisting of 8000 realistic grains, p_0=0 Pa and p_1=-2 MPa, while the lateral surfaces were closed, and solidification shrinkage and deformation were neglected (β_s=0, $\dot{\varepsilon}_{sv}$=0). These conditions provide uni-directional flow with the same flow rate of liquid entering and leaving the domain.

Fig. 5.13 shows the 3D permeability map and corresponding local fluid velocity resulting from these simulations at solid fractions of (a) 0.70 and (b) 0.84 to highlight the capability of the fluid flow model in predicting the localization of liquid feeding. First, by examining a-1, it can be seen that the permeability between different grains varies considerably, due to differences in g_s' and the extra-dendritic liquid channel width. The maximum local permeability at bulk $g_s = 0.7$ is 10730 μm^2; the value of 0 μm^2 represents grains that have fully solidified. As the permeability for globular structures is higher than dendritic structures at the same solid fraction (Fig. 5.10), this variation in local permeability would lead to further localization in liquid feeding. Second, by examining a-2, it can be seen that the fluid selectively flows through areas having larger local permeability, at higher local speeds. At higher solid fraction, $g_s = 0.84$ and shown in a-2, the maximum local permeability decreases to 4096 μm^2 due to the increase in g_s' and narrowing of the extra-dendritic liquid channels. The maximum liquid channel velocity, shown in b-2, consequently

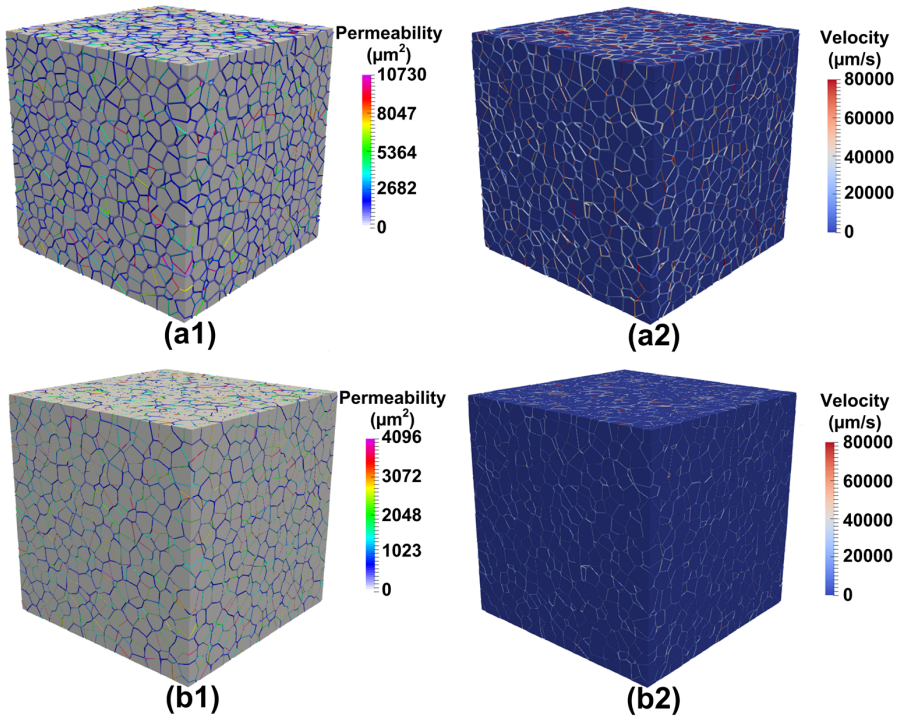

Figure 5.13: Variations in permeability (-1) and local velocity (-2) within a semisolid domain at (a)g_s=0.70 and (b) g_s=0.84. The grain size was 500 µm, and the cooling rate was 5 K/s

also decreases.

5.2.2 Fluid flow induced by phase changes and tensile deformation

The 3D dendritic fluid flow model can also be used to calculate the amount of liquid required to compensate phase changes and imposed tensile deformations under dendritic solidification conditions. This requires activation of the shrinkage and deformation terms of Eq. 4.1.25(*i.e.* $\beta_s \neq 0, \dot{\varepsilon}_{sv} \neq 0$ follow Eqs. 4.1.18 and 4.1.23) Four different compositions were assessed; Fe-0.07wt.%C, Fe-0.12wt.%C, Fe-0.16wt.%C and Fe-0.18wt.%C. The solidification simulations contained 8000 cubic grains, 500 µm in size, cooled at a rate of 55 K/s. The uniform selection of grain size (cubic grain) and the high cooling rate ensured the creation of a fully dendritic semisolid structure. For boundary conditions, the flow simulation assumed that all the domain surfaces except the one on the top were closed and a gauge pressure of 0 Pa, was imposed on the top surface. Hence, the liquid suction from top surface due to shrinkage and deformation can be predicted.

Fig. 5.14(a) shows the variation in net liquid flow per unit volume (Q/V) predicted by the 3D dendritic fluid flow model to compensate for solidification shrinkage in all four of the carbon compositions of interest assuming $\beta_s \neq 0$ and $\dot{\varepsilon}_{sv}$=0. First, as expected, it can be seen that although the predicted inflow of liquid decreases with increasing solid fraction, the net liquid flow is significantly different dependent on alloy composition. Interestingly, a sharp rise in net fluid flow is predicted to be needed to compensate for shrinkage in the peritecic alloys once the peritectic transformation starts to account for the additional density difference of the austenitic phase. The sharp rise occurs at a relatively low solid fraction for the hyper-peritectic alloy, followed by the peritectic and hypo-peritectic alloy at increasing g_s. The net fluid flow required then remains relatively constant until the final stages of solidification.

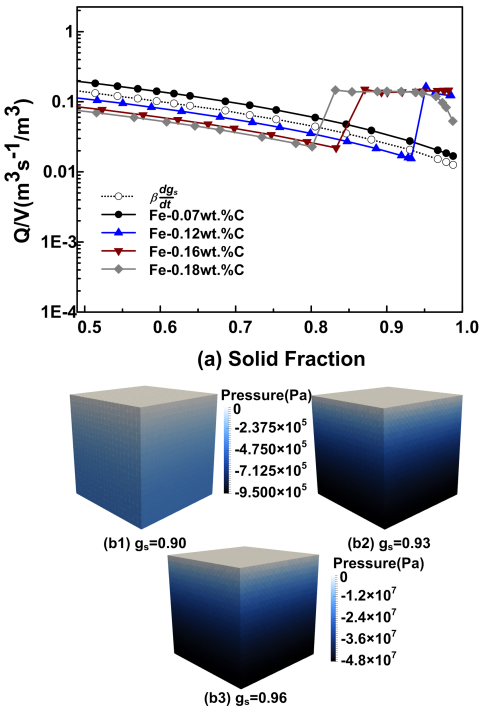

Figure 5.14: A comparison of Q/V predicted by the 3D dendritic fluid flow model and Eq. 5.2.3 as a function of solid fraction for various Fe-C alloys along with the pressure contours at three solid fractions for Fe-0.12wt.% alloy. The required flux to compensate for the peritectic transformation in peritectic grades is also included in the flow predictions of the 3D dendritic fluid flow model.Note that Fig. 5.14(b1) and (b2) share the same color bar.

For non-peritectic alloys, the amount of liquid required to compensate for

solidification shrinkage can also be calculated analytically as

$$\left(\frac{Q}{V}\right) = \beta_s \frac{dg_s}{dt}, \tag{5.2.3}$$

where Q and V represent the volumetric flow rate and total domain volume. For further validation purposes, the shrinkage calculated by this equation for a Fe-0.07wt.%C alloy is also shown in Fig. 5.14(a). As can be seen, a good match is obtained between the simulation and analytical curves.

Liquid feeding can be also induced by the deformation of the mushy zone. If, concurrently, semisolid tensile deformation is too large and liquid feeding is too low, a hot tear will form. Generally, the amount of net inflow of liquid required during solidification is a given by the combination of shrinkage and deformation. In order to investigate the dominant factors that cause hot tearing in hypo-peritectic grades (Fe-0.12wt.%C), known to be most-sensitive to hot tearing [55], a series of simulations were performed that consider both shrinkage and deformation ($\beta_s \neq 0$ and $\dot{\varepsilon}_{sv} \neq 0$); the same boundary conditions as for Fig. 5.14 were utilized.

Fig. 5.15 shows the net flow caused by the combination of solidification shrinkage and deformation, and their contributions under two different strain rates of 0.1 s^{-1} and 0.001 s^{-1}. Under the strain rate of 0.1 s^{-1}, the induced liquid feeding mainly comes from deformation at lower solid fractions($<$0.92), and amount of liquid required would increase when the peritectic tranformation occurs mentioned in the prior section. The dominant factor near the end of solidification would due to the large amount of shrinkage caused by the peritectic transformation.

Under small strain rate of 0.001 s^{-1} also shown in Fig 5.15(lower), clearly, lower strain rates result in a less liquid flow to counteract deformation. The net flow caused by shrinkage and deformation is dominated by the solidification shrinkage. In the industrial process, the strain rates during casting of steel are thought to be relatively small, on the order of 10^{-3}~10^{-4} s^{-1}. The results shown in Fig. 5.15 then seem to indicate that shrinkage associated with the large interfacial area of the dendritic structure is the key factor to cause defects.

5.2.3 Defect sensitivity analysis

The amount of liquid required during solidification and peritectic transformation can be linked to the formation of casting defects. Liquid flow that is inadequate to compensate for the solidification shrinkage could result in the formation of large voids to maintain continuity. At low solid fraction, a high permeability likely allows for adequate liquid feeding to heal any formed defects. At high solid fraction, Fig. 5.14(a) shows that for the hyper-peritectic

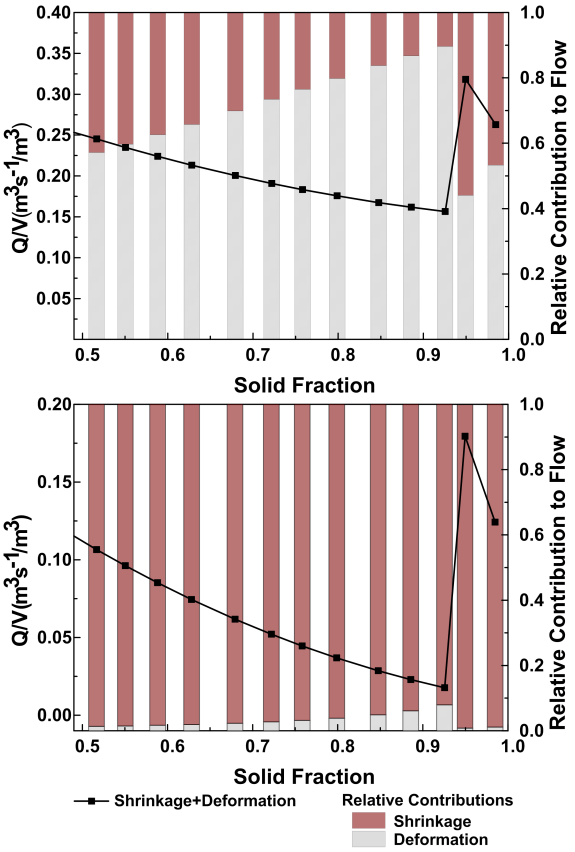

Figure 5.15: A comparison of the Q/V predicted by the 3D dendritic fluid flow model taking into account both solidification shrinkage and deformation. Strain rates of 0.1 s^{-1} (upper) and 0.001 s^{-1} (lower) are examined.

alloy, the jump in fluid required due to the peritectic transformation occurs at a "low-enough" solid fraction where the permeability remains relatively high. Using the same argument, defects would be most prone to occur in the hypo-peritectic alloy (Fe-0.12wt.%C) since the peritectic transformation occurs at a very high solid fraction where the permeability is quite low (Fig. 5.14(a)). Pressure contours of hypo-peritectic alloy are also plotted for different solid fractions to emphasis the influence of peritectic transformation shown in Fig. 5.14(b). It can be seen that before peritectic transformation, an increase in solid fraction would result in a minor increase in the pressure drop by comparing Fig. 5.14(b1) and (b2), while a significant pressure drop occurs after the peritectic transformation as shown in Fig. 5.14(b3) which is two orders of magnitude greater than Fig. 5.14(b1) and (b2). The high pressure drop near the end of solidification accelerates the formation of defects in hypo-peritectic alloy, and similar conclusion has been reported in the prior work as well [55].

5.3 Semisolid cracking model

The simulations presented in this section focus on the prediction of hot tearing within a semi-solid steel using the semisolid deformation model and cracking model mentioned in Section 4.1.4 and Section 4.2.1. In order to accurately reproduce the semisolid behavior in response to deformation, a domain with a minimum of 700 grains needs to be created, as identified by Sistaninia et al. [1]. In this investigation, a semisolid domain containing 1728 grains with an average grain size of 100 µm is selected. Temperature is assumed to be uniform within the semisolid domain, with a length along x, y, z direction defined as L_x, L_y and L_z.

The boundary conditions used for the semisolid deformation analysis are shown in Fig 5.16: symmetry boundary conditions are applied to x=0, y=0 and z=0, while surfaces y=L_y and z=L_z are free to move. A reference node is attached to the surface x=L_x, which allows for imposing a constant strain rate or displacement and directly obtaining the force-displacement curve. For the fluid flow calculation, two kinds of boundary conditions are used in this investigation. The first type is applied to study the pressure drop within a feedable mushy zone under tensile deformation, and all the surfaces are closed except surface x=L_x. Liquid metal will flow from surface x=L_x to compensate the semi-solid domain under tensile deformation. The second type represents that all the surfaces are closed for the prediction of semisolid deformation within an unfeedable mushy zone. This corresponds to a tensile experimental test where the specimen is isolated from any liquid feeding. The liquid is assumed to be compressible and the bulk modulus of liquid steel is assumed to be 55 GPa [157]. In the deformation analysis, the elastic module and

Poisson's ration used in this investigation are 15 GPa and 0.3 [158]. Note that coalescence and corner rounding are all considered in this section.

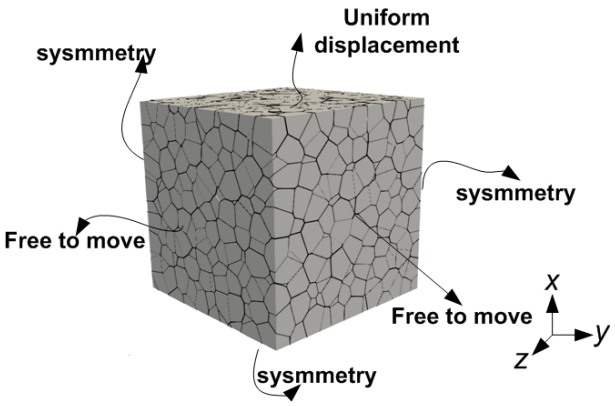

Figure 5.16: Schematic diagram of boundary conditions imposed in the semi-solid domain for stress calculation.

In this section, the semisolid deformation model is used to investigate the mechanical behavior of a feedable mushy zone. Subsequently, semisolid cracking model is applied to predict the cracking initiation and propagation of an unfeedable mushy zone, and the ultimate tensile strength predicted at different solid fractions are compared with the experimental measurements conducted by Seol et al. [27]. Then, the influence of the coalescence criterion on the bridging behavior within the semisolid is discussed, followed by the hot tearing sensitivity analysis performed on the semisolid steel containing different sulfur and oxygen contents.

5.3.1 Semisolid deformation of feedable mushy zone

In order to investigate the mechanical behavior of semisolid steels under a feedable condition, a series of simulations were performed on different grades (non-peritectic and hyper-peritectic alloy) at a solid fraction of 0.90 using the parameters listed in Table 5.1 using the semisolid deformation model. The semisolid geometry used in the simulation was created via the dendritic solidification model under the cooling rate of 1K/s. The Robin boundary condition was used in the surface x=L_x,

$$q_l = f_l \left(p_l - p_m \right), \tag{5.3.1}$$

where q_l represents the intrinsic liquid velocity, p_m is the metallostatic pressure and f_l is the feeding coefficient. In this simulation, the feeding coefficient and strain rate were kept as 0.02 µm $Pa^{-1}s^{-1}$ and 0.001 s^{-1}, respectively. The

temperatures of the semisolid with a solid fraction of 0.90 of non-peritectic (Fe-0.07wt.%C) and hyper-peritectic (Fe-0.18wt.%C) were 1517 °C and 1492°C, respectively. Non-peritectic alloy contains pure δ phase and hyper-peritectic alloy consists of 0.34 proportion of δ phase and 0.56 proportion of γ. Note that the influence of temperature on the constitutive behavior is assumed to be negligible.

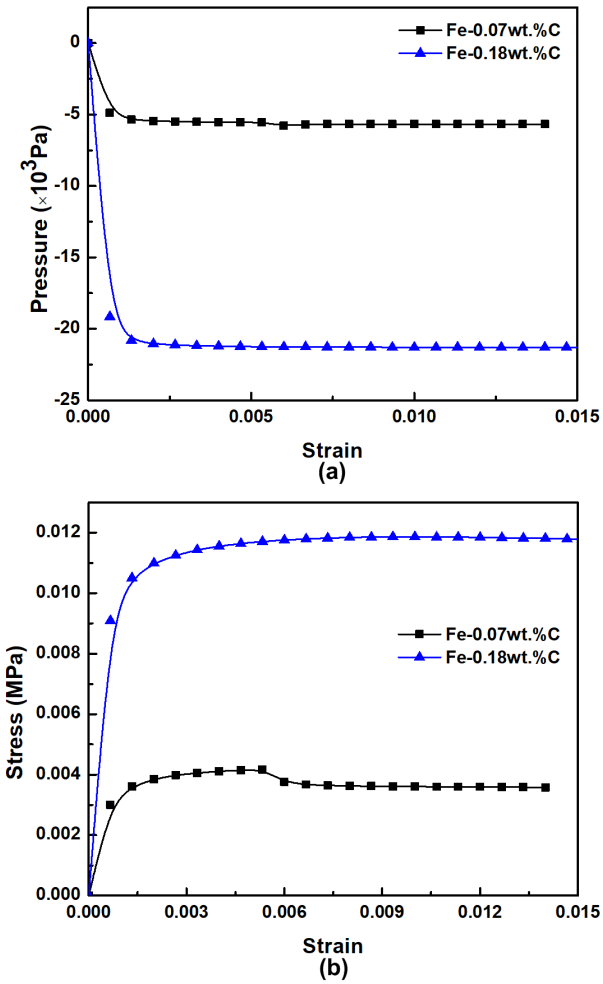

Figure 5.17: Predicted semisolid behavior with a solid fraction of 0.90 under a constant tensile deformation for non-peritectic and hyper-peritectic alloys: (a) liquid pressure and (b) average stress as a function of strain.

The pressure drop and the average stress of the semisolid resulting from a tensile deformation with various carbon contents are shown in Fig. 5.17. In Fig. 5.17(a), the results indicate that during the initial deformation, the pressure drop increases with the increase of strain, and remains almost constant even the domain is under tension. It can also be seen that under the same

feeding coefficient, a higher pressure drop is observed in the hyper-peritectic alloy compared with non-peritectic alloy. It can be expected that even though the solid fraction for all semisolids are the same, the proportion of the δ and γ phases is different for different initial carbon contents. The shrinkage coefficient resulting from the density and phase proportion greatly influences the fluid flow inside the domain, and hyper-peritectic alloy is associated with the peritectic transformation which in turn causes a larger pressure drop. The average stresses calculated for the two alloys are also plotted in Fig. 5.17(b). The average flow stress for the hyper-peritectic grade is higher than the non-peritectic grade at the given strain. As the deformation proceeds, the result of non-peritectic grade containing only δ phase shows no strain hardening, while the average stress of hyper-peritectic grade displays a higher value with strain hardening. The difference between the average stress predicted from non-peritectic and hyper-peritectic grades becomes larger as the tensile deformation continues at initial stage and then remains almost constant at larger strain.

5.3.2 Semisolid deformation of unfeedable mushy zone

During the semisolid tensile test, the specimen is isolated from the liquid feeding. This scenario is known to be unfeedable, and results in the formation of hot tearing. These hot tears initiate near the surface and grow towards the center. In this section, an extensive validation of the semisolid cracking model is achieved by comparing the predicted results with the measurements from the semisolid tensile test conducted by Seol et al. [27] presented in Section 4.3.1. The same steel grades and cooling conditions in Section 4.3.1 were used in the simulation. The second type boundary conditions were utilized in the unfeedable simulation where all the surfaces of the domain are closed. The $\lambda\cos\Theta$ in Eq. 4.2.4 is fixed to 2.288 N/m for the surface elements and 1.636 N/m for internal channels, which allows for the prediction of crack initiation and propagation.

Prediction of hot tearing initiation

Fig. 5.18(a) shows the predicted pressure drop in the liquid channel and the failure pressure, $p^c_{l,\max}$, calculated based on Eq. 4.2.4 for the widest liquid channel, for a semisolid at the solid fraction of 0.90 under the tensile strain rate of 0.01 s^{-1}. As the strain increases, the widest liquid channel widens during the tensile formation and the failure pressure required to overcome the capillary forces at the liquid-atmosphere interface increase. Fig. 5.18(a) also indicates the pressure drop inside the liquid channels, and the pressure drops initially with the increase of the tensile strain.

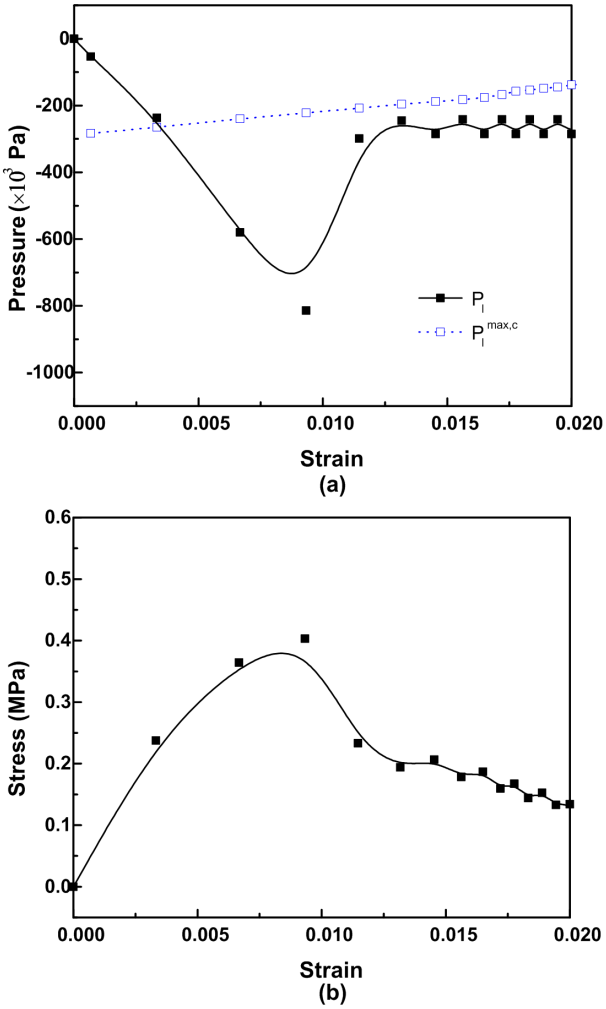

Figure 5.18: Simulated (a) liquid pressure and (b) stress as a function of strain for a semisolid at g_s=0.90 under the tensile strain rate of 0.01 s^{-1}.

The crack initiation can be predicted by referring to the intersection point in Fig. 5.18(a), where the failure pressure in the widest liquid channel exceeds the liquid pressure at the approximated strain of 0.003. Pressure inside the liquid continues to decrease with the increase of strain given the presence of hot tearing initiation. The initiated hot tear on the surface progressively grows towards the channels connected to it. A sudden pressure rise is also found at the strain of 0.008, which corresponds to the ultimate tensile strength. The can be explained by the fact that the amount of liquid sucked into other regions increases during crack propagation, and the pressure will increase once the increment rate of the sucked liquid exceeds the tensile strain rate. The sucked liquid at this moment is adequate for compensating the deformation and leads to the sudden rise in liquid pressure, which is also identified as a pressure drop relaxation by Sistaninia et al. [1].

Interestingly, the average stress shown in Fig 5.18(b) also keeps increasing with the increase of strain but with a smaller rate prior to the tensile strength which is defined as the maximum stress value on the stress and strain curve. There is clearly a drop in the stress after the tensile strength point due to the presence of cracking.

Comparison with experimental data

The comparison between the simulated tensile strength and the measurements [27] as a function of solid fraction is shown in Fig. 5.19. Both results have indicated that the tensile strength increases with the increase of solid fraction as more solid dendrites coalesce to form a compact solid network to withstand deformation. It can be seen that the fits at different solid fractions are excellent, i.e. specifically, at the solid fraction of 0.72 and 0.90 belonging to the regime of primary solidification. Thus, the tensile strength is shown to be predictable using the current semisolid cracking model. The value of the measured tensile strength is shown to be larger than the predicted value at the solid fraction greater than 0.95. It would then be expected that there were more bridging occurring within the experimental sample at the same solid fraction, and ultimately resulting in a higher strength.

Influence of coalescence criterion

As mentioned in Section 2.1.2, dendrite arms coalescence or bridging can transform continuous liquid films into isolated pockets that are able to withstand large deformation. Between two dendrite arms, a coalescence undercooling needs to be overcame as mentioned in Section 4.1.2. The coalescence undercooling determines the forces between two grains into three cases: attractive ($\gamma_{gb} < 2\gamma_{sl}$), neutral ($\gamma_{gb} = 2\gamma_{sl}$), and repulsive ($\gamma_{gb} > 2\gamma_{sl}$), mainly depending on the grain boundary energy. In this section, the effect of changing grain

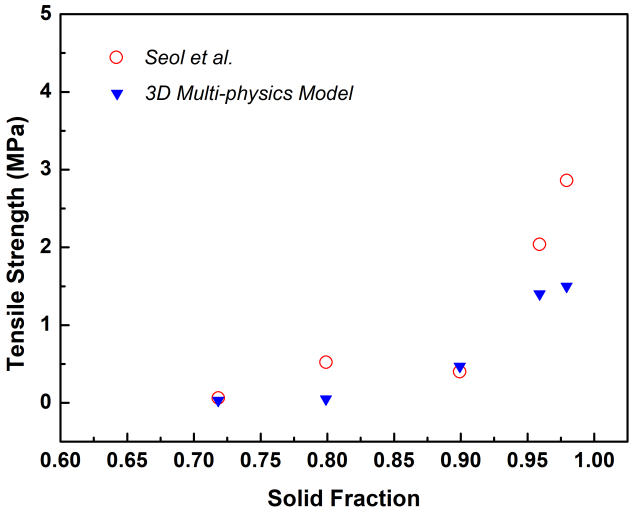

Figure 5.19: Comparison between the tensile strength measured in the steel samples by Seol et al. [27] and the results of the semisolid cracking model.

boundary energy, resulting in a coalescence undercooling distribution with the appropriations of attractiveness: 0.8%, 5% and 15.4%, respectively, is investigated. The greater the proportion of the attractive case, the easier for the dendrite to coalesce at a given solid fraction.

Fig. 5.20 shows the predicted stress vs. strain curve for three cases with different proportion of attractive cases at a solid fraction of 0.90. Clearly, the average stress of the semi-solid domain will initially increase with the increase of strain, followed by the decrease due to the presence of failure formation. The results also indicate that the case with a higher proportion of attractiveness is shown to have a higher strength compared with a lower proportion of attractive grains. It would be expected that there are more residual liquid remaining between the grains within the semisolid having less proportion of attractive grains. The remaining liquid will dramatically reduce the mechanical properties of the semisolid. The stress distribution within the semisolid under two cases are also shown in Fig. 5.21. It is easy to identify that stress is likely to be transmitted by the coalescenced grains as the solid bridges formed between the grains are able to withstand deformation. As shown in Fig. 5.21, more percolated grains are found in the case with 15.4% attractive grains, and the semisolid with more bridging inside are less prone to cracking.

Influence of surface tension

The surface tension of the liquid iron is influenced by an addition of sulfur and oxygen, and can be calculated analytically via Eq. 4.2.6 and Eq. 4.2.5,

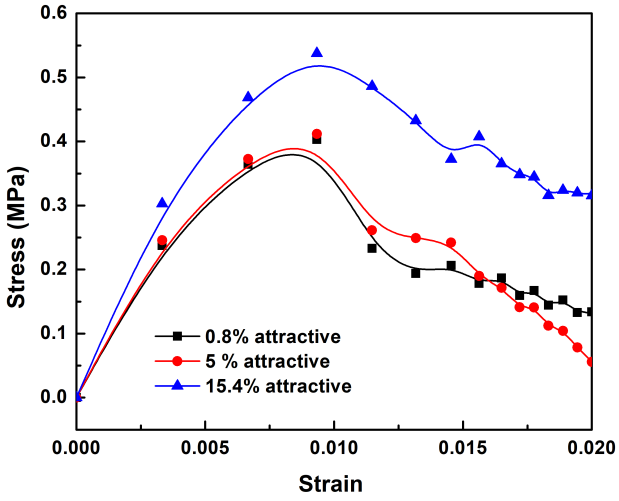

Figure 5.20: Comparison between average stress as a function of strain for various coalescence criteria.

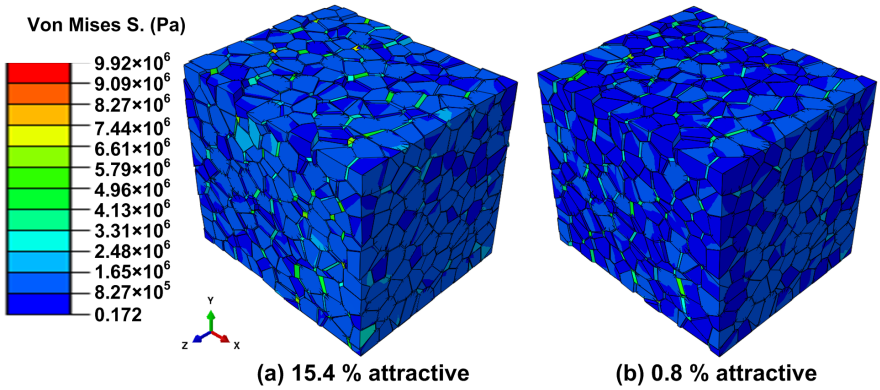

Figure 5.21: Contours plots of the Von Mises stress at a given strain of 0.003 predicted by using different coalescence criteria with attractive proportion of (a) 15.4% and (b) 0.8%, respectively.

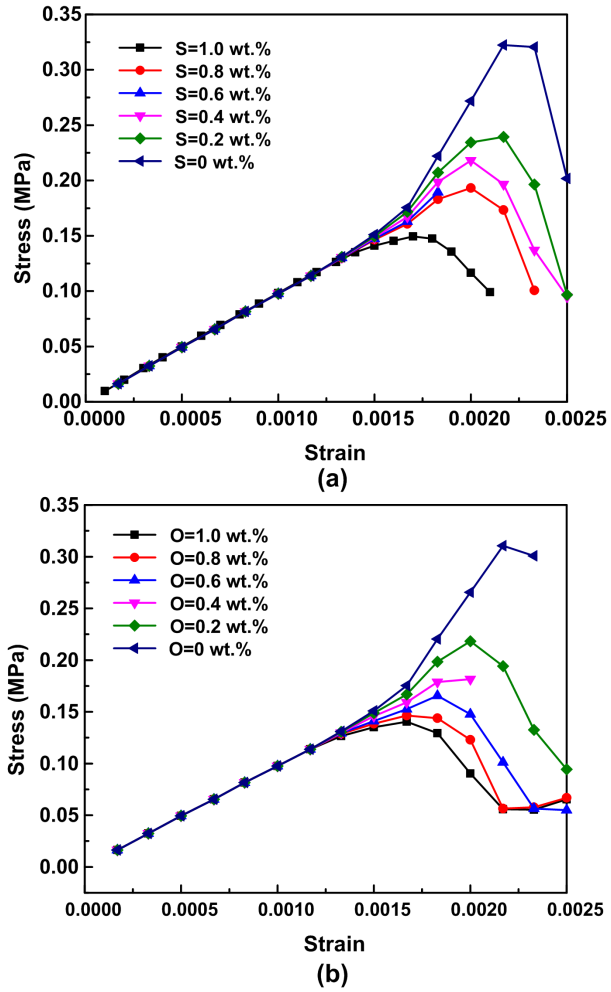

Figure 5.22: Influence of surface tension on stress strain curve of a semisolid at g_s=0.90 due to the presence of sulfur and oxygen.

respectively. The presence of sulfur and oxygen will decrease the surface tension as shown in Fig. 4.11. From a qualitative perspective, Fig. 5.22 shows a plot of stress against the strain at the strain rate of 0.005 s^{-1}, where the sulfur contents ranging from 0 to 1.0wt.% corresponds to the surface tension from 2.288 to 1.71 N/m. The carbon composition was kept the same as in Table 4.2 but the microstructure was formed under a faster cooling rate of 50 K/s.

Fig. 5.22(a) also shows a typical stress and strain evolution under tension for a semisolid containing different sulfur contents. Comparing the results, it can be seen that with an increase of sulfur contents, the tensile strength would decrease. This can be easily explained by the fact that the liquid film within the semisolid is easy to rupture due to the reduced value in surface tension. Note that the influence by the sulfur content on the solidification behavior was ignored in the simulation. Fig. 5.22(a) demonstrates that steel with high contents of sulfur strongly decrease the semisolid strength to withstand deformation and is more prone to the occurrence of hot tearing. Similarly, the presence of oxygen is also known to increase the sensitivity of hot tearing, as illustrated in Fig. 5.22(b).

5.4 Mesoscale solute transportation model

The models described in Section 4.2.2 provide a general approach to investigate solute transport within a semi-solid material at the mesoscale. In this section, the application of this 3D mesoscale solute transport models is used to predict centreline segregation during continuous casting of an advanced high strength steel with composition 0.1C-1.55Mn (wt.%) and other additions of Mo, Cr, Si, and Cu is presented. The underlying assumptions are as follows: (1) solute concentration is well mixed in the liquid pool; (2) solute concentration in the solid zone remains the same as the solute concentration at the interface between mushy zone and solid zone; (3) macro and micro segregation occur simultaneous within the mushy zone.

5.4.1 Creation of the model domain

The model domain consists of the entire mushy zone at the centreline of the slab from the liquidus to solidus temperatures. It contains both intra-dendritic liquid that is free to flow and stationary solid grains. The mushy zone length L_m, cooling rate $\dot{T}$, and average grain size near the centreline are determined by the characteristics of the casting machine and the secondary cooling systems including the amount and quality of the cooling water, as well as the casting speed.

Fig. 5.23(a) shows the evolution in centreline temperature as a function of distance below the meniscus as predicted by a 1D continuum-level model

known as CON1D [159] that simulates heat transfer and solidification during continuous casting. The CON1D model, calibrated against thermocouple data from the No. 2 continuous caster at ArcelorMittal Dofasco in Hamilton, Canada, is used in this study to determine L_m and $\dot{T}$. As can be seen in the figure, $L_m \approx 2700$ m for the given casting conditions while $\dot{T}_{avg}$ was found to be ≈ 0.14°C/s. The average grain size near the centreline, ≈800 µm, was obtained from metallography measurements made on a section of the fully solidified slab.

Fig. 5.23(b) shows lines of constant solid fraction at $g_s = 0$ and $g_s = 1$ as a function of distance along the entire caster to denote the extent of the mushy zone as well as the shell thickness. The location of the mesoscale domain relative to the slab is clearly seen by this figure, and represents the final stages of solidification. Specifically, the domain has dimensions of 2700 mm in z (*i.e.* L_m) by 20 mm in x and 20 mm in y about the centreline of the casting where z, y and x denoting the casting direction, thickness direction and width direction respectively. Due to symmetry, only one-half of the thickness is shown. Finally, Fig. 5.23(c) shows the corresponding variation in g_s, throughout the mushy zone at the centreline (P_i) and 10 mm from the centreline in y (P_{ii} *i.e.* the surface of the mesoscale model in the thickness direction). g_s curves from both the CON1D simulation as well as the average g_s values used in each subdomain of the mesoscale simulation. The concept of the subdomains is further discussed below. Note that P_{ii} is initially at $g_s > 0$ since the interest is in studying centreline solidification. Thus, P_{ii} is also seen to solidify before P_i.

5.4.2 Boundary conditions

Fig. 5.24 illustrates the boundary conditions used to solve the fluid flow and solute distribution equations. The extent of the mushy zone can be easily identified by the location of the $g_s = 0$ (blue) and $g_s = 1$ (green) lines in the middle image corresponding to similar lines shown in Fig. 5.23(b). The boundary conditions, shown in the upper image, need to be applied to all six surfaces of the simulation domain: a vertical inlet plane (on the left) which is adjacent to the molten liquid, four lateral surfaces, and a vertical outlet plane (on the right) separating the mushy zone from the fully solidified metal. They can be summarized as follows. A Dirichlet condition *i.e.* a constant pressure p_1, consisting of both metallostatic and atmosphere pressure and a constant solute concentration in liquid phase at the liquidus temperature matching the alloy composition, c_1 is imposed on the inlet plane. Homogeneous Neumann conditions are applied on the four lateral surfaces as lateral feeding is negligible and thus mass flux and solute flux are assumed to be zero. A Homogeneous Neumann condition is also imposed on the outlet plane since mass and solute

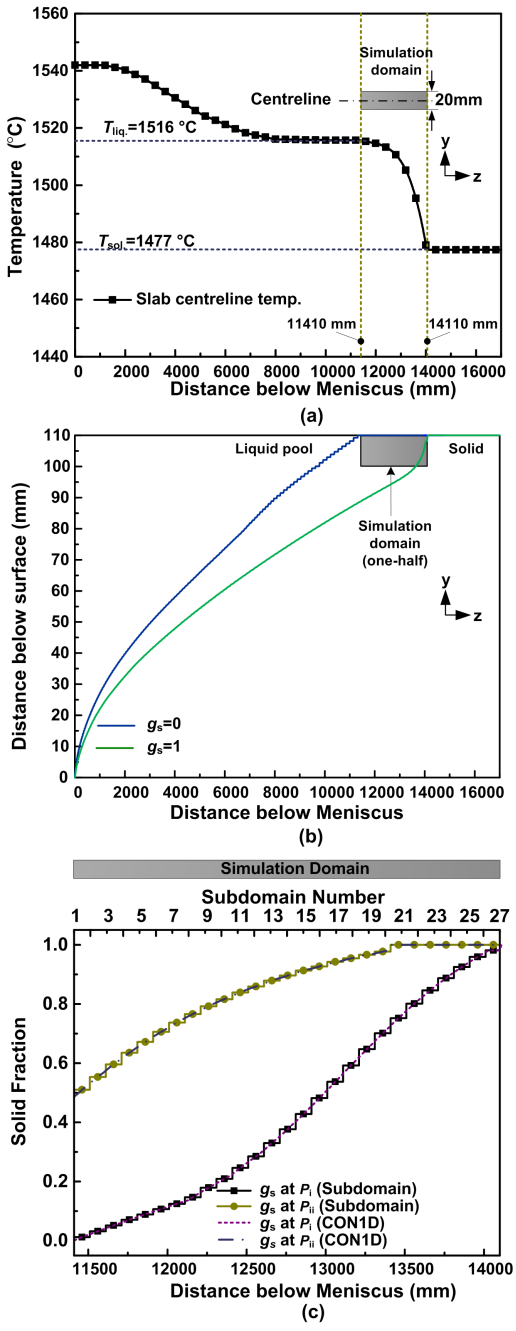

Figure 5.23: (a) Temperature evolution along the centreline predicted by CON1D along with a schematic diagram of simulation domain location; (b) corresponding lines of $g_s = 0$ and $g_s = 1$ to denote the extent of the mushy zone; (c) solid fraction variations at positions P_i and P_{ii} within the mesoscale simulation domain, along with a schematic of the applied subdivision used to reduce computation time. Note that the solid fraction is a sum of both delta phase and austenite phase.

flux cannot flow through the solidified boundary.

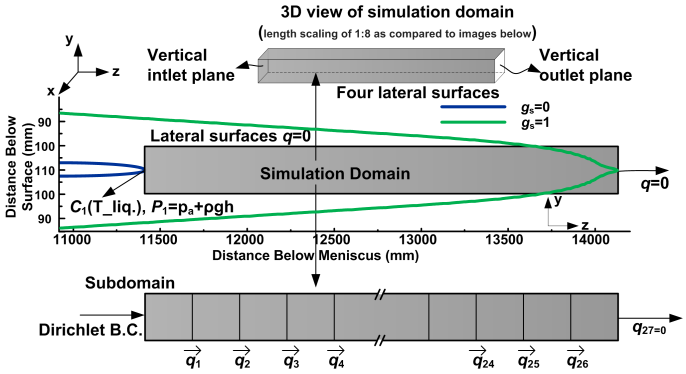

Figure 5.24: Boundary conditions applied for the simulation domain with a size of 2700 mm × 20 mm × 20 mm identified by the liquidus and solidus lines (above) and (b) the mass and solute flux at the subdomain interface within the simulation domain.

5.4.3 Numerical implementation

Fig. 5.25 provides an illustration of the simulation procedure applied to calculate the solute distribution within the liquid throughout the mushy zone. First, the CON1D model is run to acquire the thermal history of the slab during continuous casting, providing the required details to create the mesoscale model domain. Second, from the CON1D data and measured grain size, the 3D mesoscale dendritic solidification model is applied to create the 3D semi-solid geometry containing δ, γ and liquid phases at different locations of the mushy zone. Third, the 3D mesoscale dendritic fluid flow model is applied to calculate the pressure distribution throughout the mushy zone, and thus to determine the average fluid velocity within each element. Finally, the 3D mesoscale solute transport model is applied to acquire the solute distribution within the semi-solid's liquid channels.

With reference to the solidification model, a simple binary Fe-C aloy with nominal composition $C_0 = 0.105$ wt.% is assumed in order to create the semisolid structure at a specific solid fraction using the volume average approach. This simplification is justified by the fact that carbon has the dominant effect on the solidification interval and on the liquid density variations [160]. Fig. 5.26 compares the equilibrium Fe-C phase diagram with a pseudo-binary phase diagram whereby Mn has been added as a third element. As can be seen, while the introduction of Mn shifts the phase boundary downward and to the left, the shape remains the same. Although the use of an Fe-C binary phase diagram also changes the liquidus and solidus temperatures, this

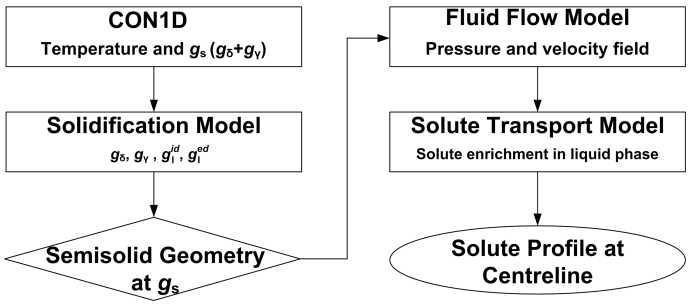

Figure 5.25: Flow chart outlining the sequential one-way coupling process for the solute prediction and validation within the continuous casting process at a steady state.

discrepancy should not be overemphasized as the focus of the mesoscale solidification model is to reproduce the semisolid geometry at a specific solid fraction. With reference to the solute distribution model, the equilibrium solute concentration $\bar{c}_l$ in Eq. 4.2.12 is taken to be the value obtained from the Fe-0.105wt.%C-1.55wt.%Mn ternary system at the equivalent solid fraction.

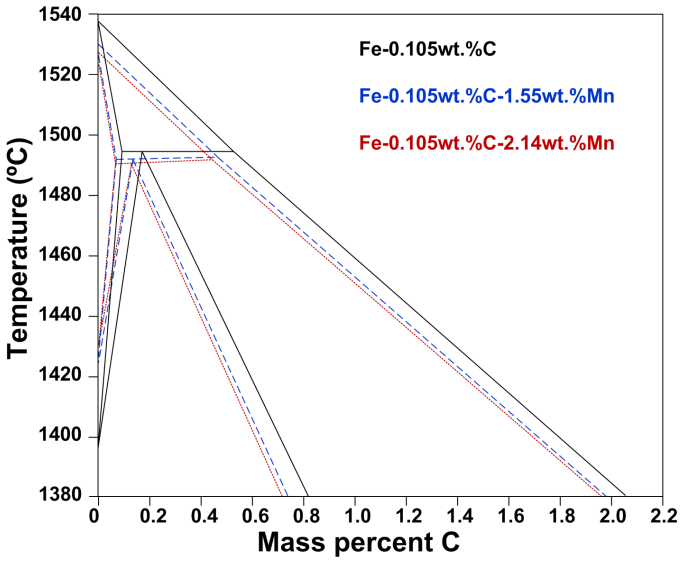

Figure 5.26: Linear approximation of the binary Fe-C equilibrium phase diagram, along with the corresponding Fe-C-Mn pseudo-binary phase diagram at 1.55 and 2.14 wt.%Mn.

The heavy computational cost associated with the calculation of such a large mushy zone, 2700 mm in length can be overcome by partitioning the domain following a method similar to the simultaneous use of multiple processors. As shown in Fig. 5.24, the domain is subdivided into 27 smaller domains each 100 mm in length and known as subdomains. g_s is assumed to remain constant

along z and x, but varies in y within each subdomain according to P_i and P_{ii} of Fig. 5.23(c). Mass flux and solute flux are exchanged at the boundaries between the subdomains as a result of fluid flow and diffusion [161].

A two-step simulation is performed to determine the unknown net mass flux q between each subdomain of the simulation, neglecting the influence of casting speed on the net mass flux. Initially, the simulation starts with the last subdomain, No. 27 with a known flux (q_{27}=0 µm·s^{-1}) on the right end as indicated in Fig. 5.24. As the lateral surfaces are closed, the flux q_{26} can be calculated simply by imposing any constant pressure on the left of subdomain 27. This is because q_{26} depends only on the pressure gradient, not the actual value of imposed pressure. In the calculation, $p = 0$ Pa is chosen. Once q_{26} is obtained, a similar step can be applied for subdomain 26 with the known q_{26} from subdomain 27 utilized to calculate q_{25}. After 27 simulations, q_1 between subdomains 1 and 2 is obtained.

In the second half of the simulation, the computation begins first with subdomain 1 assuming known boundary conditions (pressure p_1 and uniform solute concentration c_1) on the left side, known q_1 on the right side, and closed lateral surfaces, in order to obtain the pressure and solute distributions within subdomain 1 as well as p_2 and solute concentration at the interface between subdomains 1 and 2. This process continues until the pressure and solute concentrations in subdomains 27 are determined.

It was observed that very small velocity components were sometimes obtained at the lateral boundaries, which slightly different from the imposed values of zero flux. This was thought to be a result of discretization error and was handled by forcing the components at the boundaries to be equal to the imposed values prior to simulating solute transport.

Computational expenses and central processing unit (CPU) time for simulations are among the main concerns limiting use of numerical models, especially continuous casting macrosegregation models [162]. One of the advantages of the present mesoscale model is its effective computational performance. The simulation time for each subdomain containing 40000 grains was ≈15 min on a Linux machine with a 3.00 GHz 2-core processor. This is far shorter than continuum methods where multiple days are generally required to achieve similar results.

5.4.4 Centreline segregation

To accurately predict the solute distribution within a mesoscale semi-solid domain, various phenomena have to be considered. In the following sections, a series of simulations are performed to demonstrate the model's ability in predicting solute localization and macrosegregation. The model's results are independent of the solid phase and only focuses on the solute redistribution

within the liquid channels. Additional to the solute partitioning between solid and liquid phase, macrosegregation is dominated by the fluid flow behaviour. First, some results showing the variation in the pressure field and velocity along the liquid channels at steady state within a semisolid containing different grain sizes are presented. Then, the solute flow predictions and centreline segregation during continuous casting are examined, and compare the results to experimental data. Finally, the model is applied to investigate the influence of mechanical deformation and alloy composition on solute distribution.

Grain sensitivity analysis

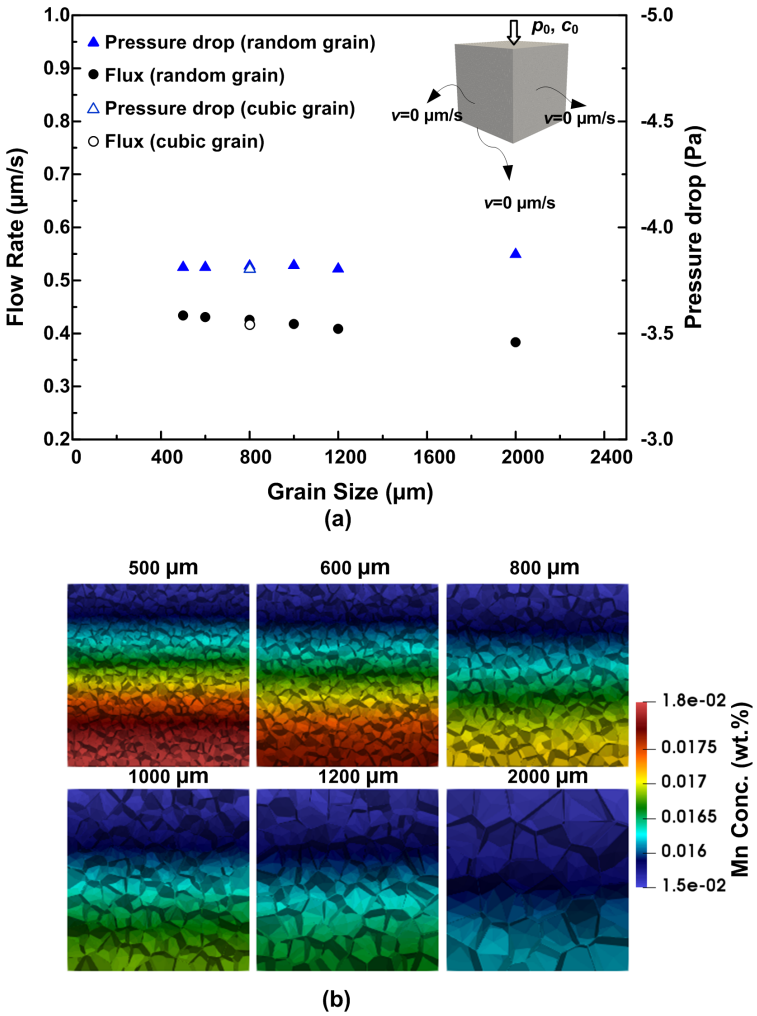

Figure 5.27: (a) Influence of grain size on the flow rate and pressure drop assuming g_s=0.92; (b) corresponding solute maps for each of the six cases.

The base case simulation is the similar as the one reported in Ref. [147], but solute redistribution is included. Specifically, the mesoscale solute transport model was applied to six semisolid geometries formed using a cooling rate of 0.14 K/s. This cooling rate was chosen from the CON1D simulation to match a value near the centre of casting slab. Two types of grain shapes were used: random realistic grains and cubic grains. The simulated average grain size ranged from 500 µm to 2000 µm. Further, a domain 12mm×12mm×12 mm having uniform temperature was selected. A dynamic viscosity of $\mu_l = 7.0 \times 10^{-3}\text{Pa} \cdot \text{s}$ [154] was assumed. The boundary conditions were set as follows: a constant pressure and uniform solute concentration on the top surface, *i.e.* $p_0 = 0$ Pa and $c_0 = 1.55$ wt.%, a constant zero flux on the bottom surface of 0 µm·s^{-1} and closed lateral boundaries, *i.e.* $q_l = 0$ µm·s^{-1} due to the symmetry reason. Solidification shrinkage was the only driving force for the fluid flow.

Fig. 5.27(a) shows the incoming flow rate and the corresponding pressure drop for seven semisolids, each at $g_s = 0.92$, containing equiaxed dendrite grains created with both random realistic and cubic grain shape. The results indicate that the grain size has only a small influence on the flow and pressure field given the same solid fraction; either random grain or realistic could also predict the similar results given the flow rate and pressure obtained with grain size of 800 µm. When grain size increases, the incoming flow rate decreases and pressure drop is less. This effect is due to interfacial area between the solid and liquid phase, which becomes more dominant as the grain size is reduced to 500 µm.

The corresponding solute maps for the six semisolids containing random realistic grains are shown in Fig. 5.27(b), which provide a general view of the solute distribution under the same boundary conditions. The solute is seen to increase almost linearly from the top to the bottom, indicating that the solute is transported along the fluid flow and enriched at the bottom of the domain achieving a local value of $c = 1.817$ wt.% for semisolid with an average grain size of 500 µm and $c = 1.616$ wt.% for a grain size of 2000 µm. Thus, the solute distribution is seen to vary significantly with grain size even though the flow rate and pressure drop are similar. This distinct difference is due to the large solid/liquid interfacial area encountered in the domain with smaller grain size where more solute is rejected from the solid phase.

Application to the continuous casting crocess

Model predictions: to quantitatively predict centreline solute enrichment, a semisolid microstructure with 27 subdomains was created. Each subdomain had solid fraction gradient as shown in Fig. 5.23(c). Solid fraction gradients in the transverse x and longitudinal z directions were neglected within each subdomain, however a solid fraction gradient in y corresponding to P_i and P_{ii}

was applied. An average grain size of 800 µm, matching the experimental measurements, was used as an input parameter to the model. Fig. 5.28 shows the calculated pressure drop, average flux along with the average concentration through the centreline mushy zone of the continuously casting slab. The pressure drop is entirely due to solidification shrinkage. This figure clearly indicates that the pressure drops only slightly during the first 25 subdomains, whereas it drops significantly in the last two subdomains due to the low permeability near the solidus. The corresponding liquid flux is shown to decrease incrementally until it reaches zero at the solidus line. The average Mn concentration in the liquid phase predicted by the solute model is seen to progressively accumulate due to both solute partitioning between the solid and liquid phases as well as fluid flow.

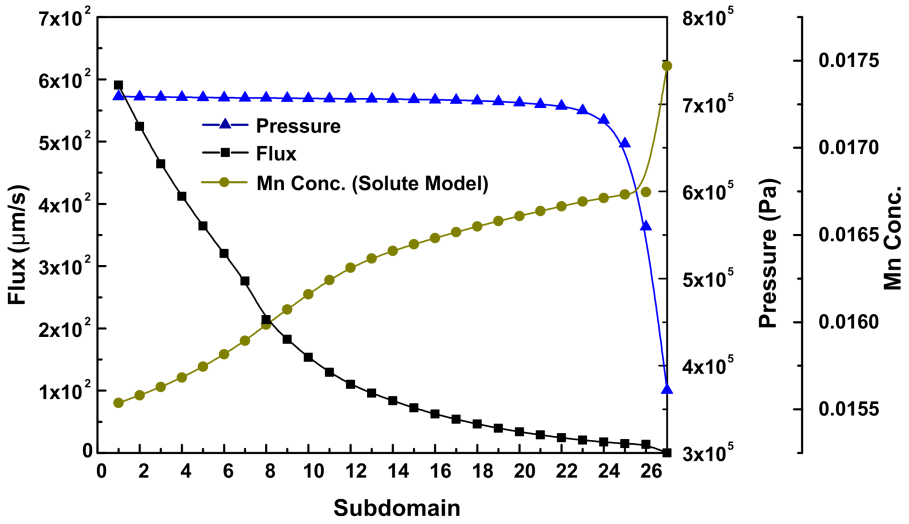

Figure 5.28: Predicted flux, pressure, and Mn concentration evolution within the entire mushy zone as a function of the subdomain number. The results presented represent the average value obtained at the subdomain interface.

Fig. 5.29 shows the corresponding Mn solute contours within four subdomains. Note that the coordinates of each subdomain are also plotted for the purposes of identifying its location. During the initial stage shown in Fig. 5.29(a) the solute will be mainly transported longitudinally as the fluid flow direction is mainly parallel to z, and slightly in the transverse direction to feed shrinkage outside of the model domain. Further down the caster, the flow is likely to compensate shrinkage in the transverse direction and the solute in enriched in the lateral of the subdomain shown in Fig. 5.29(b). Once the solidus line reaches the location of 10 mm away from the centreline, fluid flow is not able to carry the solute away due to the solidified sidewalls, and enriched near the lateral as well as the bottom which can be seen in Fig. 5.29(c).

The enrichment of the solute near the centre of the casting slab would be captured in Fig. 5.29(d) with the averaged local solid fraction up to 0.985 and only the enriched liquid near the centre remains to solidify. Compared with Fig. 5.29(a)-(d), the presence of fluid flow and solute partition lead eventually to the enrichment of solute concentration within liquid channels inside the solid structure indicated as by the color bars.

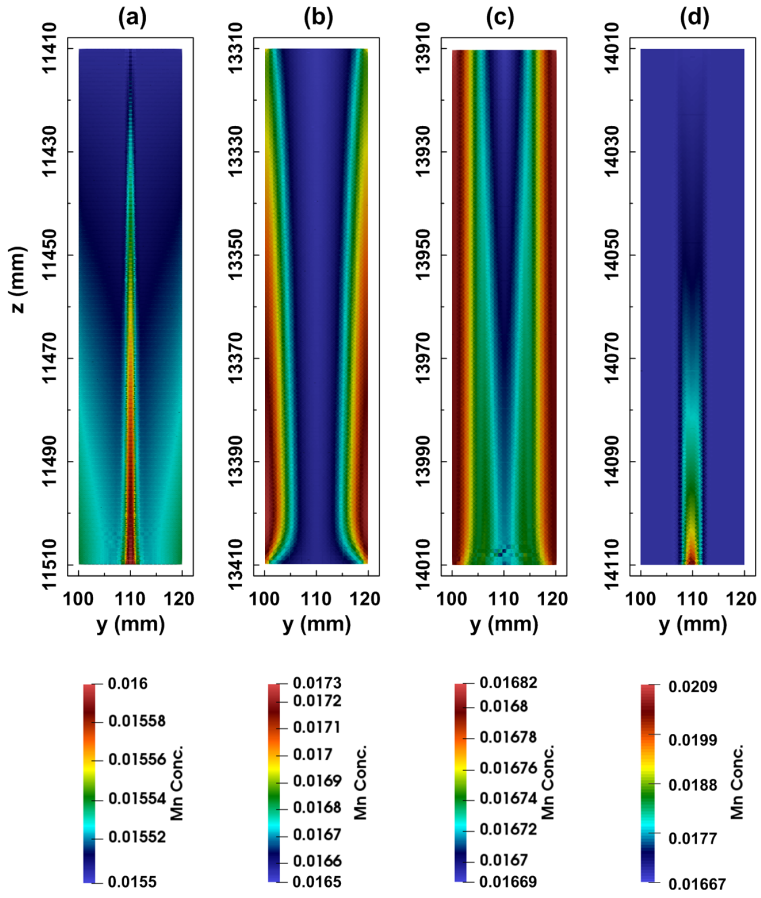

Figure 5.29: Influence of solid fraction gradient on the solute distribution. The subdomains correspond to subdomain number in Fig. 5.28: (a) subdomain 1,(b) subdomain 20, (c) subdomain 26 and (d) subdomain 27.

Experimental results: the XRF measurements showing the solute distribution in the test sample are given in Fig. 5.30. The image (a) provides the full area-map distribution while (b) shows the detail across a scanning line. Note that the maximum and minimum of the solute concentration are obtained from the data file using values 3 standard deviations from the mean, and the results are normalized based on the obtained values. The acquired solute profiles reveal both solute enrichment in Mn as well as the solidification morphology.

The dendritic structure is illustrated by the Mn-poor areas, while the inter-dendritic regions with segregated Mn are represented by the Mn-rich areas. Columnar dendrites prevail growing parallel along the heat flux direction from the surface towards the centre, but are blocked by the equiaxed dendrites forming near the centre (≈20 mm -wide through the centreline). There is also a region of random equiaxed grains on the right side of map due to the sedimentation during the casting process.

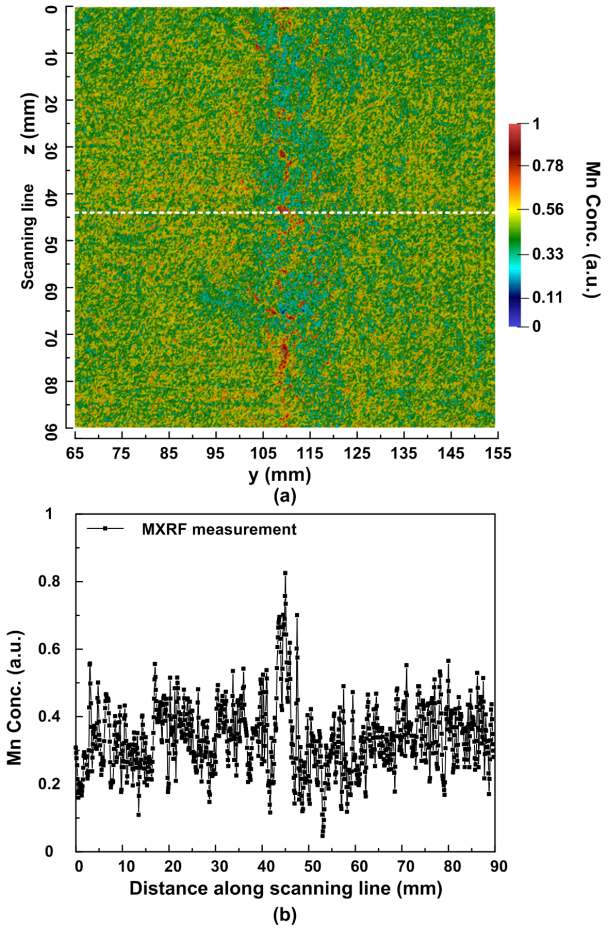

Figure 5.30: Solute mapping images of micro-segregation of Mn examined by MXRF in the section near centre of the continuously cast slab.

The solute is seen to be enriched near the centre of the test sample, i.e. the centre of the as-cast slab, where the enriched liquid is assumed to be solidified in the final stage. Referring now to the solute profile over the scanning line, solute inhomogeneity is easily identified by the peaks and valleys representing the positive segregation and negative segregation, respectively. The highest peak is observed near the centre corresponding to the red spot in Fig. 5.30(a). Note that it is not possible to identify the exact concentration in the last

solidified liquid films since the Mn concentration is an average value over the spot size.

Model validation (solute distribution): the simulations results obtained using a uniform grain size and an average grain size are almost the same identified by Fig. 5.27, but the former one is found to be more stable and efficient during computational process. The uniform grain size was used in the solute profiles in Fig. 5.29 indicating the incremental enrichment of solute near the solidus line. However, it is not an ideal case for the validation as these results were not able to capture the random distribution of grains with different grain sizes and variations in distances between different liquid channels. To make an appropriate comparison between the experimental measurement and the simulation prediction, a smaller subdomain with a dimension of 20mm × 20mm × 20mm containing different grain sizes is placed near the end of the solidus line for the validation. The semisolid geometries was also formed using the cooling rates of 0.14 K/s with an average grain size of 800 µm for these simulations. The boundary condition imposed on the top of the domain is interpolated using liquid solute concentration from the results obtained via uniform grains at the same location of 20 mm away from the solidus lines in z direction. The solid fraction gradient within this subdomain also follows Fig. 5.23(c). Solidification shrinkage was considered in the simulation.

The mesoscale model has reproduced some key features of the experimental measurements such as the random distribution of equiaxed grain, the tortuosity of the fluid flow and the enrichment of the solute enrichment at the grain boundary. Compared with the results in Fig 5.29 using a uniform grain size, the stochastic variation of shape and size due to the use of a Voronoi tessellation leads an unsymmetrical profile of the solute map shown in Fig. 5.31 (a) but with a higher computational cost. This geometry is appropriate for simulation the solute localization within the casting slabs containing random arrangement of equiaxed grains. Similar as subdomain 27, the fluid is no where to escape but enriched near the center of the slabs. The quantitative comparison is shown in Fig. 5.31 (b) where the line perpendicular to the casting direction near the solidus line is drawn, shown in Fig. 5.31(a), beyond which the remaining melt is supposed to solidify with the same density as that of the liquid melt. Thus, the solute distribution along the line remains constant once it is cast beyond the solidus line. Fig. 5.31 (b)shows the fit of the experimental data to the prediction of solute concentration predicted by the present model. The blue triangles represent solute concentration within the discrete liquid channels along the dashed line in Fig. 5.31 (a). Excellent agreement can be observed, where a solute is gradually increased towards the center. The fit is well matched of the peak near the center, and is still in good match at 8 mm away from the center. However, value predicted via the present model is slightly higher compared with the MXRF data. It was concluded that a

much better agreement is likely to achieve if a higher resolution in the experiment analysis is used and the proportion of the solid phase and liquid phase within each spot size is properly accounted for. This discrepancy is also due to the fact that the present model only simulates the solute redistribution in the discrete liquid channels.

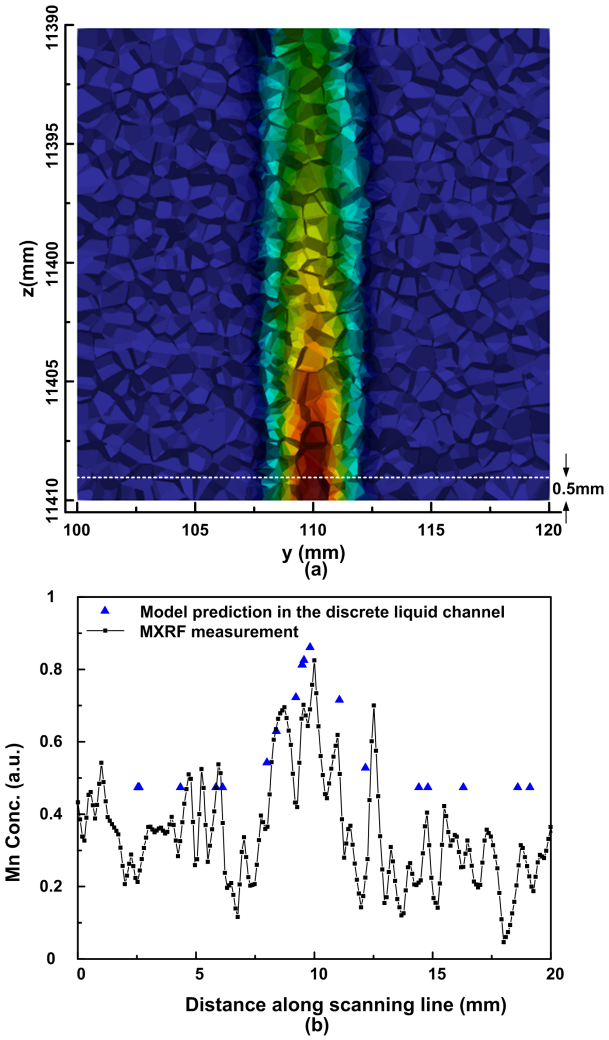

Figure 5.31: Comparison of solute distribution via experimental measurement and 3D mesoscale solute transport model.

Influence of strain rate on segregation

In addition to solidification shrinkage, mechanical deformation plays a great influence on the fluid flow and therefore on the solute segregation. The influence of mechanical deformation can be introduced into the fluid flow model through

the source term Δv_{liq} in Eq. 4.2.10. A negative value represents compression due to soft reduction while a positive value represents tensile strain.

Fig. 5.32 shows the flow rates and pressure drops, and corresponding centreline segregation under different mechanical deformation rates at the end of the mushy zone. As can be seen, the model reproduces expected behaviour: when a tensile strain is applied enriched liquid is sucked in to the domain to compensate for the mechanical deformation as indicated by an increase in the incoming flux and higher pressure drop whereas compression compensates the solidification shrinkage thus leads to less incoming flow. The change in melt flow behaviour is also seen to change the solute distribution. With an increase in compression rate, the centreline segregation is reduced as the thickness of the solute enriched region narrows. In contrast, a tensile strain rate will widen the solute-enriched region, and enhance the formation of positive macrosegregation. A key advantage of the current methodology over previous studies is the computational cost; parametric studies can be easily conducted to determine the effects of process parameters on segregation patterns.

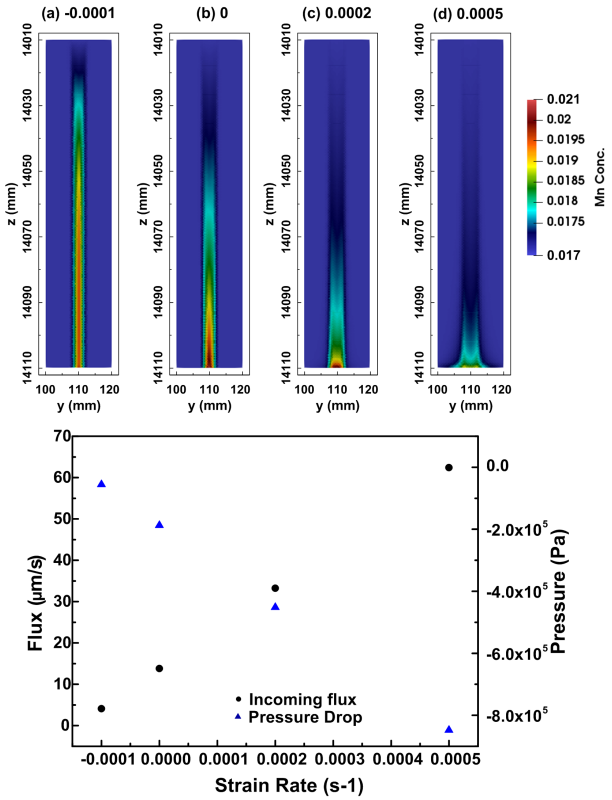

Figure 5.32: Influence of strain rate on the solute distribution. The influence of strain rate on the incoming flux and pressure drop are also shown below.

Influence of peritectic reaction on segregation

The relative severity of macrosegregation for different steels is critically important when industry is designing new grades, especially AHSS. Mechanistically, it is the presence of a peritectic transformation that influences greatly the macrosegregation due to the corresponding changes in solidification shrinkage which change the flow pattern. The influence of the peritectic transformation on shrinkage and the resulting fluid flow has been extensively investigated in Ref. [147]. In this investigation, a semi-solid morphology was created with the same solid fraction gradient in the transverse direction as Fig 5.31(a) for both non-peritectic (Fe-0.05wt.%C-1.55wt.%Mn) and hypo-peritectic grade (Fe-0.105wt.%C-1.55wt.%Mn). The boundary condition for the fluid flow is the same as Fig. 5.31(a). Since this study only focused on the influence of carbon content on the flow pattern, the incoming solute concentration of Mn in the liquid is set to be 1.55wt.% and is uniformly distributed.

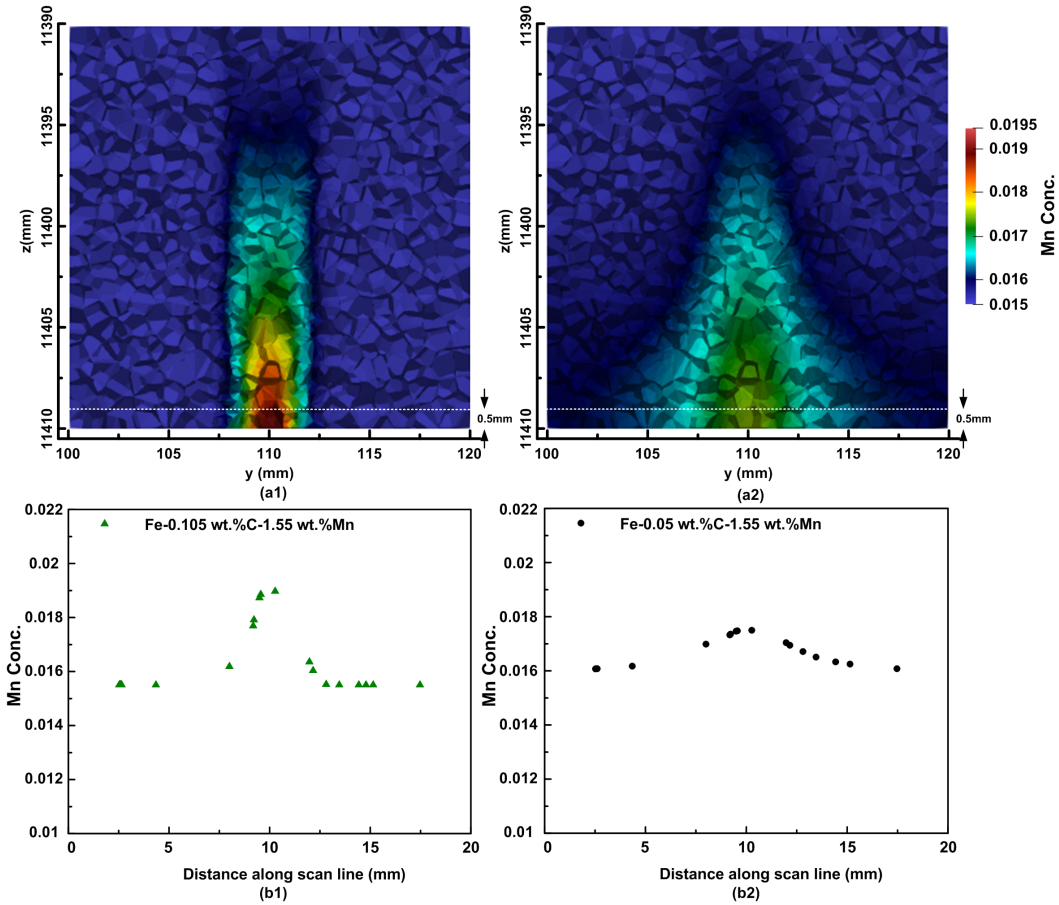

Figure 5.33: Influence of carbon contents on the solute distribution of Mn.

The solute maps between non-peritectic and hypo-peritectic grade are plotted in Fig. 5.33(a). Clearly the centreline segregation is more severe in hypo-peritectic grade compared with non-peritectic. The quantitatively comparison along the dashed line located at 5 mm away from the solidus line perpendicular to z direction is shown in Fig. 5.33(b). The peak is higher near the center for hypo-peritectic grade while the solute localization within the non-peritectic grade is relatively even. The higher concentration observed in the hypo-peritectic grade is attributed to the following reason: on the one hand, the shrinkage caused by the peritectic transformation at the near the center requires more liquid to compensate the volume change, and the solute is enriched near the center; on the other hand the solute rejection from the solid phase per unit time will increase due to the higher growth rate of the austenite phase.

Chapter 6

Conclusions

This chapter provides key contributions of the thesis, followed by an outline of the major limitations of the present model and suggestions for future work, particularly for the prediction of hot tearing and segregation within a metallic semisolid.

6.0.1 Conclusions

The key conclusions of sub-models and coupled models are summarized as follows:

A 3D meso-scale dendritic solidification model based on the volume average method is proposed to predict the evolution in semi-solid microstructure of steel alloys and consequently liquid film migration. This model is applied to Fe-C binary alloys having experiencing both primary solidification and the peritectic transformation. Solute diffusion within each phase (intra-dendritic liquid, extra-dendritic liquid, δ phase and γ phase) is considered. The coalescence phenomenon between grains is considered at the end of solidification using Bulatov's approach for estimating interfacial energy. It is seen that only 0.9% of the grains are attractive based on their orientations, significantly depressing final-stage solidification. The capability of the model in predicting solidification with both globular and dendritic structure has been demonstrated using a case study of two different cooling rates. At 0.1°C/s, a globular structure is predicted to form, while at 50°C/s a dendritic morphology is favored. The model is then applied to correlate the semi-solid microstructure evolution to different physical and process parameters. The formation of austenite at increased carbon content, due to the peritectic transformation, will sharply increase the solid fraction and narrow the remaining liquid film widths. An increase in the cooling rate leads to higher deviation from equilibrium and thus lower solid fraction at a specified temperature which in turn reduces the occurrence of hot tearing. A domain with small grains will have thin liquid

channels as compared to large grains, but there will be much more interfacial area thus more coalescence to resist hot tearing. Large grains are prone to hot tear due because of the difficulty in feeding through only a few liquid channels. The underlying microstructure leading to high hot tearing susceptibility of hypo-peritectic grades – namely liquid channels that are too thin to allow for feeding to compensate the volume change associated with the peritectic transformation – is identified.

A 3D dendritic fluid flow model has been developed to quantitatively predict the fluid flow behaviour induced by the solidification shrinkage at the meso-scale, through thousands of equiaxed grains. The model is based on the Darcy-Brinkman form of the Navier-Stokes equation at a prescribed solid fraction. Using the framework of the Voroinoi tessellation, the tortuosity of flows around the complex interdendritic channels was considered. This new technique captures both semi-solid morphology and the fluid flow behavior during solidification, and provides an alternative to the convectional experiment for the prediction of permeability by using the given surface area concentration. Comparison of the numerical and experimental permeabilities shows a good agreement (within $\pm$ 5%) for either extra-dendrite or intra-dendritic flow, and deviation from the conventional Carman-Kozeny equations using simplified Dendritic S_v or Globular S_v are explained in detail. The results quantitatively demonstrate the effect of grain size and microstructure morphology during solidification on the permeability prediction.

The localization of liquid feeding under the pressure gradient is also reproduced in the present investigation. The results highlight the ability in predicting liquid feeding within a semisolid domain where local permeability varies. Additionally, the advection of fluid due to shrinkage and deformation for non-peritectic and peritectic steel grades with dendritic morphology during solidification was captured for the first time, and the results were validated with empirical equations. Due to the large solid/liquid surface area of the dendritic structure, the advection of fluid is dominated by the shrinkage during the peritectic phase transformation within the mushy zone under the small deformation rate, and easily cause the formation of casting defect.

The semisolid deformation model and semisolid cracking model simulate the rheological behavior of the semi-solid domain under feedable and unfeedable conditions and results are validated with the semisolid tensile test experimental measurements. The simulation performed on two alloy grades under a feedable mushy zone indicates that a higher pressure drop is observed in the peritectic alloy compared with non-peritectic alloy due to the shrinkage associated with peritectic transformation, but no crack would occur in both alloys due to adequate liquid feeding. In unfeedable mushy zone, the semisolid cracking model is able to predict the crack initiation and propagation. The tensile strength predicted by the semisolid cracking model agrees well with the

experimental measurement, which increases with the increase of solid fraction. The results are shown to be related to bridging occurring within the semisolid and influenced by the proportion of the attractive grains. Additionally, hot tearing sensitivity of a mushy zone increases with the increase of sulfur and oxygen contents in the liquid phase.

A 3D solute transportation model has been developed to quantitatively predict the solute redistribution induced by the solidification shrinkage and mechanical deformation at the mesoscale. This mesoscale solute transport model provides an alternative to the convectional simulation methods which requires heavy computational cost. The results indicate that the grain size used in the simulation has a great impact on the solute distribution due to larger solid/liquid interfacial area encountered in the domain with smaller grain size where more solute is rejected from the solid phase. Solute partitioning combined with intra-dentritic fluid flow leads eventually to liquid channels enriched with solute near the centreline of continuous casting slab. The solute enriched within the thin liquid channels at the end of solidification is validated with the measurements via MXRF quantitatively. The change in melt flow behaviour is also seen to change the solute distribution, where centreline segregation is reduced with an increase of compression rate while an increase of tensile strain rate enhance the formation of positive macrosegregation. The present model is also able to indicate that the centreline segregation is more severe in hypo-peritectic grade compared with non-peritectic due to solidification shrinkage and the higher growth rate of the austenite phase.

6.0.2 Model limitations and potential future works

The critical model assumptions and the limitations of the present model are discussed along with some potential future works to the present investigation.

(1) The present model focuses on the solidification behavior of semisolid containing equiaxed grains. However, the severe cracking problem is also found near the columnar grains region. This could be achieved by creating a semisolid with elongated columnar grains growing in the same direction. A coalescence criterion needs to be imposed between these columnar grains under tensile or shear deformation. The new semisolid morphology allows for the prediction of hot tearing sensitivity analysis within the columnar region.

(2) One major limitation relates to the use of fixed solid grains created by the Voronoi tessellation. The implication of this assumption is validated at the final-stage solidification, but can not be able to capture the grain movement during the initial solidification process where the solid fraction of the semisolid is relative low. This means that the high liquid velocity of the liquid would change the location of the solid grains and then influence the solute profile at initial-stage solidification. The same problem also rises during the deformation

analysis during solidification as pointed out by Sistaninia et al. [1].

(3) In the solute transport model, the microstructure is assumed to be pure dendritic and only intra-dendritic flow occurs. Hence, this model is not able to distinguish the solute profile in the intra-dendritic region and the extra-dendritic region resulting from the presence of the fluid flow. This limitation would be eliminated through the development of a more elegant solute transport model where the liquid is split into two phases (intra-dendritic and extra-dendritic liquid phase), and the solute exchange at the solid/intra-dendritic and intra-dendritic/extra-dendritic phase interfaces are considered. Then the improved solute transport model could be able to distinguish the solute profile in intra and extra-dendritic region within a semisolid given the intra-dendritic and extra-dendritic fluid velocity predicted by the mesoscale fluid flow model.

(4) The coalescence undercooling used in the present work is calculated based on the grain boundary energy as proposed by Bulatov et al. [24] to better describe the repulsive/attractive proportion of grain boundaries. The present mesoscale model used the grain boundary energy of Ni as an approximation of the γ-Fe due to similar properties. Note that Bulatov's model is only applicable to predict the grain boundary of FCC metal, but not for BCC metal such as δ-Fe. This means that the coalescence predicted in this investigation only focused on the peritectic grades where a layer of γ-Fe formed on the periphery of the primary δ-Fe phase. This limitation could be removed by using a more elaborate grain boundary model which is applicable for both BCC structure as well as FCC structure metals.

(5) Coalescence between the dendritic structure is crucial in predicting the hot tearing. In a globular case, the two grains are assumed to be either fully coalesced or separated by a layer of liquid film. In dendritic structure, the coalescence between the dendrite tips has to be better considered to describe the deformation of a semisolid. This limitation could be removed if one are able to considered the progressive coalescence between the two dendritic structures based on for example of the internal solid fraction or the interfacial area between the solid and the liquid phase.

(6) Solute segregation under deformation is predicted by imposing a source term in the fluid flow equation. This simplified assumption can not be able to study the solute redistribution under deformation simultaneous. A real time investigation of deformation on the solute redistribution in the liquid phase can be achieved by coupling between fluid flow model, deformation model and solute transport models. The influence of deformation on the fluid flow behavior would be predicted first and then in turn causes a redistribution of solute.

6.0.3 Industrial applications

The model developed in this thesis is built on the formulation of continuum equations and simulates the important physical phenomena associated with defects formation during solidification process of steel. It is interesting to note that the results of this work are essentially due to the consideration of physical phenomena of different phases that are classically hidden by the averaging procedure of continuum approaches. Moreover, the low computational cost of the current model allows for its application to industrial process over large scales while taking into account of the fundamental mechanism at a scale of microstructure.

The current model helps to investigate the microstructure evolution within the entire mushy zone of casting slabs, and predicts the fluid flow behavior and pressure distribution at every locations inside the mushy zone. Specifically, the solidification behavior of alloys with peritectic transformation is captured. One can also use this model to assess the hot tearing sensitivity of different steel grades under a specific casting condition. Another application of the current model is to predict the centreline segregation within the continuous casting slab, where the solute distribution within the liquid channels is predicted quantitatively.

By overcoming the limitations identified above, the current model can be further extended and become a more advanced predictive tool for defect formation. In addition to continuous casting process of steel, this approach is also applicable to welding, direct casting or ingot casting process for other metallic materials. This technique would help metallurgists to have a better idea of the range of alloys compositions that can be industrially produced and alleviate the long-term severe problems during casting, which allows for the increase of productivity and optimization of casting procedures.

Bibliography

[1] Meisam Sistaninia. Prediction of hot tearing formation in metallic alloys using a granular approach. Technical report, EPFL, 2013.

[2] HR Zareie Rajani and AB Phillion. A mesoscale solidification simulation of fusion welding in aluminum–magnesium–silicon alloys. *Acta materialia*, 77:162–172, 2014.

[3] Dong Jin Seol, Young Mok Won, Tae-jung Yeo, Kyu Hwan Oh, Joong Kil Park, and Chang Hee Yim. High temperature deformation behavior of carbon steel in the austenite and δ-ferrite regions. *ISIJ international*, 39(1):91–98, 1999.

[4] Passenger car fuel economy normalized to cafe. `https://theicct.org/chart-library-passenger-vehicle-fuel-economy`. Accessed: 2020-05-30.

[5] Nina Fonstein. *Advanced high strength sheet steels*. Springer, 2015.

[6] Klaus Timmel, Sven Eckert, Gunter Gerbeth, Frank Stefani, and Thomas Wondrak. Experimental modeling of the continuous casting process of steel using low melting point metal alloys—the limmcast program. *ISIJ international*, 50(8):1134–1141, 2010.

[7] Hongbin Yin, Kenneth Blazek, and Oscar Lanzi. "in-situ" observation of remelting phenomenon after solidification of fe-b alloy and b-bearing commercial steels. *ISIJ international*, 49(10):1561–1567, 2009.

[8] Michel Bellet, Olivier Cerri, M Bobadilla, and Yvan Chastel. Modeling hot tearing during solidification of steels: assessment and improvement of macroscopic criteria through the analysis of two experimental tests. *Metallurgical and Materials Transactions A*, 40(11):2705, 2009.

[9] Doru M Stefanescu. Microstructure evolution during the solidification of steel. *ISIJ international*, 46(6):786–794, 2006.

[10] Naotsugu Yoshida, Osamu Umezawa, and Kotobu Nagai. Influence of phosphorus on solidification structure in continuously cast 0.1 mass% carbon steel. *ISIJ international*, 43(3):348–357, 2003.

[11] Ed J Pickering, Connor Chesman, Sinan Al-Bermani, Melanie Holland, Peter Davies, and Jesus Talamantes-Silva. A comprehensive case study of macrosegregation in a steel ingot. *Metallurgical and Materials Transactions B*, 46(4):1860–1874, 2015.

[12] Jonathan A Dantzig and Michel Rappaz. *Solidification: -Revised & Expanded*. EPFL press, 2016.

[13] Young Mok Won, Tae-Jung Yeo, Dong Jin Seol, and Kyu Hwan Oh. A new criterion for internal crack formation in continuously cast steels. *Metallurgical and Materials Transactions B*, 31(4):779–794, 2000.

[14] Mikio Suzuki, Makoto Suzuki, Chonghee Yu, and Toshihiko Emi. In-situ measurement of fracture strength of solidifying steel shells to predict upper limit of casting speed in continuous caster with oscillating mold. *ISIJ international*, 37(4):375–382, 1997.

[15] Shahrooz Nafisi, Omid Lashkari, Reza Ghomashchi, Frank Ajersch, and Andre Charette. Microstructure and rheological behavior of grain refined and modified semi-solid a356 al–si slurries. *Acta materialia*, 54(13):3503–3511, 2006.

[16] Yu Xu, Rong-jun Xu, Zheng-jie Fan, Cheng-bin Li, An-yuan Deng, and En-gang Wang. Analysis of cracking phenomena in continuous casting of 1cr13 stainless steel billets with final electromagnetic stirring. *International Journal of Minerals, Metallurgy, and Materials*, 23(5):534–541, 2016.

[17] Mohammadhossein Ghoncheh. *HIGH-TEMPERATURE PHYSICO-MECHANICAL PROPERTIES OF AS-RECEIVED STRUCTURES IN DUAL-PHASE ADVANCED HIGH-STRENGTH STEELS*. PhD thesis, 2019.

[18] I Farup, J-M Drezet, and M Rappaz. In situ observation of hot tearing formation in succinonitrile-acetone. *Acta materialia*, 49(7):1261–1269, 2001.

[19] Chedtha Puncreobutr, Peter D Lee, Richard W Hamilton, Biao Cai, and Thomas Connolley. Synchrotron tomographic characterization of damage evolution during aluminum alloy solidification. *Metallurgical and Materials Transactions A*, 44(12):5389–5395, 2013.

[20] M Rappaz, J-M Drezet, and Met Gremaud. A new hot-tearing criterion. *Metallurgical and materials transactions A*, 30(2):449–455, 1999.

[21] V Mathier, P-D Grasso, and M Rappaz. A new tensile test for aluminum alloys in the mushy state: experimental method and numerical modeling. *Metallurgical and Materials Transactions A*, 39(6):1399–1409, 2008.

[22] M Sistaninia, S Terzi, AB Phillion, J-M Drezet, and M Rappaz. 3-d granular modeling and in situ x-ray tomographic imaging: a comparative study of hot tearing formation and semi-solid deformation in al–cu alloys. *Acta materialia*, 61(10):3831–3841, 2013.

[23] HR Zareie Rajani and AB Phillion. 3d multi-scale multi-physics modelling of hot cracking in welding. *Materials & Design*, 144:45–54, 2018.

[24] Vasily V Bulatov, Bryan W Reed, and Mukul Kumar. Grain boundary energy function for fcc metals. *Acta Materialia*, 65:161–175, 2014.

[25] Joydeep Sengupta, Jackie Leung, and Amir Noorafkan. Calibration and validation of x-ray fluorescence technique for mapping centreline segregation on steel slabs. In *AISTech 2017 Conference Proceedings*, pages 1925–1938, 2017.

[26] Joydeep Sengupta and Amir Noorafkan. Quantifying slab centerline segregation: Mxrf eliminates sample preparation and etching procedures. In *AISTech 2018 Conference Proceedings*, pages 2637–2649, 2018.

[27] Dong Jin Seol, Young Mok Won, Kyu Hwan Oh, Yong Chang Shin, and Chang Hee Yim. Mechanical behavior of carbon steels in the temperature range of mushy zone. *ISIJ international*, 40(4):356–363, 2000.

[28] John Chipman. Thermodynamics and phase diagram of the fe-c system. *Metallurgical and Materials Transactions B*, 3(1):55–64, 1972.

[29] Wilfried Kurz and David J Fisher. *Fundamentals of Solidification*. Trans Tech Publications, Aedermannsdorf, Switzerland, 1998.

[30] Machiko ODE, Seong Gyoon KIM, Won Tae KIM, and Toshio SUZUKI. Numerical simulation of peritectic reaction in fe-c alloy using a multi-phase-field model. *ISIJ international*, 45(1):147–149, 2005.

[31] DY Sun, M Asta, and JJ Hoyt. Crystal-melt interfacial free energies and mobilities in fcc and bcc fe. *Physical Review B*, 69(17):174103, 2004.

[32] Minoru Yamazaki, Yukinobu Natsume, Hiroshi Harada, and Kenichi Ohsasa. Numerical simulation of solidification structure formation during continuous casting in fe–0.7 mass% c alloy using cellular automaton method. *ISIJ international*, 46(6):903–908, 2006.

[33] JM Drezet, M Gremaud, R Graf, and M Gaümann. A new hot tearing criterion for steel. In *Proceedings of the 4th European Continuous Casting Conference, IOM communications, Birmingham, UK*, pages 755–763, 2002.

[34] JK Brimacombe and K Sorimachi. Crack formation in the continuous casting of steel. *Metallurgical transactions B*, 8(2):489–505, 1977.

[35] BG Thomas, IV Samarasekera, and JK Brimacombe. Mathematical model of the thermal processing of steel ingots: Part ii. stress model. *Metallurgical transactions B*, 18(1):131, 1987.

[36] Takao Koshikawa, Michel Bellet, Charles-André Gandin, Hideaki Yamamura, and Manuel Bobadilla. Study of hot tearing during steel solidification through ingot punching test and its numerical simulation. *Metallurgical and materials transactions A*, 47(8):4053–4067, 2016.

[37] Edward John Pickering. Macrosegregation in steel ingots: the applicability of modelling and characterisation techniques. *ISIJ international*, 53(6):935–949, 2013.

[38] Nazim Baluch, Zulkifli Mohamed Udin, and Che Sobry Abdullah. Advanced high strength steel in auto industry: an overview. *Engineering, Technology & Applied Science Research*, 4(4):686–689, 2014.

[39] R Kuziak, Rudolf Kawalla, and Sebastian Waengler. Advanced high strength steels for automotive industry. *Archives of civil and mechanical engineering*, 8(2):103–117, 2008.

[40] MI Khan, ML Kuntz, and Y Zhou. Effects of weld microstructure on static and impact performance of resistance spot welded joints in advanced high strength steels. *Science and Technology of Welding and Joining*, 13(3):294–304, 2008.

[41] Takehide Senuma. Physical metallurgy of modern high strength steel sheets. *ISIJ international*, 41(6):520–532, 2001.

[42] Sung-Moo SONG, Koh-ichi SUGIMOTO, Mitsuyuki KOBAYASHI, Hideyuki MATSUBARA, and Takahiro KASHIMA. Impact properties of low alloy trip steels. *Tetsu-to-Hagane*, 86(8):563–569, 2000.

[43] Abey Abraham. Metallic material trends in the north american light vehicle. *Ducker Worldwide*, 13, 2015.

[44] David K Matlock, John G Speer, Emmanuel De Moor, and Paul J Gibbs. Recent developments in advanced high strength sheet steels for automotive applications: an overview. *Jestech*, 15(1):1–12, 2012.

[45] S Kim Kim, Gyosung Kim, and KG Chin. Development of high manganese twip steel with 980mpa tensile strength. In *Proceedings of the International Conference on New Developments in Advanced High-Strength Sheet Steels, Association for Iron and Steel Technology, Orlando*, pages 249–256, 2008.

[46] A Grajcar, R Kuziak, and W Zalecki. Third generation of ahss with increased fraction of retained austenite for the automotive industry. *Archives of civil and mechanical engineering*, 12(3):334–341, 2012.

[47] Brian G Thomas. Review on modeling and simulation of continuous casting. *steel research international*, 89(1):1700312, 2018.

[48] J Sengupta, BG Thomas, and MA Wells. The use of water cooling during the continuous casting of steel and aluminum alloys. *Metallurgical and Materials Transactions A*, 36(1):187–204, 2005.

[49] Brian G Thomas. Modeling of the continuous casting of steel—past, present, and future. *Metallurgical and materials transactions B*, 33(6):795–812, 2002.

[50] R Bommaraju, JK Brimacombe, and IV Samarasekera. Mould behaviour and solidification in the continuous casting of steel billets. iii. structure, solidification bands, crack formation and off-squareness. *Transactions of the Iron and Steel Society of AIME*, 5:95–105, 1984.

[51] X Huang, Brian G Thomas, and FM Najjar. Modeling superheat removal during continuous casting of steel slabs. *Metallurgical and Materials Transactions B*, 23(3):339–356, 1992.

[52] M El-Bealy and Brian G Thomas. Prediction of dendrite arm spacing for low alloy steel casting processes. *Metallurgical and materials transactions B*, 27(4):689–693, 1996.

[53] H Neumann-Heyme, K Eckert, and C Beckermann. General evolution equation for the specific interface area of dendrites during alloy solidification. *Acta Materialia*, 140:87–96, 2017.

[54] Gregor Arth, Sergiu Ilie, Robert Pierer, and Christian Bernhard. Experimental and numerical investigations on hot tearing during continuous casting of steel. *BHM Berg-und Hüttenmännische Monatshefte*, 160(3):103–108, 2015.

[55] Peter Presoly, Robert Pierer, and Christian Bernhard. Identification of defect prone peritectic steel grades by analyzing high-temperature phase transformations. *Metallurgical and Materials Transactions A*, 44(12):5377–5388, 2013.

[56] Young-Mok Won and Brian G Thomas. Simple model of microsegregation during solidification of steels. *Metallurgical and materials transactions A*, 32(7):1755–1767, 2001.

[57] M El-Bealy. On the mechanism of halfwaycracks and macro-segregation in continuously cast steel slabs. i: Halfway cracks. *Scandinavian journal of metallurgy*, 24(2):63–80, 1995.

[58] Hideaki MIZUKAMI, Masami KOMATSU, Toru KITAGAWA, and Kiminari KAWAKAMI. Effect of electromagnetic stirring at the final stage of solidification of continuously cast strand. *Tetsu-to-Hagané*, 70(2):194–200, 1984.

[59] SK Choudhary and Suvankar Ganguly. Morphology and segregation in continuously cast high carbon steel billets. *ISIJ international*, 47(12):1759–1766, 2007.

[60] V Ludlow, A Normanton, A Anderson, M Thiele, J Ciriza, J Laraudogoitia, and W Van Der Knoop. Strategy to minimise central segregation in high carbon steel grades during billet casting. *Ironmaking & steelmaking*, 32(1):68–74, 2005.

[61] Bo Sundman, Bo Jansson, and Jan-Olof Andersson. The thermo-calc databank system. *Calphad*, 9(2):153–190, 1985.

[62] Ch W Bale, P Chartrand, SA Degterov, G Eriksson, K Hack, R Ben Mahfoud, J Melançon, AD Pelton, and S Petersen. Factsage thermochemical software and databases. *Calphad*, 26(2):189–228, 2002.

[63] M Rappaz, A Jacot, and William J Boettinger. Last-stage solidification of alloys: Theoretical model of dendrite-arm and grain coalescence. *Metallurgical and Materials Transactions A*, 34(3):467–479, 2003.

[64] Stéphane Vernede, Philippe Jarry, and Michel Rappaz. A granular model of equiaxed mushy zones: Formation of a coherent solid and localization of feeding. *Acta Materialia*, 54(15):4023–4034, 2006.

[65] Hubert Preßlinger, Sergiu Ilie, Peter Reisinger, Andreas Schiefermüller, Andreas Pissenberger, Erik Parteder, and Christian Bernhard. Methods for assessment of slab centre segregation as a tool to control slab continuous casting with soft reduction. *ISIJ international*, 46(12):1845–1851, 2006.

[66] DG Eskin, J Zuidema Jr, VI Savran, and L Katgerman. Structure formation and macrosegregation under different process conditions during dc casting. *Materials Science and Engineering: A*, 384(1-2):232–244, 2004.

[67] SK Choudhary, S Ganguly, A Sengupta, and V Sharma. Solidification morphology and segregation in continuously cast steel slab. *Journal of Materials Processing Technology*, 243:312–321, 2017.

[68] Takao Koshikawa, Michel Bellet, Charles-André Gandin, Hideaki Yamamura, and Manuel Bobadilla. Experimental study and two-phase numerical modeling of macrosegregation induced by solid deformation during punch pressing of solidifying steel ingots. *Acta Materialia*, 124:513–527, 2017.

[69] M Co Flemings and GE Nereo. Macrosegregation. pt. 3. *Trans Met Soc AIME*, 242(1):50–55, 1968.

[70] JA Sarreal and GJ Abbaschian. The effect of solidification rate on microsegregation. *Metallurgical Transactions A*, 17(11):2063–2073, 1986.

[71] Terry F Bower, HD Brody, Merton C Flemings, et al. Measurements of solute redistribution in dendritic solidification. *AIME MET SOC TRANS*, 236(5):624–634, 1966.

[72] TW Clyne and W Kurz. Solute redistribution during solidification with rapid solid state diffusion. *Metallurgical Transactions A*, 12(6):965–971, 1981.

[73] Itsuo Ohnaka. Mathematical analysis of solute redistribution during solidification with diffusion in solid phase. *Transactions of the Iron and Steel Institute of Japan*, 26(12):1045–1051, 1986.

[74] Sumio Kobayashi. Mathematical analysis of solute redistribution during solidification based on a columnar dendrite model. *Transactions of the Iron and Steel Institute of Japan*, 28(9):728–735, 1988.

[75] CY Wang and C Beckermann. A unified solute diffusion model for columnar and equiaxed dendritic alloy solidification. *Materials Science and Engineering: A*, 171(1-2):199–211, 1993.

[76] J Lipton, ME Glicksman, and W Kurz. Dendritic growth into undercooled alloy metals. *Materials Science and Engineering*, 65(1):57–63, 1984.

[77] CY Wang and C Beckermann. A multiphase solute diffusion model for dendritic alloy solidification. *Metallurgical and Materials Transactions A*, 24(12):2787–2802, 1993.

[78] CY Wang, S Ahuja, C Beckermann, and HC De Groh. Multiparticle interfacial drag in equiaxed solidification. *Metallurgical and Materials Transactions B*, 26(1):111–119, 1995.

[79] Ch Beckermann. Modelling of macrosegregation: applications and future needs. *International Materials Reviews*, 47(5):243–261, 2002.

[80] Merton C Flemings and GE Nereo. Macrosegregation. pt. 1. *AIME Met Soc Trans*, 239(9):1449–1461, 1967.

[81] R Mehrabian, M Keane, and MC Flemings. Interdendritic fluid flow and macrosegregation; influence of gravity. *Metallurgical and Materials Transactions B*, 1(5):1209–1220, 1970.

[82] SD Ridder, S Kou, and R Mehrabian. Effect of fluid flow on macrosegregation in axi-symmetric ingots. *Metallurgical Transactions B*, 12(3):435–447, 1981.

[83] WD Bennon and FP Incropera. A continuum model for momentum, heat and species transport in binary solid-liquid phase change systems—i. model formulation. *International Journal of Heat and Mass Transfer*, 30(10):2161–2170, 1987.

[84] WD Bennon and FP Incropera. A continuum model for momentum, heat and species transport in binary solid-liquid phase change systems—ii. application to solidification in a rectangular cavity. *International Journal of Heat and Mass Transfer*, 30(10):2171–2187, 1987.

[85] Jun Ni and Christoph Beckermann. A volume-averaged two-phase model for transport phenomena during solidification. *Metallurgical Transactions B*, 22(3):349, 1991.

[86] Miha Založnik and Hervé Combeau. An operator splitting scheme for coupling macroscopic transport and grain growth in a two-phase multiscale solidification model: Part i–model and solution scheme. *Computational Materials Science*, 48(1):1–10, 2010.

[87] Miha Založnik, Arvind Kumar, Hervé Combeau, Marie Bedel, Philippe Jarry, and Emmanuel Waz. Influence of transport mechanisms on macrosegregation formation in direct chill cast industrial scale aluminum alloy ingots. *Advanced Engineering Materials*, 13(7):570–580, 2011.

[88] Harold D. Brody and Merton C. Flemings. Solute Redistribution in Dendritic Solidification. *Transaction of the Metallurgical Society of AIME*, 236(May):615–624, 1966.

[89] Philip Crosbie Carman. Fluid flow through granular beds. *Trans. Inst. Chem. Eng.*, 15:150–166, 1937.

[90] K Narita, T Mori, K Ayata, J Miyazaki, M Fujimaki, and T Shiomi. Determination of the temperature distribution in continuous casting process. *Tetsu-to-Hagané*, 64(11):S659, 1978.

[91] JM Drezet and M Rappaz. Study of hot tearing in aluminum alloys using the ring mold test. *Modeling of Casting, Welding and Advanced Solidification Processes VIII. San Diego, USA, TMS*, pages 883–890, 1998.

[92] TW Clyne and CLYNE TW. A quantitative solidification cracking test for castings and an evaluation of cracking in aluminium-magnesium alloys. 1975.

[93] D Warrington and DG McCartney. Development of a new hot-cracking test for aluminium alloys. *Cast Metals*, 2(3):134–143, 1989.

[94] B Mintz and JM Arrowsmith. Hot-ductility behaviour of c–mn–nb–al steels and its relationship to crack propagation during the straightening of continuously cast strand. *Metals technology*, 6(1):24–32, 1979.

[95] Warren F Savage. Apparatus for studying the effects of rapid thermal cycles and high strain rates on the elevated temperature behavior of materials. *Journal of Applied Polymer Science*, 6(21):303–315, 1962.

[96] DG Eskin, L Katgerman, et al. Mechanical properties in the semi-solid state and hot tearing of aluminium alloys. *Progress in materials science*, 49(5):629–711, 2004.

[97] BG Thomas, JK Brimacombe, and IV Samarasekera. The formation of panel cracks in steel ingots: a state-of-the-art review. *ISS Transactions*, 7(10):7–20, 1986.

[98] P Ackermann, W Kurz, and W Heinemann. In situ tensile testing of solidifying aluminium and al-mg shells. *Materials science and engineering*, 75(1-2):79–86, 1985.

[99] Christian Bernhard, Herbert Hiebler, and Manfred M Wolf. Simulation of shell strength properties by the ssct test. *ISIJ international*, 36(Suppl):S163–S166, 1996.

[100] V Laxmanan and MC Flemings. Deformation of semi-solid sn-15 pct pb alloy. *Metallurgical Transactions A*, 11(12):1927–1937, 1980.

[101] QY Pan, Diran Apelian, and Andreas N Alexandrou. Yield behavior of commercial al-si alloys in the semisolid state. *Metallurgical and materials transactions B*, 35(6):1187–1202, 2004.

[102] MA Chopra, ME Glicksman, and NB Singh. Measurement of the diffusion coefficient of acetone in succinonitrile at its melting point. *Journal of crystal growth*, 92(3-4):543–546, 1988.

[103] O Prakash and DRH Jones. Creep of metal-type organic compounds—i. pure polycrystals and particle-hardened systems. *Acta metallurgica et materialia*, 40(12):3443–3449, 1992.

[104] Sofiane Terzi, Luc Salvo, Michel Suéry, Nathalie Limodin, Jérôme Adrien, E Maire, Y Pannier, Michel Bornert, Dominique Bernard, M Felberbaum, et al. In situ x-ray tomography observation of inhomogeneous deformation in semi-solid aluminium alloys. *Scripta Materialia*, 61(5):449–452, 2009.

[105] Brian G Thomas. Modeling of hot tearing and other defects in casting processes. *ASM Handbook*, 22:362–374, 2009.

[106] TW Clyne and CLYNE TW. The influence of composition on solidification cracking susceptibility in binary alloy systems. 1981.

[107] L Katgerman. A mathematical model for hot cracking of aluminum alloys during dc casting. *JOM*, 34(2):46–49, 1982.

[108] U Feurer. Quality control of engineering alloys and the role of metals science. *Delft University of Technology, Delft, The Netherlands*, pages 131–45, 1977.

[109] John Campbell. *Castings*. Elsevier, 2003.

[110] WS Pellini. Strain theory of hot tearing. *Foundry*, 80(11):125–133, 1952.

[111] NN Prokhorov. Resistance to hot tearing of cast metals during solidification. *Russian castings production*, 2(2):172–175, 1962.

[112] Ilya I Novikov. Hot-shortness of nonferrous metals and alloys. Technical report, FOREIGN TECHNOLOGY DIV WRIGHT-PATTERSON AFB OHIO, 1968.

[113] B Magnin, L Katgerman, and B Hannart. Modeling of casting, welding and solidification process, 1995.

[114] A Yamanaka, K Nakajima, K Yasumoto, H Kawashima, and K Nakai. Measurement of critical strain for solidification cracking. *Modelling of Casting, Welding and Advanced Solidification Processes V*, pages 279–284, 1991.

[115] Mohammed M'Hamdi, Asbjørn Mo, and Hallvard G Fjær. Tearsim: A two-phase model addressing hot tearing formation during aluminum direct chill casting. *Metallurgical and Materials Transactions A*, 37(10):3069–3083, 2006.

[116] V Mathier, A Jacot, and M Rappaz. Coalescence of equiaxed grains during solidification. *Modelling and simulation in materials science and engineering*, 12(3):479, 2004.

[117] Stéphane Vernède and Michel Rappaz. A simple and efficient model for mesoscale solidification simulation of globular grain structures. *Acta materialia*, 55(5):1703–1710, 2007.

[118] Stéphane Vernède, Jonathan A Dantzig, and Michel Rappaz. A mesoscale granular model for the mechanical behavior of alloys during solidification. *Acta Materialia*, 57(5):1554–1569, 2009.

[119] AB Phillion, J-L Desbiolles, and M Rappaz. A 3d granular model of equiaxed-granular solidification. Technical report, Minerals, Metals & Materials Soc, 184 Thorn Hill Rd, Warrendale, Pa 15086 . . . , 2009.

[120] Meisam Sistaninia, AB Phillion, J-M Drezet, and Michel Rappaz. Simulation of semi-solid material mechanical behavior using a combined discrete/finite element method. *Metallurgical and Materials Transactions A*, 42(1):239–248, 2011.

[121] M Sistaninia, AB Phillion, J-M Drezet, and M Rappaz. Three-dimensional granular model of semi-solid metallic alloys undergoing solidification: Fluid flow and localization of feeding. *Acta Materialia*, 60(9):3902–3911, 2012.

[122] HR Zareie Rajani and AB Phillion. A multi-scale thermomechanical-solidification model to simulate the transient force field deforming an

aluminum 6061 semisolid weld. *Metallurgical and Materials Transactions B*, 46(4):1942–1950, 2015.

[123] HR Zareie Rajani and AB Phillion. 3-d multi-scale modeling of deformation within the weld mushy zone. *Materials & Design*, 94:536–545, 2016.

[124] AB Phillion, JL Desbiolles, and M Rappaz. A 3d granular model of equiaxed-granular solidification. *Modeling of Casting, Welding and Advanced Solidification Processes, TMS Publ., Warrendale, USA*, 2006.

[125] Yi Feng and Andre Phillion. A 3d meso-scale solidification model for steels, 2018.

[126] Damien Tourret and Ch-A Gandin. A generalized segregation model for concurrent dendritic, peritectic and eutectic solidification. *Acta Materialia*, 57(7):2066–2079, 2009.

[127] Damien Tourret, Guillaume Reinhart, Ch-A Gandin, GN Iles, Ulf Dahlborg, Monique Calvo-Dahlborg, and CM Bao. Gas atomization of al–ni powders: Solidification modeling and neutron diffraction analysis. *Acta Materialia*, 59(17):6658–6669, 2011.

[128] Damien Tourret, Ch-A Gandin, Thomas Volkmann, and Dieter M Herlach. Multiple non-equilibrium phase transformations: Modeling versus electro-magnetic levitation experiment. *Acta Materialia*, 59(11):4665–4677, 2011.

[129] Hongwei Zhang, Charles-André Gandin, Keiji Nakajima, and Jicheng He. A multiphase segregation model for multicomponent alloys with a peritectic transformation. In *IOP Conference Series: Materials Science and Engineering*, volume 33, page 012063. IOP Publishing, 2012.

[130] W Kurz, B Giovanola, and R Trivedi. Theory of microstructural development during rapid solidification. *Acta Metallurgica*, 34(5):823–830, 1986.

[131] V Mathier, Alain Jacot, and Michel Rappaz. Coalescence of equiaxed grains during solidification. *Modelling and Simulation in Materials Science and Engineering*, 12(3):479–490, may 2004.

[132] Hossein Beladi, Noel T Nuhfer, and Gregory S Rohrer. The five-parameter grain boundary character and energy distributions of a fully austenitic high-manganese steel using three dimensional data. *Acta materialia*, 70:281–289, 2014.

[133] S Terzi, L Salvo, M Suery, A Dahle, and E Boller. In situ microtomography investigation of microstructural evolution in al-cu alloys during holding in semi-solid state. *Transactions of Nonferrous Metals Society of China*, 20:s734–s738, 2010.

[134] M Sistaninia, AB Phillion, J-M Drezet, and M Rappaz. A 3-d coupled hydromechanical granular model for simulating the constitutive behavior of metallic alloys during solidification. *Acta Materialia*, 60(19):6793–6803, 2012.

[135] Ehsan Khajeh and Daan M Maijer. Physical and numerical characterization of the near-eutectic permeability of aluminum–copper alloys. *Acta Materialia*, 58(19):6334–6344, 2010.

[136] Dominique Bernard, Øyvind Nielsen, Luc Salvo, and Peter Cloetens. Permeability assessment by 3d interdendritic flow simulations on microtomography mappings of al–cu alloys. *Materials Science and Engineering: A*, 392(1-2):112–120, 2005.

[137] Ehsan Khajeh and Daan M Maijer. Permeability of dual structured hypoeutectic aluminum alloys. *Acta Materialia*, 59(11):4511–4524, 2011.

[138] Michael Le Bars and M Grae Worster. Interfacial conditions between a pure fluid and a porous medium: implications for binary alloy solidification. *Journal of Fluid Mechanics*, 550:149–173, 2006.

[139] Hideo Mizukami and Akihiro Yamanaka. Generation mechanism of unevenness of ultra low carbon steel at initial stage of solidification. *ISIJ international*, 50(3):435–444, 2010.

[140] Jack Dongarraxz, Andrew Lumsdaine, Xinhiu Niu, Roldan Pozoz, and Karin Remingtonx. A sparse matrix library in c++ for high performance architectures. In *Second object oriented numerics conference*, pages 214–218. Citeseer, 1994.

[141] Heung Nam Han, Yong-gi Lee, Kyu Hwan Oh, and Dong Nyung Lee. Analysis of hot forging of porous metals. *Materials Science and Engineering: A*, 206(1):81–89, 1996.

[142] Abaqus Users Manual. Version 6.10. *Abaqus Inc*, 2010.

[143] Abaqus/CAE simulia. `https://www.3ds.com/products-services/simulia/products/abaqus/`. Accessed: 2020-08-12.

[144] Kunihiko Nakashima and Katsumi Mori. Interfacial properties of liquid iron alloys and liquid slags relating to iron-and steel-making processes. *ISIJ international*, 32(1):11–18, 1992.

[145] Benoît Commet, Pascal Delaire, Jan Rabenberg, and Joost Storm. Measurement of the onset of hot cracking in dc cast billets. In *LIGHT METALS-WARRENDALE-PROCEEDINGS-*, pages 711–718. TMS, 2003.

[146] AB Phillion, S Thompson, SL Cockcroft, and MA Wells. Tensile properties of as-cast aluminum alloys aa3104, aa6111 and ca31218 at above solidus temperatures. *Materials Science and Engineering: A*, 497(1-2):388–394, 2008.

[147] Y Feng, M Založnik, BG Thomas, and AB Phillion. Meso-scale simulation of liquid feeding in an equiaxed dendritic mushy zone. *Materialia*, 9:100612, 2020.

[148] Yoshiyuki Ueshima, Shozo Mizoguchi, Tooru Matsumiya, and Hiroyuki Kajioka. Analysis of solute distribution in dendrites of carbon steel with δ/γ transformation during solidification. *Metallurgical Transactions B*, 17(4):845–859, 1986.

[149] Bernadette Weisgerber, Klaus Harste, and Wolfgang Bleck. Phenomenological description of the surface morphology and crack formation of continuously cast peritectic steel slabs. *steel research international*, 75(10):686–692, 2004.

[150] Christian Bernhard, Jürgen Reiter, and Hubert Presslinger. A model for predicting the austenite grain size at the surface of continuously-cast slabs. *Metallurgical and Materials Transactions B*, 39(6):885–895, 2008.

[151] Rian Dippenaar, Christian Bernhard, Siegfried Schider, and Gerhard Wieser. Austenite grain growth and the surface quality of continuously cast steel. *Metallurgical and Materials Transactions B*, 45(2):409–418, 2014.

[152] ES Szekeres. A review of strand casting factors affecting transverse cracking. In *Proceedings of 6th International Conference on Clean Steel*, pages 324–338, 2002.

[153] AB Phillion, S Vernede, M Rappaz, SL Cockcroft, and PD Lee. Prediction of solidification behaviour via microstructure models based on granular structures. *International Journal of Cast Metals Research*, 22(1-4):240–243, 2009.

[154] Lifeng Zhang, Shoji Taniguchi, and Kaike Cai. Fluid flow and inclusion removal in continuous casting tundish. *Metallurgical and Materials Transactions B*, 31(2):253–266, 2000.

[155] Jacob Bear. *Dynamics of fluids in porous media*. Courier Corporation, 2013.

[156] Y Feng and AB Phillion. A 3d meso-scale solidification model for metallic alloy using a volume average approach. *Materialia*, 6:100329, 2019.

[157] Yuta Shimoyama, Hidenori Terasaki, Eiji Ohtani, Satoru Urakawa, Yusaku Takubo, Keisuke Nishida, Akio Suzuki, and Yoshinori Katayama. Density of fe-3.5 wt% c liquid at high pressure and temperature and the effect of carbon on the density of the molten iron. *Physics of the Earth and Planetary Interiors*, 224:77–82, 2013.

[158] Seid Koric and Brian G Thomas. Thermo-mechanical models of steel solidification based on two elastic visco-plastic constitutive laws. *journal of materials processing technology*, 197(1-3):408–418, 2008.

[159] YA Meng and Brian G Thomas. Heat-transfer and solidification model of continuous slab casting: Con1d. *Metallurgical and materials transactions B*, 34(5):685–705, 2003.

[160] Hervé Combeau, Miha Založnik, and Marie Bedel. Predictive capabilities of multiphysics and multiscale models in modeling solidification of steel ingots and dc casting of aluminum. *Jom*, 68(8):2198–2206, 2016.

[161] Jürgen Fuhrmann and Hartmut Langmach. Stability and existence of solutions of time-implicit finite volume schemes for viscous nonlinear conservation laws. *Applied Numerical Mathematics*, 37(1-2):201–230, 2001.

[162] Munekazu Ohno and Hayato Sato. Macrosegregation simulation model based on lattice-boltzmann method with high computational efficiency. *International Journal of Heat and Mass Transfer*, 127:561–570, 2018.